Electronic Thesis and Dissertation Repository

12-14-2018 2:00 PM

Validating and Highlighting the Advantages of the Optimal Estimation Method For Rayleigh Lidar Middle Atmospheric Temperature Retrievals

Ali Jalali
The University of Western Ontario

Supervisor
Sica, Robert J.
The University of Western Ontario

Follow this and additional works at: https://ir.lib.uwo.ca/etd

Part of the Atmospheric Sciences Commons, Climate Commons, and the Numerical Analysis and Computation Commons

Abstract

An improved understanding of temperature variations in Earth's middle atmosphere is important for the improvement of our understanding of climate and weather on the surface. The optimal estimation method (OEM) is an inversion modeling approach, which uses regularized nonlinear regression to retrieve, in this case, the temperature of Earth's middle atmosphere using Rayleigh-scatter lidar measurements. The OEM regularization term is the *a priori* knowledge of the atmospheric temperature profile. In this thesis I use lidar temperatures in the altitude range 30–110 km to construct a temperature climatology using over 500 nights of measurements obtained by the Purple Crow Lidar in London, Ontario. The OEM produces several diagnostic tools, such as averaging kernels and an uncertainty budget which includes both systematic and statistical uncertainties important for atmospheric applications. Using OEM allows for the quantitative calculation of the maximum valid altitude of the retrieval by determining at which altitude the *a priori* temperature profile influences the retrieval by more than 10%. This new knowledge extends the temperature retrievals 5 to 10 km higher in altitude than traditional methods. The OEM retrievals are validated by comparison of the PCL temperature climatology with other measurements. Excellent agreement is found between the PCL and sodium lidar climatologies in the upper mesosphere and lower thermosphere, where the temperature variability is highest. Thus validated, the OEM can now be applied to other similar lidar systems. Lidar retrievals of atmospheric temperature profiles using the OEM typically use a retrieval grid whose number of points is larger than the number of pieces of independent information obtainable from the measurements. Consequently, retrieved geophysical quantities contain some information from the *a priori* values, which can affect the temperatures at higher altitudes. I present a method for removing the *a priori* information from the retrieved profiles. The OEM provides averaging kernels, or weighting functions, at each level. I applied the OEM to measurements obtained from two lidars during a coincident measurement campaign between the Deutscher Wetterdienst and

National Aeronautics and Space Administration. The OEM averaging kernels are then used to improve lidar and satellite intercomparison.

Co-Authorship

This thesis is comprised of three papers among which one is already accepted for publication in the Atmospheric Measurement Technique (AMT) journal, and one is submitted to AMT and still undergoing the review process. The third paper will be submitted in the near future.

The work described in Chapter 2 is based on using 16 years of lidar measurements of the middle atmosphere to form a climatology for use in studying atmospheric temperature change, using an optimal estimation method (OEM). Using OEM allows us to calculate a complete systematic and random uncertainty budget, and allows an additional 10 km in altitude of the measurement to be used, improving our ability to detect atmospheric temperature change up to 100 km altitude. Ali Jalali was responsible for applying the OEM data analysis technique, developing the code to form the climatologies, and paper preparation. He also was involved in operating the lidar after July 2012. R. J. Sica was responsible for the supervision of the doctoral thesis, contributions to manuscript preparation, obtaining the measurements in collaboration with Dr. P. Argall (Fanshawe College), coding the OEM temperature retrieval and, in collaboration with A. Haefele, first applying the OEM to Rayleigh-lidar temperature retrievals. Alexander Haefele helped in manuscript preparation and many OEM and scientific discussions relevant to this work. The results of Chapter 2 are published in the Atmospheric measurement Techniques journal (Jalali et al., 2018b).

In Chapter 3, we built upon the work in Von Clarmann and Grabowski (2007) concerning the *a priori* profile influence in the optimal estimation method applied to active remote sensing measurements, with examples given for lidar retrievals of temperature and water vapour mixing ratio. The optimal estimation method is a new technique for many active remote sensing researchers. This study gives insight into understanding the affect on retrievals of the *a priori* information. In this paper, Ali Jalali was responsible for developing the *a priori* removal method and code, as well as manuscript preparation. Ali Jalali also applied the method to the Rayleigh temperature analysis. This work is the second component of his doctoral thesis. Shannon Hicks-Jalali applied my removal method to the water

vapour daytime and nighttime measurements, as well as helped with manuscript preparation. Robert J. Sica was responsible for supervising the doctoral theses and contributed to manuscript preparation. Alexander Haefele contributed to manuscript preparation and scientific discussions. Thomas Von Clarmann also contributed to the scientific discussions which resulted in this paper, helped develop the method based on his original work, and contributed to manuscript preparation. The results of this chapter are submitted to the Atmospheric Measurement techniques journal (Jalali et al., 2018a).

In Chapter 4, I applied the OEM to the DWD (German weather service) and NASA lidar measurements were taken during a campaign in 2005 to improve the intercomparison. Ali Jalali was responsible for all data analyses and paper preparation. R. J. Sica suggested and supervised the project and Alexander Haefele helped with OEM theory and averaging kernel comparisons. Wolfgang Steinbrecht (DWD) and Thomas McGee (NASA) provided the measurements for this project. Wolfgang also hosted me at DWD and provided useful conversion regarding analysis of the DWD measurements. John Sullivan (NASA) participated in the NASA lidar data discussions and helped provide insight into the NASA lidar operating procedures.

Bibliography

Jalali, A., S. Hicks-Jalali, R. J. Sica, A. Haefele, and T. Clarmannvon . A practical method to remove a priori information from lidar optimal estimation method retrievals. *Atmospheric Measurement Techniques Discussions*, 2018:1–23, 2018a. doi: 10.5194/amt-2018-347.

Jalali, A., R. J. Sica, and A. Haefele. A middle latitude rayleigh-scatter lidar temperature climatology determined using an optimal estimation method. *Atmospheric Measurement Techniques Discussions*, 2018:6043–6058, 2018b. doi: 10.5194/amt-11-6043-2018.

Von Clarmann, T. and U. Grabowski. Elimination of hidden a priori information from remotely sensed profile data. *Atmos. Chem. Phys.*, 7:397–408, 2007.

Acknowledgements

First, I would like to thank my supervisor Prof. R. J. Sica for his support and guidance throughout my PhD. Being a part of his research group has provided me with many unique opportunities.

I would also like to thank Prof. Wayne Hocking and and Prof. Margaret Campbell-Brown for serving on my Advisory Committee during these years and sharing their experiences with me. I would also like to thank Prof. Wayne Hocking for many offline useful discussions about research and life.

I would also thank Dr. Alexander Haefele and MeteoSwiss group, for providing me with the opportunity to travel to Switzerland and other conferences. Also, I learned a lot about the OEM from Alexander.

I would also like to thank Patricia Sica for spending large amounts of time reading this thesis and for her attention to detail.

I am definitely grateful to my family, my Mom, Mahin Pourani, and my Dad, Mostafa Jalali, and my sisters Fatemeh and Fereshte, and my brother Hossein. They provided me with the chance to gain a lot of experience far from home. They have always supported my education and considered it a priority. Without their emotional support these last few years would have been much more difficult.

Finally, I owe more than a thank you to my best friend and wife, Shannon. This job could not have been accomplished without her help, scientifically and emotionally. I appreciate all the precious time she has spent for me as an editor and helping me through all the scientific problems patiently. Thanks for her true love and friendship.

Dedication

To my parents and my wife for their endless support and love

Contents

List of Figures

xvii

List of Symbols

c_{sound} The speed of sound

γ' The ratio of specific heat of air

R The ideal gas constant

k Boltzmann's constant

M The mean molecular mass of air

T Temperature

N_o Lidar observed photocounts

N_t Lidar true photocount rate

N Number of returned photons

γ Dead time

z Altitude

ξ_{sys} Receiver efficiency

$\Gamma_{emitted}$ Transmittance of the photons from the ground

Γ_{return} Transmittance of the photons returning to the telescope

τ Optical depth

O Overlap function

λ Wavelength

σ Scattering cross section

σ_{ext} Extinction cross section

n	Number density
A	Area
Δt	Time
Δz	Altitude Bin Size
B	Background photon counts
h	Planck constant
C	Lidar normalization constant
P	Pressure
ρ	Density
g	Acceleration due to the gravity
ν	Frequency
$\Delta \nu$	Frequency shift
β	Molecular rotational constant
J	Rotational quantum number
$\mathbf{y}$	Measurement vector
$\mathbf{F}$	Forward model
$\mathbf{b}$	Forward model parameters
ϵ	Measurement noise
$\mathbf{S}_{\epsilon}$	Measurement covariance matrix
$\mathbf{S_a}$	Measurement covariance matrix
$\hat{\mathbf{x}}$	Retrieved parameter

$\mathbf{x_a}$ *a priori* profile

$\mathbf{G}$ Gain matrix

$\mathbf{K}$ Jacobian matrix

$\mathbf{A}$ Averaging kernel matrix

$\mathbf{Tr}$ Trace of a matrix

$\mathbf{dgf}$ Degree of freedom

N_A Avogadro's number

Chapter 1

Introduction

1.1 Overview of the Atmosphere

Earth's atmosphere is comprised of several different molecules with varying concentrations depending on the altitude or season. On average below $48\,\mathrm{km}$ ($1\,\mathrm{mb}$), the major atmospheric constituents are as follows: nitrogen (N_2) at 78%, oxygen (O_2) with 21%, and argon (Ar) with 0.93% concentration. There are a variety of trace gases including: carbon dioxide (CO_2) with 0.04%, methane (CH_4), ozone (O_3), and many other trace gases with less than 0.01% like N_2O, water vapour, chlorofluorocarbons and CO. Despite their small concentrations, these trace gases have important physical and chemical properties such that when they interact with solar radiation they can affect the energy balance and consequently the temperature of Earth's atmosphere. The distribution of these gases in the atmosphere depends on the dynamics of each atmospheric region. The lower atmosphere, which starts from the ground up to the tropopause, is mostly heated through energy transfer from Earth's surface and convective activities, which together cause rapid vertical exchange of energy and mass. The distribution of the gases in the middle atmosphere (25-$110\,\mathrm{km}$) is highly dependent on dynamical and chemical processes as well as the energy and momentum budget. The gravitational force causes atmospheric gases to separate by their weight, and thus stratifies density in the atmosphere, which ultimately constrains the air's vertical displacements. The air's motion, and consequently the transport of chemical species in the atmosphere, depends on density stratification.

The atmosphere has been classified into four layers based on their thermal characteristics such that the change of temperature as a function of altitude has a constant sign in each layer (Brasseur and Solomon, 2005). From the ground up, the layers are: the troposphere, stratosphere, mesosphere and thermosphere. These layers are separated by isothermal regions at the edge of each "sphere" called the tropopause, stratopause, and mesopause. The altitudes of these regions vary based on latitude and season. Each region of Earth's atmosphere is characterized by its change in temperature with altitude. Typical summer and winter atmospheric temperature profiles are shown in Fig. 1.1. The COSPAR International Reference Atmosphere (CIRA) is an empirical model based on data taken from various instruments at different altitudes and latitudes. The CIRA-86 provides the monthly temperature from the surface up to 120 km. The CIRA-86 is an empirical models of atmospheric temperature and densities from surface to 2000 km. Before the CIRA-86 sixties different editions of the CIRA have been published. In altitudes above 100 km the CIRA-86 is identical with the MSIS-86 (Hedin, 1991) model. The temperature measurements used to make the CIRA-86 model were taken from several global data compilations including ground-based and satellite (Nimbus 5, 6, 7) measurements. Then at 120 km the CIRA-86 is merged with MSIS-86. The temperature profiles in Fig. 1.1 are from the CIRA-86 model (Fleming et al., 1988). The troposphere contains 85% of the mass of the atmosphere (Marshall and Plumb, 2007) and the temperature decreases significantly (10 K per kilometer) from the surface up to the tropopause at 8 to 16 km altitude - depending on the season and latitude. In the stratosphere, solar UV radiation is absorbed by ozone, causing the temperature to increase with altitude. The maximum temperature in the stratosphere occurs around 45 to 50 km at the stratopause. Then, the temperature decreases through the mesosphere to reach a minimum at roughly 85 km in the summer or at 100 km in the winter. This variation in the mesopause height is due to seasonal temperature differentials with altitude in the upper mesosphere (Gerding et al., 2008). Pressure decreases through the atmosphere exponentially (barometric law) such that 99.9% of the total mass of the atmosphere is below 1 mb (48 km). The barometeric formula (Eq. 1.1) shows that for an isothermal atmosphere the pressure of the air decreases with altitude in a way that the pressure drops by factor of e at each scale height

(H).

$$P(z) = P_0 e^{\left(-\frac{z-z_0}{H}\right)},\tag{1.1}$$

which

$$H = \frac{kT}{mg}.\tag{1.2}$$

In Eq. 1.1, $P(z)$ is the pressure of an isothermal, m is the molecular mass, z and z_0 are height and surface height respectively and P_0 is pressure at the surface. Above $100\,\text{km}$ is a warm layer, called the thermosphere, where the Sun's short wavelength UV radiation is absorbed by mainly O and then N_2 and O_2.

Atmospheric physicists often label the regions of the atmosphere as the lower, middle, and upper atmosphere. The lower atmosphere (surface–$25\,\text{km}$) refers to the troposphere and the lower stratosphere. Collecting data in the troposphere is more frequent and easier relative to other layers due to accessibility, specifically near the surface where most of the measurements from different instruments are collected to measure temperature, pressure, humidity, wind speed, and wind direction. The middle atmosphere includes the stratosphere and mesosphere and lower thermosphere from $25\,\text{km}$ – $110\,\text{km}$. The upper atmosphere typically refers to the thermosphere layer which extends from about $100\,\text{km}$ to $400\,\text{km}$. This thesis will mainly focus on the middle atmosphere.

1.2   The Middle Atmosphere

The middle atmosphere is the region extending from the tropopause to the turbopause (around $110\,\text{km}$). The turbopause is a layer which transition from turbulence-dominated mixing to molecular diffusion occurs. The middle atmosphere is comprised of several unique regions which play a key role in middle atmospheric dynamics and chemistry. Below the turbopause, turbulence is the key process of mixing. Above the turbopause, atmospheric gases separate according to their molecular mass. Heavier molecules like N_2, O_2, and Ar stay in the lower thermosphere and lighter atoms (H, O, N and He) are concentrated at higher altitudes (above $500\,\text{km}$; Quiroz (1968); Plane et al. (2015)). Above the turbopause, turbulent motion decreases and molecular diffusion becomes the main motion.
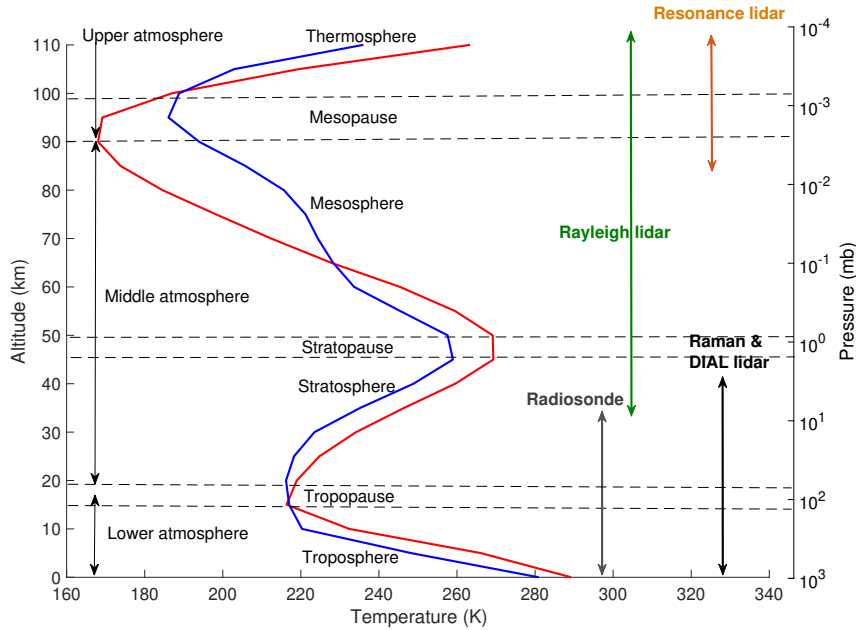
Figure 1.1: Typical summer and winter atmospheric temperature profiles at the middle latitudes ($\approx$ 45°N). Temperature profiles are taken from the CIRA-86 model. The layers of the atmosphere: the troposphere, mesosphere, and thermosphere are also shown. The operational range of some atmospheric lidars is shown by arrows, as well as radiosondes (weather balloons).

1.2.1 Chemistry and Physics of the Middle Atmosphere

The sources of energy in the Mesosphere and Lower Thermosphere (MLT) region include: high-energy downward solar electromagnetic radiation, upward propagating gravity waves, and chemical radiative processes in the upper mesosphere. The long-wave heating radiation from below is not important because the density is very low in the MLT and their energies do not transfer to the molecules.

The main source of energy in the MLT is solar energy. The solar energy is absorbed by the ozone in the stratosphere and mesosphere, and by oxygen molecules in the MLT region. Atomic oxygen plays the main role of all the chemistry in the MLT via recombination with other atoms and molecules through exothermic chemical reactions. Photolysis of O_2 by solar radiation produces large amount of atomic oxygen and chemical potential energy in the MLT. Atomic oxygen releases heat through the exothermic chemical reactions and through these

processes solar and chemical energy release heat.

The main energy sinks are thermal infrared cooling by CO_2, ozone and water vapour. The cooling by CO_2 emission is larger than all the heating processes in the MLT. The emission of CO_2 in the MLT is much larger than its absorption and therefore, the net effect of CO_2 is cooling. In the MLT, the molecular kinetic energy excites the vibrational states of a molecule's energy level and then energy is emitted by infrared emission. Through this thermal infrared emission, the atmosphere cools.

Considering only the local radiative equilibrium between the mentioned source and sinks of energy results in very large and unrealistic vertical temperature gradients in temperature models (Manabe and Moller, 1961). Therefore, it is important to consider vertical transport as a source of non-radiative energy. Gravity waves are the primary transporters of non-radiative energy into the MLT. Planetary waves and atmospheric tides are most important in the stratosphere however, atmospheric tides have a large impact up to the lower thermosphere (Kopp et al., 2015). The source of planetary waves are large-scale variations in pressure, temperature, and wind in the troposphere, which propagate vertically upward.

Consider an air parcel in a stable atmospheric layer. If the air parcel is forced to displace to higher altitudes like uplifting over a mountain, Earth's gravity acts as a restoring force that pushes the air parcel back to its initial level. The lifting force is buoyancy. The oscillation caused by the displacement generates what is called a gravity wave. Gravity waves are generated in the troposphere between stable layers of the atmosphere with different densities. Gravity waves cannot be generated if the atmosphere is unstable. Because in an unstable condition, a parcel of air which is displaced vertically will not oscillate and will continue to rise. Gravity waves are produced by different processes in the troposphere, such as convection, cyclonic fronts, topography, cumulonimbus cloud formation, and wind shearing. Gravity waves then transport the momentum and energy gained in the troposphere to the middle atmosphere and they are the main source of dynamical variability in the mesosphere. The propagation of gravity waves depends on the temperature and wind in the atmosphere. As gravity waves propagate upward, their amplitude grows exponentially as the atmospheric density decreases. At a critical level, where the gravity phase speed is equal to the background speed, the gravity waves become unstable and break and release

their energy into the atmosphere (Brasseur and Solomon, 2005). Planetary waves and solar tides (Chapman and Malin, 1970) are also two important waves that are components of the general atmospheric circulation. The source of atmospheric tides is from the daily absorption of solar energy in the atmosphere and the restoring force is gravity. Tides also grow in amplitude with altitude as they propagate vertically. The tidal amplitudes are small in the stratosphere, and their amplitude grow as they propagate into the mesosphere. Planetary waves are large-scale oscillations due to the conservation of absolute vorticity, which is an atmospheric parameter combined from Earth's rotation and temperature gradient between the poles and equator. Planetary wave amplitudes and frequencies are stronger during winter due to larger temperature gradients between the poles and the equator. Planetary waves and tides are important especially in the stratosphere and stratopause for transportation of species including trace gases produced in the lower atmosphere. Planetary waves can reach very large amplitudes and also interact with gravity waves and tides in the MLT region.

A middle atmosphere temperature climatology helps to determine future climate expectations and understanding of the energy budget of the middle atmosphere. A temperature climatology is a mean temperature over a period of time at different altitudes at the different times of the year. The mean temperature is taken from the measurements on the same day over the entire data set time period. Temperature climatologies may be made over varying time lengths; although, the results from a longer measurements record would present the average temperature more accurately.

1.2.2   Importance of the Middle Atmosphere

Improving middle atmosphere temperature climatologies is a priority focus of programs such as the Stratosphere Reference Climatology Group, part of the World Climate Research Programme (WCRP) Stratospheric Processes and their Role in Climate (SPARC) project (https://www.sparc-climate.org). Climatologies are important for trend analyses because they are the average temperatures which must be removed from the measurements in order to create accurate trends. Defining middle atmosphere temperature trends, including those in the stratosphere, mesosphere, and lower thermosphere, is important for understanding the connection between temperature variations in the middle atmosphere and corresponding

changes in the lower atmosphere. Ramaswamy et al. (2001a) and Randel et al. (2004, 2009, 2016) discussed the effects of the middle atmosphere temperature trends over time using different instruments. They found that cooling trends increase with height from the lower stratosphere with a cooling rate of 0.1–0.2 K/decade to the middle and upper stratosphere with) a 0.6 K/decade cooling rate over the period of 1979 to 2015. One of the important role of the middle atmosphere is detecting the global temperature change. During the last few decades atmospheric concentrations of greenhouse gases (especially CH_4 and CO_2) have increased dramatically and are affecting the global climate. Variations and trends in the middle atmosphere are representative of climate change and accurate upper atmosphere measurements are essential to detect changes. Among the different atmospheric parameters, temperature is the most affected by changing concentrations of greenhouse gases. The extent of climate change can be evaluated by considering the dramatic increase in the amount of trace gases over the last few decades. The increase in trace gases has disrupted the energy exchange balance between Earth and the atmosphere and magnified the greenhouse effect, a process that traps thermal radiation in the troposphere. In the troposphere, temperature decreases with altitude, therefore active atmospheric gases absorb more energy than they emit (Dickinson and Cicerone, 1986). The increase in trace gases has increased their energy absorption, resulting in a global rise in tropospheric temperatures. However, the greenhouse effect also causes cooling in the middle and the upper atmosphere. This cooling effect is detectable in the middle and upper atmosphere, specifically in the stratosphere (Lastovicka et al., 2006). The cooling is predominantly caused by CO_2 and its infrared emission. The CO_2 cooling effect has been modelled in global upper atmosphere models which show that by doubling CO_2 and halving CH_4 concentrations, the mesospheric and thermospheric temperatures cool by 10 K and 50 K respectively (Roble and Dickinson, 1989). Currently, researchers have focused on middle atmosphere temperature trends, especially the stratospheric temperature trends, because it is a key component in the detection of climate change.

Rayleigh lidars can be used to detect the cooling rate in the middle atmosphere. A cooling of 4 K/decade in the mesosphere was detected by Hauchecorne et al. (1991) using the Haute Provence Observatory (OHP) Rayleigh between 1978 and 1989 in southern France. Then this trend analyses was updated in 1995 by Keckhut et al. (1995) who showed the same 0.4 K/year

cooling in the mesosphere. Ramaswamy et al. (2001b) also conducted a comprehensive study using several instruments to investigate the cooling rate in the stratosphere. The study also included OHP lidar measurements from 1979 to 2001 and they found that there was a considerable cooling in the stratosphere during the mid 1960s to mid 1990s. All data sets agreed on the general cooling but at different rate. Studies like Dickinson and Cicerone (1986) and Roble and Dickinson (1989) have indicated that there is a coupling between the different layers of the atmosphere, including the lower and upper regions, and have shown that understanding the lower atmosphere and the global circulation of the atmosphere requires an understanding of the middle atmosphere. The atmospheric circulation above the tropopause includes two main regimes, pole to pole circulation above 45-50 km and equator to pole below 30 km (Dunkerton, 1978) (Brewer-Dobson circulation). Air rises in the summer polar mesosphere and adiabatic cooling processes cause the air to reach to a minimum temperature. The temperature at the summer polar mesosphere is the coldest temperature in Earth's atmosphere (see Figure 1.2). Figure. 1.2 shows the global average temperature calculated using the MSIS (Hedin, 1991) model. It can be seen that the temperature at the mesopause in the summer pole is $-150\,°C$ which is 100 degrees colder than the winter troposphere. Also, the summer mesopause in middle latitude ($\approx 45°N$) is around $-120\,°C$ and is above $-90\,°C$ during the winter (Fig. 1.1). The MLT is an active area. For example, gravity waves are produced in the lower atmosphere and then propagate toward the upper atmosphere where they start dissipating and breaking down (grey lines in Figure 1.2). Gravity waves cause short-term variations in temperature, density and wind in the upper mesosphere and lower thermosphere.

Another example of coupling between layers has been seen in global climate studies. Wave-driven general circulation in the middle atmosphere (specifically the stratosphere) can affect climate in the troposphere (Hartley et al., 1998; Perlwitz and Harnik, 2003; Colucci, 2010). Baldwin and Dunkerton (2001) showed that zonal wind anomalies in the upper stratosphere propagate downward to the surface. Polvani and Waugh (2004) presented the argument that the stratospheric circulation anomalies are because of an anomaly in the wave activity from the troposphere. Another way that the stratosphere can influence the tropospheric weather system is through a process called tropopause folding, where stratospheric
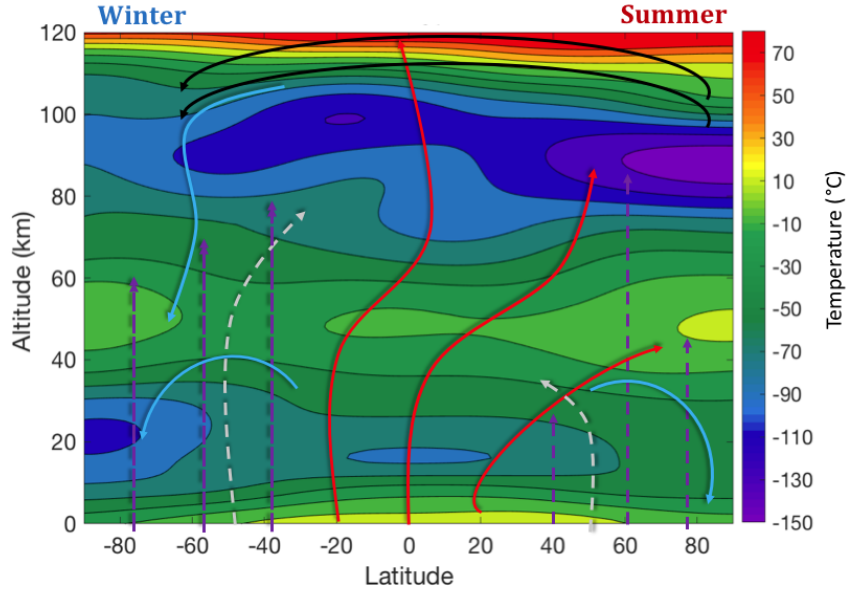
Figure 1.2: The temperature structure of Earth during Northern summer calculated from the MSIS model for 15 July 2012. The red, blue, and black arrows show the Brewer-Dobson circulation. The purple and white arrows represents the gravity waves and planetary waves, respectively in the middle atmosphere. The long wavelengths of gravity waves filter out by the lower atmosphere and shorter wavelengths reach to the MLT region. Due to the low pressure in the MLT, gravity waves break and release their energy and momentum in the MLT, resulting in meridional flow toward the winter pole. Adapted from Meriwether and Gerrard (2004).

pressure anomalies can grow through the troposphere and affect the cyclones and anticyclones (Holton, 2004). Because of this coupling, numerical weather prediction models try to increase their maximum altitudes in order to improve tropospheric forecasts over longer periods. For instance, Boville and Cheng (1988) used two versions of a general circulation model to investigate the effect of changing the upper boundary height. Each model had identical conditions, with the exception of the number of their vertical levels. The upper boundaries were set to the middle of the stratosphere and the middle of the mesosphere, respectively. The results showed that the model with the lower boundary height weakly predicted the troposphere parameters because of waves reflecting off the upper boundary model to the lower levels. However, the model with a higher upper boundary presented more accurate

forecasts. Therefore, it is necessary for models to consider the effect of gravity waves on the general circulation. However, not many high resolution observations which are continuous in time are available for this purpose to validate the representation of atmospheric waves in forecast models. Rayleigh lidars are excellent instruments to fill this measurement gap. For example, Sica and Russell (1999) used Rayleigh lidar measurements to find the number of waves in the gravity waves spectrum. They found that only two-three waves, with vertical wavelengths between 2 to 10 km and growth rates on the order of $1/(14\,\mathrm{km})$ or less carry most of the energy.

1.2.3   Measuring Temperature in the Middle Atmosphere

Many different instruments have been used to measure atmospheric properties in the middle atmosphere including satellite instruments, rocketsondes, lidars and radars. Rocketsondes were one of the first instruments used to study the middle atmosphere but their high cost and discontinuous measurements were problematic for continuous use. Radars have contributed to middle atmosphere measurements very effectively, specifically meteor radars (MR), Mesospheric-Stratospheric-Tropospheric (MST) radars (which cover from surface up to 100 km) and incoherent scatter radars (100 to 500 km). Meteor radars use meteor trail decay times to estimate the temperature in the MLT region. The decay rate of the meteor backscatter provides the ambipolar diffusion coefficient, which depends on the temperature of the atmosphere (Hocking, 1999). Various ground- and air-based remote sensing instruments like satellites and lidar were the solution to covering the entire MLT region with as high vertical resolution as possible. The advantage of lidars over the satellites are their high temporal and spatial resolution. However, satellite instruments provide better global coverage of measurements, which lidars are not capable of.

Satellites

Satellite temperature measurements are valuable data sets for obtaining a global view of atmospheric temperature, as their speed is high and they measure Earth's temperature at different latitude and longitude in relatively short periods of time. Nadir and limb are two

types of satellite viewing orientations. A nadir view is the direction pointing directly below the satellite. Satellites in limb view are tilted at an angle to look through the edge of the atmosphere. This view has a much longer path in the atmosphere and therefore a larger air mass. The long ray-path through the atmosphere provides higher signal-to-noise ratio and the observation angle variation provides vertical scanning of different layers of the atmosphere. Satellites usually use the limb view for studying the mesosphere and stratosphere. Usually, there are multiple instruments installed in each satellite to collect the data from Earth's atmosphere. These instruments use several techniques to collect measurements at specific wavelengths and altitude ranges, such as passive microwave limb emission and thermal infrared limb emission. Satellites instruments like infrared limb sounders are capable of measuring the spectrum of emitted radiation of various gaseous constituents in the atmosphere. Each molecule at a certain temperature and pressure has a specific spectrum, therefore, satellites use the atmosphere's spectrum to calculate the temperature and pressure as a function of altitude. In order to compare the retrieved temperature from lidar with another instrument, satellites are a good option because they cover the entire MLT region globally.

There are three types of satellite orbits: high Earth orbit (weather and some communications satellites around $35000\,\text{km}$), medium Earth orbit (navigation and specialty satellites focused on specific regions, between 2000 and $35000\,\text{km}$), and low Earth orbit (most of the scientific satellites, below $2000\,\text{km}$). The height of the orbit determines the speed of a satellite where the closer to Earth it is, the faster it must move to overcome Earth's gravity. A sun-synchronous orbit is a low Earth orbit that passes over each location at the same local time on each orbit. A satellite's orbit determines the frequency with which it can collect measurements and the size of its global measurement coverage.

In Chapter 4 of this thesis, the lidar measurements are compared to measurements from two satellites: Aura/MLS and TIMED/SABER. Aura and TIMED are the name of the satellites and MLS and SABER are the names of the instruments. The basic operation principles of these satellites are discussed below.

Aura/MLS

The Earth Observing System (EOS) Aura spacecraft was launched in 2004 in a sun-synchronous orbit at $705\,\mathrm{km}$ with a sixteen-day repeat cycle and 233 revolutions per cycle. The Microwave Limb Sounder (MLS) on the Aura satellite observes the thermal microwave limb emission of atmospheric molecules and scans Earth limb 240 times per orbit creating 3500 vertical profiles per day from the surface to $90\,\mathrm{km}$ every $24.7\,\mathrm{s}$, from 82°S to 82°N latitudes. The atmospheric temperature determined by the MLS is based on the measurement of thermal microwave emission lines of O_2 at $118\,\mathrm{GHz}$ (Schwartz et al., 2008).

TIMED SABER

The Thermosphere Ionosphere Mesosphere Energetics and Dynamics (TIMED) is a satellite that was launched in 2001 in a sun-synchronous orbit at $625\,\mathrm{km}$ with an orbital period of 97 minutes with one revolution per 60 days. The focus of TIMED is on the processes governing the chemistry and dynamics of the mesosphere and lower thermosphere. SABER (Sounding of the Atmosphere using Broadband Emission Radiometry) is a multi-channel infrared radiometer installed on TIMED. SABER measures atmospheric infrared radiances in 10 broadband channels by scanning the limb of Earth's atmosphere. Each scan takes about $110\,\mathrm{s}$ with a vertical sampling of $0.37\,\mathrm{km}$ and a $2\,\mathrm{km}$ field of view (Russell et al., 1999). SABER calculates the kinetic atmospheric temperature and CO_2 volume mixing ratio by measuring the emission of CO_2 at 15 and 4.3 μm.

Rocketsondes

The temperature and wind in the middle atmosphere have been studied since late 1950s by using rocketsondes. There are several techniques that are used by rocketsondes to measure the temperature, but we will only discuss two of them here: the grenade and the falling sphere. In the grenade technique, a rocket is launched up to $100\,\mathrm{km}$ altitude and several grenades ejected from the rocket as it ascends and explode every few kilometers. One can then measure the position in space, sound travel times to the ground and the angle of the arriving sound waves. The measurements of sound delay times from exploded grenades are

recorded by a network of ground stations, and temperature profiles can be derived by these times in the mesosphere (Stroud et al., 1960). The temperature is derived from

$$c_{sound} = \sqrt{\frac{\gamma' RT}{M}}, \tag{1.3}$$

where c_{sound} is the velocity of sound in each layer, γ is the ratio of specific heat of air, R is the ideal gas constant, M is the mean molecular mass of air and T is temperature. The temperature error in the grenade technique increases from $0.5\,\mathrm{K}$ at $30\,\mathrm{km}$ to $10\,\mathrm{K}$ at $90\,\mathrm{km}$. However, the main source of error is the time of arrival measurement of the sound waves and is less than $\pm 3\,\mathrm{K}$ at altitudes below $75\,\mathrm{km}$ (Stroud et al., 1960).

The second technique is the falling sphere method. This method was developed by the Department of Aeronautical Engineering of the University of Michigan and is based on measurements of atmospheric drag acceleration on falling spheres ejected from the rockets. This method can measure the atmospheric pressure, density and temperature up to $100\,\mathrm{km}$ (Bartman et al., 1956). A metalized mylar sphere ($1\,\mathrm{m}$ diameter) is ejected from a rocket at the peak of its trajectory and it floats in the atmosphere. Then, the trajectory of the sphere is tracked by a high precision radar. The air density can be determined using the sphere's trajectory and the atmospheric drag acceleration of the falling sphere. Then, the temperature can be calculated from density. The main source of error in this technique is due to the uncertainty of the drag coefficient which is considered 2% up to $75\,\mathrm{km}$ and increases to 5% above $75\,\mathrm{km}$. Lübken et al. (1994) made an intercomparison using the Rayleigh lidar and falling sphere with maximum time difference of 1 hour, from the ground to the lower thermosphere. They found good agreement between the two techniques. The mean of the deviations was less than $3\,\mathrm{K}$ between 35 and $65\,\mathrm{km}$, and between 65 and $80\,\mathrm{km}$ the Rayleigh lidar temperatures were around $5\,\mathrm{K}$ colder than the measurements using falling spheres.

LIDARs

Lidars (originally from "light" and "radar", later from LIght Detection and Ranging) are one of the few instruments that can measure atmospheric properties from the surface up to the lower thermosphere. A lidar is an active remote sensing system which uses the same principles as radar, but with a laser as the emission source. One of the advantages of lidar

is its well-collimated short laser pulses provide higher spatial and temporal resolution when compared to other remote sensing instruments. Unlike satellite instruments, lidars are stable and can operate for long periods of time. These characteristics make lidars useful for studying atmospheric properties and their variability. In the next section (Section 1.3), different kinds of lidars and their techniques to measure temperature will be discussed.

1.3   Lidar

An atmospheric lidar emits laser pulses toward the sky and then measures the backscattered photons from molecules and aerosols in the atmosphere. The wavelength of the backscattered photons and the number of backscattered photons received by the lidar are used to determine atmospheric properties like atmospheric density and temperature, molecular concentration, as well as wind speed and direction (Leblanc et al., 2013). There are different kinds of atmospheric lidars, and each use different kinds of scattering mechanisms to measure different characteristics of the atmosphere. The scattering processes in the atmosphere are divided into three categories: Raman, Rayleigh, and Mie scattering. Raman lidars measure temperatures below 30 km and molecular concentrations of water vapour, ozone, and nitrogen. Temperature and molecular density above 25 km is usually measured by Rayleigh lidars. DIfferential Absorption Lidar (DIAL) can also measure temperature by using temperature-dependent absorption of O_2 lines in the near infrared. Resonance lidars measure temperature, density, and wind velocity between 80 and 105 km by using scattering off of various metal layers made of sodium, potassium, iron, lithium, and calcium located at those altitudes (Measures, 1992). Figure. 1.1 shows the ranges of operation for the lidars mentioned above.

1.3.1   Lidar Basics

An atmospheric lidar is comprised of three main parts: the transmitter, receiver, and detection system. The transmitter is a laser that acts as a source of energy, the receiver is a telescope that collects the backscattered photons, and the detection system is a transient recorder system which converts the collected photons into a digital or analog signal (Kovalev and Eichinger, 2004).

Transmitter

Most of the modern Rayleigh and Raman lidars use Yttrium-Aluminium-Garnet (YAG) solid state crystals with another element to produce a stable beam. Rayleigh lidars typically use Neodymium to make Nd:YAG lasers. These Nd:YAG lasers produce a beam wavelength of $1064\,nm$ and the frequency of the beam is then doubled, tripled or quadrupled by another crystal to generate the desired wavelength. The Rayleigh scattering coefficient increases with decreasing wavelength as is proportional to λ^{-4} (Kovalev and Eichinger, 2004). Hence, going to shorter wavelength increases the signal for a given laser power. The choice of laser depends on the ease of use and power provided by the laser. Using a doubled Nd:YAG crystal at $532\,nm$ or, for DIAL ozone-Rayleigh lidars using XeCl excimer lasers, $353\,nm$, are common choices.

Receiver

Two parameters determine the design of a telescope as a receiver: the field-of-view of the telescope should be larger than the divergence of the laser beam, and the diameter of the telescope limits the amount of signal detected. Either a lens or a mirror can be used as a receiver but most lidars use mirrors as they can have larger areas and are more cost-efficient. The backscattered photons are collected and focused onto a photo multiplier tube (PMT) at the mirror focal point. Then the electric signal produced by the PMT is recorded by the transient recorder system.

Detection System and Dead Time

Generally, a lidar signal detection system has two components: the lidar signal detectors, or PMTs, and the signal processing system. The signal processing system is a multichannel scalar counter which records the number of collected backscattered photons as a function of altitude. Signal processing modes for detecting the backscattered signal can be separated into analog and digital.

Analog recorders transform the PMT signal to a current and they can record the backscattered signal from lower altitudes as they will not saturate. Digital recorders use a photon

counting system and record the individual photons hitting the PMT. The digital mode is more suitable for high altitudes observations where the signal is weak. Therefore, the digital recorders are required for low-level light from high altitudes where returning photons are recorded over long periods of time (Kovalev and Eichinger, 2004) and they can provide a higher signal-to-noise ratios at those altitudes compared to the analog system.

The PMT for the lidar needs a specific amount of time to record and process a single photon counting event. If a second photon arrives during that interval of time the PMT will not process it and it may be lost or cause a pile-up effect within the PMT. This waiting time for a detector to discriminate and process two separate events is called "dead time"and is typically on the order of nanoseconds. Dead time may be due to counting electronics or limitations of the processing parts of the detector. The dead time effect mostly happens at high count rates and the resulting signal becomes lower than the true signal. A dead time correction should be used to calculate the true count rate in a region with high count rates. In the data analyses of atmospheric profiles, this correction is more important at lower altitudes where the rate of photon counting events is high compared to the greater heights where the signal is lower. There are two models to find a correction for the true number of photons due to the dead time effect: paralyzable and nonparalyzable models. Paralyzable dead time occurs when the arrival of a second photon during the dead time period extends the dead time from the time of the second event's arrival by another dead time period, preventing any subsequent photons from being "counted". Hence, the system is effectively "paralyzed". In a paralyzable system, the sampling time is longer than γ and the true count rates obey Poisson counting statistics as expected. The following equation shows the relation between the observed photocount (N_o) and the true photocount rate (N_t) in a paralyzable system (Donovan et al., 1993).

$$N_o = N_t \exp(-N_t \gamma). \tag{1.4}$$

Non-paralyzable dead times (Mielke, 2005) occur when an event happens after the γ interval, but the detection is not recorded due to having energy less than the discriminator level set by the system. In this scenario, several photons may "pile up" to create one photon

count in the system. The observed photocounts and true counts are related with

$$N_o = \frac{N_t}{1 + N_t \gamma}.$$
(1.5)

The lidar used in this thesis, Western's Purple Crow Lidar (PCL) has a counting system which is non-paralyzable. The above relation between the observed and true counts is valid when the denominator is less than about 1.25; above this point correction is not advised for the PCL lidar.

1.3.2 The Lidar Equation

The measurements of a lidar system are a time series of counts which can be converted to height (photocount profiles) and vary with height and time. The photocount profiles are proportional to the atmospheric density and are described by the "lidar equation" (Eq. 1.6). The lidar equation relates the number of backscattered photons detected by a lidar to the physical characteristics of the lidar and atmospheric properties such as molecular density and cross-section. Eq. 1.6 is the general form of the lidar equation used for all scattering types (Measures, 1992):

$$N(z) = \xi_{sys} \cdot \Gamma_{emitted}(z, \lambda_e) \Gamma_{return}(z, \lambda_r) \cdot O(z) \frac{p_{laser}}{(hc/\lambda_{laser})} \cdot \sigma_{backscatter} n(z) \cdot \frac{A}{4\pi z^2} \cdot \Delta t \cdot \Delta z + B(z).$$
(1.6)

Transmission is the opacity of the atmosphere to electromagnetic radiation where the transmissions in Eq. 1.6 are given by

$$\Gamma_{emitted}(z, \lambda_e) = exp^{-\tau_{emitted}}, \tau_{emitted}(z, \lambda_e) = \int_0^z \sigma_{ext}(\lambda_e) n(z) dz',$$
(1.7)

$$\Gamma_{return}(z, \lambda_r) = exp^{-\tau_{return}}, \tau_{return}(z, \lambda_r) = \int_0^z \sigma_{ext}(\lambda_r) n(z) dz'.$$
(1.8)

The other variables in the lidar equation are as follows, with all quantities in SI units.

N = number of returned photons which are detected by lidar (unit-less)

z = altitude above the detector (m)

ξ_{sys} = system specific receiver efficiency (unit-less)

Γ = transmittance of the photons through the atmosphere (unit-less, the value of transmittance is between zero and one)

τ = optical depth (unit-less)

$O(z)$ = overlap function of the receiver field of view (unit-less)

p_{laser} = Laser power at wavelength λ (W), $\frac{p_{laser}\Delta t}{hc/\lambda_{laser}}$ gives the number of emitted photons.

$\sigma_{backscatter}$ = scattering cross section of the molecules at the returning wavelength (m^2)

$\sigma_{ext}(\lambda_e)$ = extinction cross section at the emitted wavelength (λ_e) (m^2)

$\sigma_{ext}(\lambda_r)$ = extinction cross section at the returning wavelength $(\lambda_r)(m^2)$

$n(z)$ = number density of scatterers in the atmosphere (m^{-3})

A = area of telescope where $A/(4\pi z^2)$ presenting the effective area of the primary telescope (m^2)

Δt = time over which measurements are collected (s)

Δz = spatial range over which photons in a bin are integrated (m)

$B(z)$ = background counts (unit-less)

We can rewrite Eq. 1.6 as:

$$N_t(z) = C\psi(z)\frac{n(z)}{z^2} + B(z), \tag{1.9}$$

which

$$C = \xi_{sys}\frac{p_{laser}}{(hc/\lambda_{laser})}\frac{A}{4\pi z^2}\Delta t\Delta z, \tag{1.10}$$

and

$$\psi(z) = \Gamma_{emitted}(z, \lambda_e)\Gamma_{return}(z, \lambda_r)O(z)\sigma_{backscatter}. \tag{1.11}$$

Where C is a constant that depends on the properties of the lidar and is explained below. The function $\psi(z)$ includes the height-dependent parameters of atmospheric transmission, the Rayleigh scatter cross section, detector nonlinearities and geometric overlap.The lidar equation (Eq. 1.6) is derived assuming that there is a single scattering event for each photon, the density of the atmosphere in a layer of thickness Δz is constant, and the laser pulse is shorter than the recording time of an altitude bin. The lidar equation can be modified based

on the type of scattering event. For example, in Rayleigh scattering, the emitted transmission is equal to the return transmission because the wavelength does not change. Also, the cross section is summation of Rayleigh-scatter and ozone cross section. However, for a Raman scattering event, the transmittance differs because the wavelength of the backscattered photon is not the same as the wavelength of the emitted photon and one must also consider the aerosol cross section. It is not practical to calculate absolute measurements of density $(n(z))$ due to several factors like the fluctuating laser power with time, changing laser beam alignment, effect of ozone on the backscatter cross section, and the effect of aerosols and clouds on the atmospheric transmission. But it is possible to calculate relative density using Eq. 1.12 because the receiver efficiency, overlap, laser power, A and scattering cross section cancel out. Also, above 25 km the effect of ozone and aerosols are small enough that we can assume $\tau(z) = \tau(z_0)$, thus:

$$n(z) = n(z_0)\frac{N(z)}{N(z_0)}\frac{\tau(z_0)^2}{\tau(z)^2}\frac{z^2}{z_0^2} \qquad (1.12)$$

Various lidar system parameters and physical constants affect the total number of received photocounts and are independent of altitude. The combination of these parameters is called the lidar constant (C) and in our definition includes: the number of photons emitted by each laser pulse, the optical efficiency, the detection efficiency of the photomultipliers, atmospheric Rayleigh scatter cross section and speed of light. All quantities are system dependent except the speed of light, and can in fact change for a specific instrument as hardware changes, such as changing the laser transmitter.

When the pressure gradient of an air parcel in the atmosphere is in balance with its gravitational force, the atmosphere is in hydrostatic equilibrium, and is dynamically and thermally stable. The hydrostatic equilibrium equation is:

$$\frac{dP}{dz} = -\rho(z)g(z), \qquad (1.13)$$

where $P(z)$ is the atmospheric pressure, $\rho(z)$ is the density and $g(z)$ is the acceleration due to gravity. The mean molecular mass of air is considered to be constant within the 30 to 80 km altitude range. However, the mean molecular mass can vary with altitude above 80 km due to an increase in the relative amount of atomic oxygen, and this variation affects

the temperature retrieval, both through the change in mean molecular mass and the effect of composition changes on the Rayleigh-scatter cross section. In the traditional analysis technique, the lidar equation is combined with the assumption of hydrostatic equilibrium to calculate the temperature.

1.3.3   Rayleigh Lidar

Rayleigh scattering is an elastic scattering that occurs when the size of a particle is much smaller than the emitted photon's wavelength. The Rayleigh scattering intensity is proportional to λ^{-4}. In Rayleigh scattering, the incident photon excites the electron to an unstable energy level and decays to the same initial level energy quickly, thereby emitting a photon with the same wavelength of the incident photon. Rayleigh lidars utilize Rayleigh scattering to probe the atmosphere between 25 and 110 km. Radiosondes are able to measure atmospheric parameters from surface to 35 km, resonance lidars between 80 and 105 km, incoherent scatter radars from 100 to 500 km, and MST radars cover the range from surface up to 100 km except the range between 30 and 60 km. Rayleigh lidars in particular are well suited for measuring the middle atmosphere temperature. Rayleigh lidars are capable of measuring atmospheric relative density continuously with high spatial resolution, however, they are limited to measuring only during clear nights. These properties make Rayleigh lidars a good option for researchers to study the middle atmosphere temperature and density. Satellites also cover the range of the middle atmosphere and lower upper atmosphere but they only collect measurements for short periods of time in each location and they are not ideal for temporal studies; however, they provide good measurements along the direction of satellite track. The Purple Crow Lidar, used in this thesis, is one example of a Rayleigh lidar.

The Purple Crow Lidar

The PCL is a Rayleigh-Raman lidar which is located since 2012 at the Environmental Science Western Field Station (43.07 ° N, 81.33 ° W, 275 m altitude) near The University of Western Ontario in London, Canada. The PCL was previously located at the Delaware Observatory

(42.52 °N , 81.23 °W), from 1992 to 2010 (Sica et al., 1995, 2000; Argall et al., 2000). At present, the PCL is comprised of 6 channels: the Raman channel with 532 nm beam to measure the temperature of the upper troposphere and lower stratosphere and the digital and analog Rayleigh channels to measure temperature in the upper mesosphere and lower thermosphere. A summary of the PCL's properties is listed in Table 1.1 and Fig. 1.3 shows diagram of the PCL. The PCL's receiver is a liquid mercury mirror with a diameter of 2.65 m. From 1994 to 1998, the PCL used a single detection channel (the High Level Rayleigh (HLR) channel) over the range of 30 to 110 km (Sica et al., 1995). In 1999, a Low Level Rayleigh (LLR) channel was added, which is nearly linear above 25 km (Sica et al., 2000).

Table 1.1: The PCL system parameters.

	Delaware Observatory	Echo Base Observatory
Operation period	1992-2010	2012-now
Location	42.52 N , 81.23 W	43.07 N, 81.33 W
Height above sea level (m)	225	275
laser wavelength (nm)	532	532
Energy (mJ/pulse)	600	1000
Repetition rate (Hz)	20	30
Power (W)	12	30
Aperture diameter (m)	2.65	2.65
Rayleigh bin size (m)	24	7.5
Raman bin size (m)	250	24
Water vapour bin size (m)	250	24
Mirror diameter (m)	2.56	2.56
Mirror focal length (m)	5.17	5.17

At the bottom (24-40 km) of the Rayleigh measurement profiles the count rate is very high and saturation occurs. The saturation prevents accurate measurements at the bottom, and thus, a neutral density filter is used in front of the Rayleigh PMT to extend the range of photon counting to keep the count rate linear. The Low Level Rayleigh channel is used to record measurements from 25 to 50 km to increase the accuracy of the measured Rayleigh
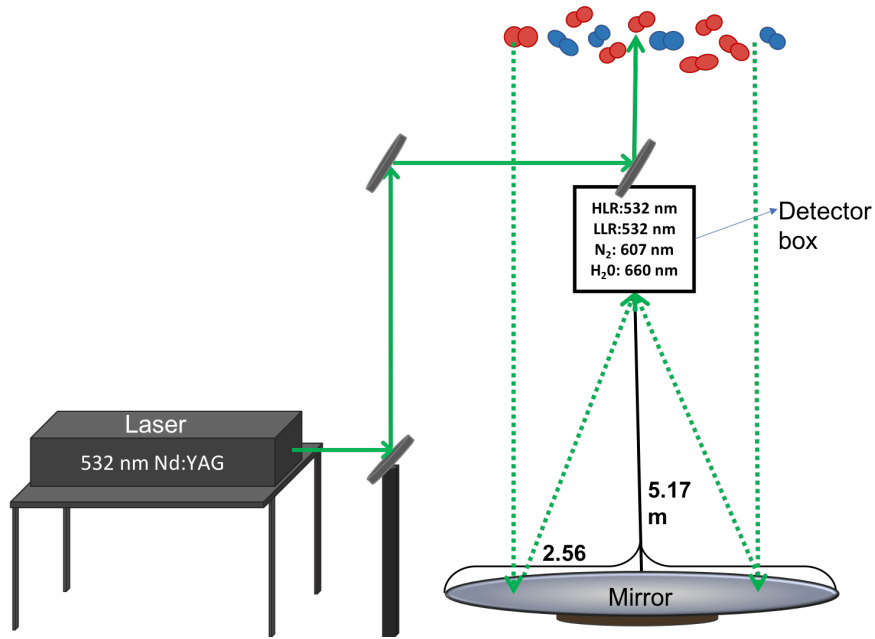
Figure 1.3: A schematic of the Purple Crow Lidar. The green dashed lines represent the backscattered photon path. The channels inside the detector box are: two Rayleigh channels (HLR and LLR) at 532 nm, a Raman nitrogen channel at 607 nm, and a Raman water vapour channel at 660 nm. The diameter of the telescope is 2.56 m with a focal length of 5.17 m.

temperatures at the lower altitudes while the High Level Rayleigh channel is operated to measure from 30 to 120 km. Figure 1.4a and b show the HLR and LLR PCL photocount measurements for a typical night (24 March 2002). The lidar system operates during the night when the background light is minimal (background light due to the moon is negligible). The average operating time is around 5.5 hours per night. Over the course of the night, clouds may pass over the PCL which can reduce the count rate and ultimately can affect the precision of the signal. During these conditions, the PCL continues recording the signal, but these parts of the data that heavily affect the signals are not useful and they are eliminated during analysis. Fig. 1.4 shows measurements collected for a total of 456 minutes on the night of 24 March 2002. It can be seen in this figure that clouds are passing over the lidar around minute 370 of operations and the signal is weakened. These bad scans are removed from the measurements shown in Figures 1.4c and d. The useful number of scans (corrected counts) are 350 minutes. The sum of all these scans is shown in Figures 1.4e and
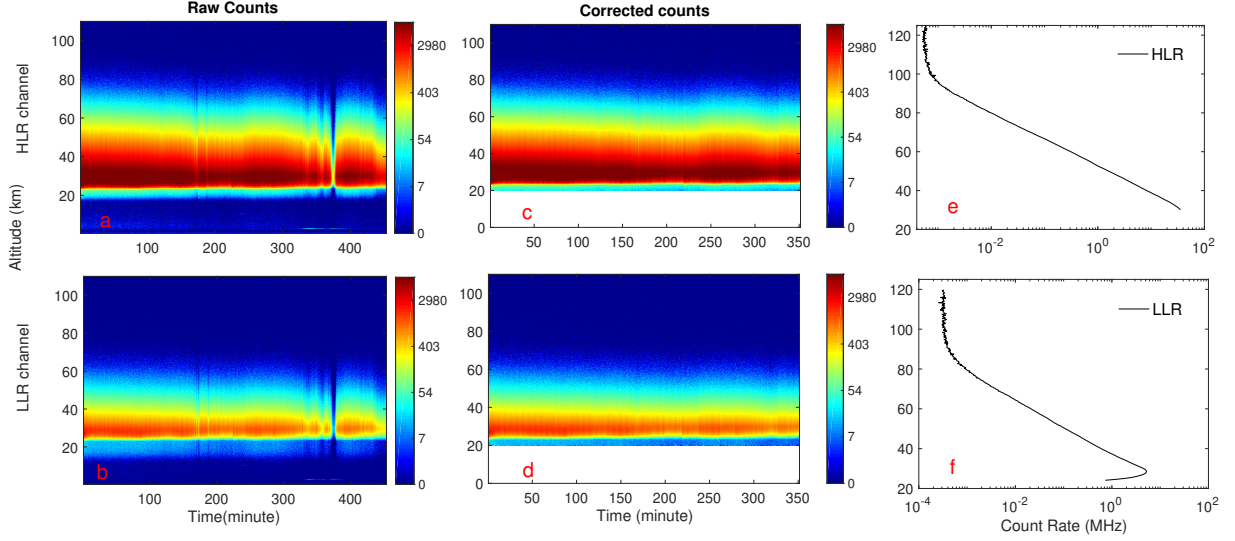
Figure 1.4: a) HLR and b) LLR PCL rawcount measurements (cts/bin/s) for 24 March 2002, c) HLR and d) LLR corrected counts (cts/bin/s), e) HLR and f) LLR coadded corrected profiles (MHz). The color-bar values are corresponding corrected count rates of e^1, e^2, e^3 and so on.

f for the LLR and HLR channel. At the bottom of the Rayleigh range in Fig. 1.4 (around 25 km) the maximum count rate in the LLR channel is linear, therefore the LLR can be used to correct the nonlinearity in the HLR signal due to the dead time. At the higher altitudes of the measurement profiles, the signal-to-noise ratio is small. This is because the backscattered signal is proportional to density which exponentially decreases with height, therefore causing the signal-to-noise ratio to decrease at the top of the photocount profile. Averaging the pulses or integrating them is often used to increase the measurement altitude range of the system by increasing the signal-to-noise ratios. The integration or averaging can be done over time and/or by altitude bin; however, while integration increases the signal-to-noise ratio, it decreases the resolution (Kovalev and Eichinger, 2004). The lidar scans are usually integrated over time and height in order to accurately calculate the temperature in higher altitudes. A typical PCL temperature profile for the climatology is calculated up to 100 km, using signal integrated in time over an entire night (5.5 hours on average) and integrating in height by 1 km. For higher temporal-spatial studies of atmospheric variations this time can be as short as a few minutes and a few hundred meters.

1.3.4 Raman Lidar

Raman scattering is a type of inelastic scattering where the backscattered photon is at a different wavelength than the emitted photon. In Raman scattering, the laser photons excite the electrons of a molecule to an upper stable energy level. Then the excited photon decays to a lower energy level spontaneously and emits a photon with a wavelength proportional to the energy differences of the excited and final state. Electronic, vibrational, and rotational states are three types of energy levels that can emit a photon when a transition between energy states occurs. The electronic energy transition happens between the orbital levels of a molecule and requires several eV to move an electron between electronic states. The vibrational transition corresponds to vibrations of the nuclei and has energy states on the order of 0.1 eV. Rotational transitions are associated with the rotation of a nuclei around its center of mass with levels of energy on the order of 0.001 eV (Bransden et al., 2000). The energy of a Raman-scattered photon is much smaller than the energy of a Rayleigh-scattered photon.

Vibrational Raman lidar

Above $30\,\mathrm{km}$, where the scattering mostly is Rayleigh, the atmospheric transmission in the lidar equation (Eq. 1.6) is constant with height. However, below $30\,\mathrm{km}$, this assumption is not valid as the atmospheric transmission depends on Rayleigh, Mie and ozone scattering (Keckhut et al., 1990). Almost 78% percent of the atmosphere below $80\,\mathrm{km}$ is comprised of nitrogen molecules. Therefore, it is possible to measure the temperature below 30 km using the N_2 density and vibrational Raman scattering from the N_2 molecule (Keckhut et al., 1990). The PCL Raman-shifted wavelength for N_2 molecule due to vibrational transition is $607\,\mathrm{nm}$. Iserhienrhien et al. (2013) and Jalali (2014) used the PCL nitrogen channel measurements to calculate the PCL temperature climatology between $10\,\mathrm{km}$ and $30\,\mathrm{km}$.

Rotational Raman lidar

There are two branches or energy states (Stokes and anti-Stokes) which are symmetrically located on both sides of the Rayleigh line. These branches are due to the Raman rotational

spectrum. Stokes scattering occurs when a photon is absorbed by a molecule and then the photon is red-shifted to a longer wavelength. The anti-Stokes scattering is the opposite of the Stokes scattering and the wavelength of the re-emitted photon is decreased. The frequencies of Stokes and anti-Stokes scattering are given in Eq. 1.14, where the frequency shift between the exciting and scattering line ($\Delta\nu$) is presented in Eq. 1.15 (Cooney, 1972).

$$\nu_s = \nu_1 - \mid \Delta\nu \mid,$$
$$\nu_a s = \nu_1 + \mid \Delta\nu \mid \tag{1.14}$$

$$\Delta\nu = 4\beta(J' + \frac{3}{2}). \tag{1.15}$$

Here β is the molecular rotational constant and J' is the rotational quantum number of the lower state. The intensity of each individual rotational Raman line depends on the temperature of the molecule. Therefore, the atmospheric temperature can be calculated by using the pure rotational Raman scattering of N_2 and O_2 molecules (Arshinov et al., 1983). The atmospheric temperature can be calculated by measuring the intensity of two rotational Raman lines with opposite temperature dependency, as the ratio of these two lines is a function of the temperature. Rotational Raman lidar can measure temperature up to around 30 km. Above about 25 km altitude, Rayleigh scattering is large and the the contribution to the scattering from aerosols becomes negligible, while the Raman and Mie scattering is orders of magnitude smaller. Thus, above about 25-30 km Rayleigh-scatter measurements are better suited for temperature retrievals.

1.3.5   Resonance Fluorescence Lidar

Rayleigh lidars measure molecular scattering from air in the mesosphere and lower thermosphere to calculate temperature, but resonance lidars use scattering from metals (Na, P, Fe, Li, and Ca) released by meteors between 80 to 110 km altitude. Metals like Na, K, Fe, Ca and Ca^+ are deposited in the MLT region by meteors when they burn up in the atmosphere (Plane, 1991). These metals do not exist below 85 km as the air density is high. However, when metallic atoms react with other molecules they form compounds and they act as condensation nuclei for clouds in the middle atmosphere. Eventually, after roughly 4 years, they reach the ground (Plane et al., 2015). Resonance fluorescence is a process

for ions or molecules where the energy of an incident photon coincides with the transitional energy of the atom which causes a photon at the same or longer wavelength to be re-emitted. When implemented for lidars, only re-emission at the same wavelength is considered (Abo, 2005). Resonance fluorescence lidars can also derive kinetic temperature and wind velocity from the thermal broadening and Doppler shift of measured spectra (Arnold and She, 2003). Sodium lidars are a type of resonance fluorescence lidar which use the resonant scattering of the sodium layer. Na atoms in the MLT region absorb the photons and they are excited to higher energy level, then they re-emit a photon as they return to the ground energy level. The temperature accuracy is limited by our knowledge of the received photon noise, transmitted wavelength, and line width (Bills et al., 1991; Krueger et al., 2015).

Typically, Rayleigh lidars don't measure as high in altitude as sodium lidars. Several Rayleigh lidar temperature climatologies have been calculated e.g. Leblanc et al. (1998), Argall and Sica (2007) and have been compared with sodium temperature climatologies such as those in She et al. (2000), States and Gardner (2000) and Yuan et al. (2008). However, the PCL can reach into the sodium layer. We have compared our temperature climatologies with sodium lidars in Chapter 2.

1.4 Measuring Temperature with Lidar

In this section, we briefly review the temperature retrieval methods that are used in the following chapters: the traditional method and the Optimal Estimation Method (OEM). Each method has its own benefits and deficiencies. Both of these methods start with a lidar return which is proportional to density and then find temperature using the lidar equation, the assumption of hydrostatic equilibrium, and the Ideal Gas Law.

1.4.1 The Traditional Method

In 1980, Hauchecorne and Chanin (HC) presented a robust method to retrieve temperature from Rayleigh lidar measurements (Hauchecorne and Chanin, 1980). The HC method uses the assumption of hydrostatic equilibrium, the Ideal Gas Law, and the lidar equation to define a relationship between the measured lidar signal and temperature at each altitude in

the lidar's range. The hydrostatic equilibrium is given by Eq. 1.16:

$$\frac{dp}{p} = -\frac{M}{R}\frac{g(z)}{T(z)}dz. \tag{1.16}$$

This equation can be integrated over layers with a thickness $\triangle z$ that is bounded by $z - \frac{\triangle z}{2}$ and $z + \frac{\triangle z}{2}$ as follows:

$$\log\left(\frac{P(z_i + \frac{\triangle z}{2})}{P(z_i - \frac{\triangle z}{2})}\right) = -\int_{z_i - \frac{\triangle z}{2}}^{z_i + \frac{\triangle z}{2}} \frac{M}{R}\frac{g(z)}{T(z)}dz. \tag{1.17}$$

Equation 1.17 is not a linear relation in terms of temperature. In order to find a linear relation between the temperature and lidar observations (density), we assume an isothermal atmosphere and constant gravity within each layer. Then Eq. 1.17 can be simplified at each altitude (z_i), $i = 1$ to N:

$$\frac{P(z_i + \frac{\triangle z}{2})}{P(z_i - \frac{\triangle z}{2})} = exp\left(-\frac{Mg(z_i)}{RT(z_i)}\Delta z\right). \tag{1.18}$$

The derived temperature expression is then (Hauchecorne and Chanin, 1980):

$$T(z_i) = \frac{Mg(z_i)\triangle z}{R\log(\frac{P(z_i - \frac{\triangle z}{2})}{P(z_i + \frac{\triangle z}{2})})}. \tag{1.19}$$

In Eq. 1.19, $T(z_i)$ is temperature (in Kelvins), z_i is the ith altitude levels, M is mean molecular mass of air (in kilograms/mole), $g(z_i)$ is the acceleration of Earth's gravity, P is atmospheric pressure and R is the ideal gas constant. The HC method assumes that $T(z_i)$ and consequently P are constant within each layer. The pressure values at the top and bottom of a defined layer can be calculated using the hydrostatic equilibrium equation upon downward integration as:

$$P(z_i + \frac{\triangle z}{2}) = P(z_n + \frac{\triangle z}{2}) + \sum_{j=i+1}^{n} \rho(z_j)g(z_j)\triangle z, \tag{1.20}$$

and

$$P(z_i - \frac{\triangle z}{2}) = P(z_i + \frac{\triangle z}{2}) + \rho(z_j)g(z_j)\triangle z, \tag{1.21}$$

where the term $P(z_n + \frac{\triangle z}{2})$ is the pressure at the Nth layer (the highest layer). In Eq. 1.20 and 1.21, $\rho(z_j)$ is the atmospheric density profile

$$\rho(z_j) = \frac{n(z)}{N_A}, \tag{1.22}$$

27

where N_A is Avogadro's number and $n(z)$ is atmospheric number density (particles/m^3) calculated from the lidar equation (Eq. 1.9). We can rearrange and rewrite Eq. 1.9 using these assumptions and merging $\psi(z)$ in C since ψ is constant with height:

$$\rho(z_i) = C(N(z_i) - B(z_i))(z_i)^2. \tag{1.23}$$

Equation 1.23 shows that the Rayleigh lidar signal is proportional to the atmospheric mass density. In Eq. 1.23, the lidar constant (C) cannot be determined precisely due to the uncertainties in the parameters that comprise the lidar constant, and $N(z_i)z_i^2$ is the relative density profile. Using the relative density profile, the relative temperature profile can be calculated. It is necessary to have the lidar constant in Eq. 1.23, in order to find atmospheric density profile at all altitudes from lidar measurements. The lidar constant in Eq. 1.23 can be calculated by scaling the lidar photocounts between an altitude range where the lidar photocount is linear with high signal-to-noise ratio and (45-65 km) to the corresponding density values usually taken from an atmospheric model like the CIRA-86. The relative pressure profiles can be calculated using the density profile through Eq. 1.20 and 1.21. In order to initiate the pressure relation from top to bottom, the pressure at the highest altitude of the mass density profile is required. This pressure is usually obtained from a model and is called "seed" or "tie-on" pressure. A "seed temperature" could also be used in the above temperature retrieval algorithm instead of a "seed pressure". The ratio of the calculated relative pressure profile to actual pressure profile is the same as the relative mass density profile to the actual atmosphere mass density profile (Eq. 1.24):

$$\frac{P(z_i)}{P_{atmos}(z_i)} = \frac{\rho(z_i)}{\rho_{atmos}(z_i)} = K. \tag{1.24}$$

Finally, the temperature profile can be calculated using eq. 1.19 by applying ideal gas law to the relative mass density and pressure profile (Eq. 1.25).

$$T(z_i) = \frac{P(z_i)}{R\rho(z_i)} = \frac{KP_{atmos}(z_i)}{RK\rho_{atmos}(z_i)} = \frac{P_{atmos}(z_i)}{R\rho_{atmos}(z_i)}. \tag{1.25}$$

Both, the mass density and pressure profiles are relative in Eq. 1.25 but the calculated temperature is absolute. Using the seed value in Eq. 1.20 most likely cause an offset in the top of the calculated relative pressure profiles which depends how far the seed value

is from the actual atmospheric pressure. Atmospheric density increases as the downward integration proceeds in Eq. 1.20 and the second term becomes larger and dominates the first term, therefore, the seeding value uncertainty decreases.

The uncertainties due to seed temperature or pressure in the first term in Eq. 1.20 create uncertainties in the retrieved temperature profile. In the case of the PCL, the seed value is usually taken from the CIRA-86 (Fleming et al., 1988) model between 100 to 110 km. At these altitudes the density is very small and consequently the pressure is very low, therefore, the uncertainty in the seed value is high and can have very large variations over time.

Leblanc et al. (2016) used the Monte Carlo technique to calculate the temperature uncertainty due to the seed pressure and they presented their result based on the temperature uncertainty due to 1% uncertainty in the seed pressure. It is necessary to know the variation of atmospheric pressure (which is directly proportional to temperature) in the region that seed pressure is chosen and the effect of the seed pressure on the temperature retrieval. To investigate the amount of temperature variation due to variation of seed pressure, the percent difference of CIRA-86 temperature profiles from the PCL temperature climatology (Jalali et al., 2018) was calculated (Fig. 1.5) for each month at all altitudes of the climatology. The details of the methodology to calculate these figures will be discussed in Section 1.4.2 and Chapter 2.

The annual variation in the percent difference between CIRA-86 and the PCL temperature climatology was calculated by taking the average of the percent differences between 100 and 110 km (Fig. 1.6). The differences in temperature between CIRA-86 and PCL were used to study how the consequent variations in the seed pressure would effect the temperature retrieval for a typical PCL temperature profiles (March 24 2002). The PCL temperature profiles are calculated using ±2, 4, 8 and 10% variation in the seed pressure (Fig. 1.7 A) and the difference between the temperatures using the perturbed seed pressure with the original temperature profile is calculated in Fig. 1.7b. The seed pressure altitude for this night is close to 104 km. The temperature difference due to the ±2% up to ±10% is between 4.5 and 22.5 K.

Due to the high uncertainties caused by estimating the pressure or temperature from a model, the top 10 to 15 km (on the order of two scale heights) are typically eliminated
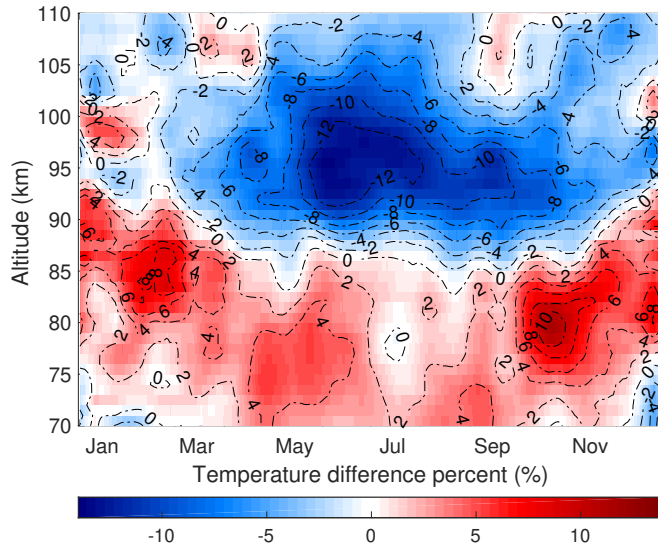
Figure 1.5: The temperature percent difference between the CIRA-86 model and the PCL temperature climatology using the PCL and CIRA-86 temperature climatologies.

from each temperature profile to achieve accurate results. Hauchecorne and Chanin (1980) presented that the seed pressure uncertainty is proportional to the density at the highest altitude which is proportional to each height below. Therefore, the seed pressure uncertainty decreases with increasing the density.

1.4.2 The Optimal Estimation Method

The Optimal Estimation Method (OEM) is an inverse method which was developed by Rodgers (2011) for remote atmospheric measurements. It is now well-known in the atmospheric science field, especially in data assimilation and satellite (Marks and Rodgers, 1993; Palmer and Barnett, 2001; Watts et al., 2011) retrieval measurements as well as radiometer observations (Güldner and Spänkuch, 2001; Haefele et al., 2099). The method has only recently been applied to active sounding measurements. Povey et al. (2014) used the OEM to retrieve aerosol backscatter and extinction from lidar measurements. Then, Sica and Haefele (2015) presented the method as a solution to some of the shortcomings of the previously mentioned Rayleigh temperature retrieval techniques. Sica and Haefele (2015) used a first-
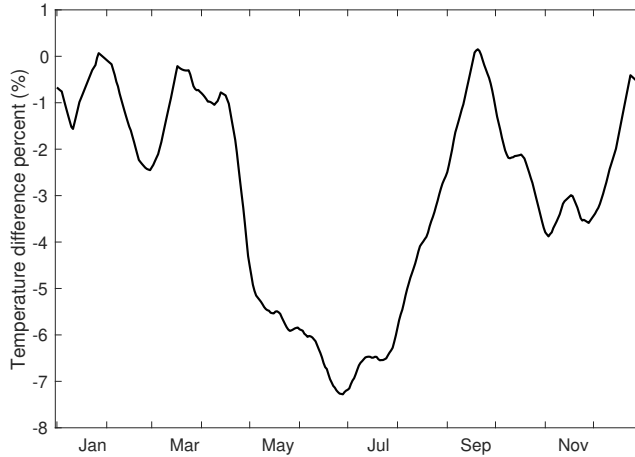
Figure 1.6: The average of the percent differences in temperature between 100 and 110 km shows the annual variation of the difference between the CIRA-86 and PCL temperature climatology.

principle OEM to retrieve temperature from Rayleigh-scatter lidar measurements. Here, first principle means that the OEM analysis is done from uncorrected (level 0) measurements to avoid introducing artifacts due to instrument corrections.

The OEM consists of two primary components: measurements and determined model parameters (Rodgers, 2011). The relationship between these components can be modeled in a function known as the forward model ($\mathbf{F}(\mathbf{x})$).

The linear OEM relationship can be written as:

$$\mathbf{y} = \mathbf{F}(\mathbf{x}, \mathbf{b}) + \epsilon, \tag{1.26}$$

where $\mathbf{y}$ is the measurement vector, $\mathbf{x}$ is the state vector, $\mathbf{b}$ is the model parameter vector, and ϵ is the measurement noise. The state vector contains the retrieved quantities; henceforth I will call this the retrieval vector. The noise in lidar measurements implies that the measurements have uncertainties that have a distribution of possible values. The state vector is retrieved and contains the temperature profile and some instrument parameters like detector dead time and background. The model parameter vector contains all other parameters needed to represent the measurements. The forward model is the lidar equation (Eq. 1.9), which is dependent on both the system hardware configuration and atmospheric

31
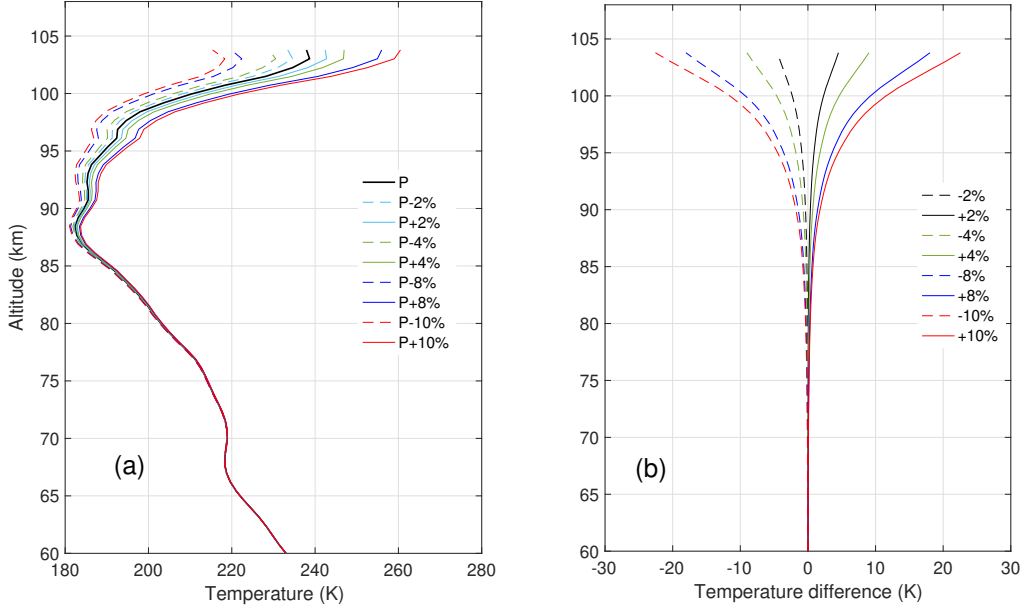
Figure 1.7: a) PCL temperature retrieval using the HC method on 20020324. Each profile corresponds to a seed pressure while the black temperature profile used the original seed pressure and other colors show $\pm$ 2, 4, 8 and 10% of the original seed pressure. b) The temperature difference between the temperature profiles using the original seed pressure versus the varying seed pressure. This figure is adapted from Gross et al. (1997) and Khanna et al. (2012).

properties. The measurement noise in lidar measurements implies that the measurements have uncertainties that have a Gaussian distribution of possible values represented by ϵ. It is necessary to mention that lidar photocounts follow Poisson statistics and the Poisson distributions with high enough photocounts approximates a normal distribution. Sufficiently high (i.e. > 10 cts/bin/s) exist for the entire range of lidar photocounts below the lower thermosphere.

The theory of the optimal estimation method is formulated in terms of Bayesian inference with Gaussian statistics. Bayes' theorem (Bayes et al., 1964) is given as:

$$\underbrace{P(x|y)}_{\text{Posteriori}} = \frac{\overbrace{P(y|x)}^{\text{Likelihood}}\overbrace{P(x)}^{\text{Priori}}}{\underbrace{P(y)}_{\text{Normalizing constant}}}. \tag{1.27}$$

In equation 1.27, $P(x|y)$ is known as the *a posteriori* term and is the probability of a random variable x (or hypothesis x) given an observation y. This term gives our complete state of knowledge of the wanted parameters given all of the available data. $P(y)$ is the probability of collecting the data under all possible hypotheses and normalizes the total probability of $P(x|y)$. The normalizing constant in following relations has been neglected. $P(x)$ is the background context or any available underlying information and knowledge about x prior to the arrival of data y, otherwise known as *a priori* information. $P(y|x)$ is the probability of getting y if the state were x or if the hypothesis x were true. The purpose of Bayes' theorem is to find a way to update our current state of knowledge of x, after the arrival of some data measurements y. The Bayesian approach is applicable when modeling time varying systems and one of the advantages of the Bayesian approach is that least squares maximum likelihood results can be achieved as special cases of the Bayesian results. Using Bayes' theorem, the most likely state can be found based on measurements and their uncertainties, as well as *a priori* information.

By using Bayes' theorem and approximating all parameters with a Gaussian probability density function (PDF), the retrieved states can be found by using the backscattered photons detected by the lidar. OEM solves the inverse problem, that is, a problem which uses the desired retrieval parameters to reproduce the measurements via a forward model which contains all the important physics and instrument effects. Here we retrieve temperature using photon counts measurements, with the forward model based on the lidar equation (Eq. 1.9). However, in order to solve the inverse problem using Bayes theorem we also need *a priori* profile, or a "first guess", for the retrieval parameters. We can find *a priori* information from different sources, for example: other instruments' measurements, climatologies, and meteorological models.

The solution of the retrieval inverse problem is constrained by *a priori* information. The optimum estimate for the probability state $\hat{\mathbf{x}}$ is found by minimizing equation 1.28, otherwise known as the "Cost" function.

$$\text{cost} = [\mathbf{y} - \mathbf{F}(\hat{\mathbf{x}}, \mathbf{b})]^T \mathbf{S}_\epsilon^{-1} [\mathbf{y} - \mathbf{F}(\hat{\mathbf{x}}, \mathbf{b})] + [\hat{\mathbf{x}} - \mathbf{x_a}]^T \mathbf{S_a}^{-1} [\hat{\mathbf{x}} - \mathbf{x_a}]. \tag{1.28}$$

where $\mathbf{S}_\epsilon$ is the covariance of the measurements, $\mathbf{x_a}$ is the *a priori* vector, and $\mathbf{S_a}$ is the *a*

priori covariance. Minimizing the cost function produces the retrieval solution ($\hat{\mathbf{x}}$), where the solution is then the maximum *a posteriori* solution based on the PDFs and is given by

$$\hat{\mathbf{x}} = \mathbf{x_a} + (\mathbf{K}^T\mathbf{S}_\epsilon^{-1}\mathbf{K} + \mathbf{S_a}^{-1})^{-1}\mathbf{K}^T\mathbf{S}_\epsilon^{-1}(\mathbf{y} - \mathbf{F}(\mathbf{x_a})) = \mathbf{x_a} + \mathbf{G}(\mathbf{y} - \mathbf{F}(\mathbf{x_a})), \qquad (1.29)$$

where $\mathbf{K}$ refers to the Jacobian matrix, and $\mathbf{G}$ is the gain matrix. The gain matrix describes the sensitivity of the retrieval to the observations:

$$\mathbf{G} = \frac{\partial\hat{\mathbf{x}}}{\partial\mathbf{y}} = (\mathbf{K}^T\mathbf{S}_\epsilon^{-1}\mathbf{K} + \mathbf{S_a}^{-1})^{-1}\mathbf{K}^T\mathbf{S}_\epsilon^{-1}. \qquad (1.30)$$

The two terms in Eq. 1.30 show the sensitivity to the measurement and *a priori*, respectively. One of the advantages of the OEM is that in addition to obtaining a retrieval vector, the method also provides diagnostic tools and a full uncertainty budget. The primary diagnostic tool is the averaging kernel matrix ($\mathbf{A}$) which represents the sensitivity of the retrieved state to the true state. At each retrieval grid point (level or altitude), the averaging kernel shows the sensitivity of the retrieval to the measurement. The full width at half-maximum (FWHM) of the averaging kernel at each altitude represents the vertical resolution. Equation 1.29 can be rewritten based on the averaging kernel as:

$$\hat{\mathbf{x}} = \mathbf{A}(\mathbf{x} - \mathbf{x_a}) + \mathbf{G}\epsilon. \qquad (1.31)$$

Equation 1.31 shows that if the $\mathbf{A}$ is unity at each altitude, the retrieval is sensitive only to the measurements, with no contribution from the *a priori* considering the gain matrix is the sensitivity of the retrieval to the observations. Wherever $\mathbf{A}$ is less than unity, the *a priori* is contributing to the retrieval and the extent of its contribution can be estimated using the measurement response. The averaging kernel also provides a means of calculating the number of degrees of freedom (dgf) in the retrieval by evaluating the trace of $\mathbf{A}$:

$$dgf = \text{Tr}(\mathbf{A}). \qquad (1.32)$$

Ideally, the contribution of the *a priori* is zero at all levels, and dgf equals the number of levels of the retrieved temperature profiles. If $\mathbf{u}$ is a vector with unit elements, $\mathbf{Au}$ is the sum along the rows of the averaging kernel and it can be used as a representation of the amount of

information coming from the lidar measurements and how much is as a result of the *a priori*. For example, an averaging kernel value of in the OEM retrieval represents no contribution of *a priori* information in the OEM retrieval and an averaging kernel with a value of 0 shows that all the OEM retrieval information comes from *a priori* knowledge. Figure. 1.8 represents an example of OEM temperature averaging kernel profiles calculated by the PCL (Fig. 1.8a) and MLS (Fig. 1.8b). In Fig. 1.8 the red lines are the measurement responses for each instrument which they are calculated from the sum over the raw of averaging kernel matrices. in Fig. 1.8a, every third averaging kernel is plotted to be clearer. The PCL is an active remote sensing instrument and the most of the averaging kernels from 25 km up to around 85 km are 1, which means all the temperature retrieval information comes from the PCL measurements at each level and clearly the measurement response is 1 as well. Above 85 km the averaging kernels decrease in magnitude and their width increases, meaning the vertical resolution of the retrieval decreases.

The MLS on the Aura satellite is a passive instrument and its typical averaging kernels are presented in (Fig. 1.8b). All of MLS averaging kernels are less than 1 at each level and they vary from 0.3 to maximum 0.7. The FWHM of the MLS averaging kernels are larger than those of the lidar and they vary with altitude. In Fig. 1.8, the vertical resolution for the PCL is 1 km up to 85 km and increases above it up to 3 km, however, the MLS vertical resolution is between 3.5 km and 10 km. The measurement response in Fig. 1.8b is almost 1 up to 0.005 mb, which means the retrieval comes from the MLS measurements but from a much wider altitude range than for the PCL. Therefore, **Au** was used as the cutoff height reference in the OEM instead of removing 1 or 2 scale heights from the top of each profile as in the traditional method. Values of **Au** equal to 0.9 and 0.8 are considered as a cutoff height. These values represent the fractional contribution of the measurements as compared to the *a priori* in the temperature retrieval and are generally recognized in the OEM community as levels above which the effect of the *a priori* is minimal.

In order to calculate the systematic uncertainties in the HC method, it is necessary to use a Monte Carlo method to propagate the uncertainties through the temperature retrieval (Leblanc et al., 2016). The OEM produces a complete uncertainty budget for all parameters in the temperature retrieval process on a profile by profile basis. The uncertainty
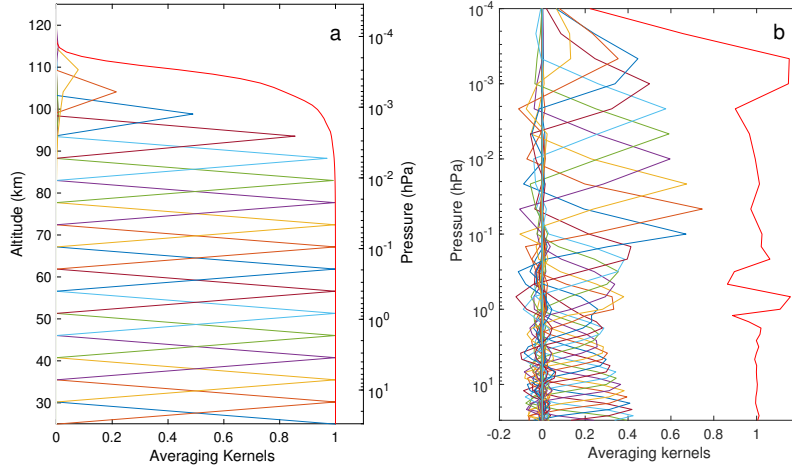
Figure 1.8: a) The PCL temperature averaging kernels for 24 May 2012 adapted from Sica and Haefele (2015). b) The MLS temperature averaging kernels at 70° latitude adapted from Schwartz et al. (2008). The red lines represent the measurement response.

budget includes the uncertainty due to the seed pressure and the other model parameters and measurement noise. The retrieval uncertainty due to measurement noise is:

$$\mathbf{S_y} = \mathbf{G}\mathbf{S}_\epsilon\mathbf{G}^T \tag{1.33}$$

where $\boldsymbol{S_\epsilon}$ is the covariance of the measurements and $\mathbf{G}^T$ is the transpose of the gain matrix $\mathbf{G}$. The OEM calculates the uncertainty due to the parameters inside the forward model by eq. 1.34:

$$\mathbf{S_b} = \mathbf{G}\mathbf{K_b}\mathbf{S_b}\mathbf{K_b}^T\mathbf{G}^T \tag{1.34}$$

In Eq. 1.34, $\mathbf{S}_b$ is the covariance of each forward model parameters and $\mathbf{K}_b$ is the jacobian of those parameters $(\dfrac{\partial \hat{\mathbf{F}}}{\partial \mathbf{b}})$. The lidar equation (Eq. 1.9) using the hydrostatic equilibrium plus non-paralyzable deadtime correction (Eq.1.5) can be used as a forward model to calculate the temperature. For Rayleigh-scatter lidar temperature retrievals, Sica and Haefele (2015) proposed the following form of the lidar equation as the forward model:

$$N_t(z) = C\frac{\psi(z)}{z^2}\frac{P_{hseq}(z)}{kT(z)} + B(z) \tag{1.35}$$

where

$$P_{hseq}(z) = P_0 \exp\left(\frac{1}{R}\int_z^{z_{top}} \frac{M(z')g(z')}{T(z')}dz'\right). \tag{1.36}$$

36

The Optimal Estimation Method
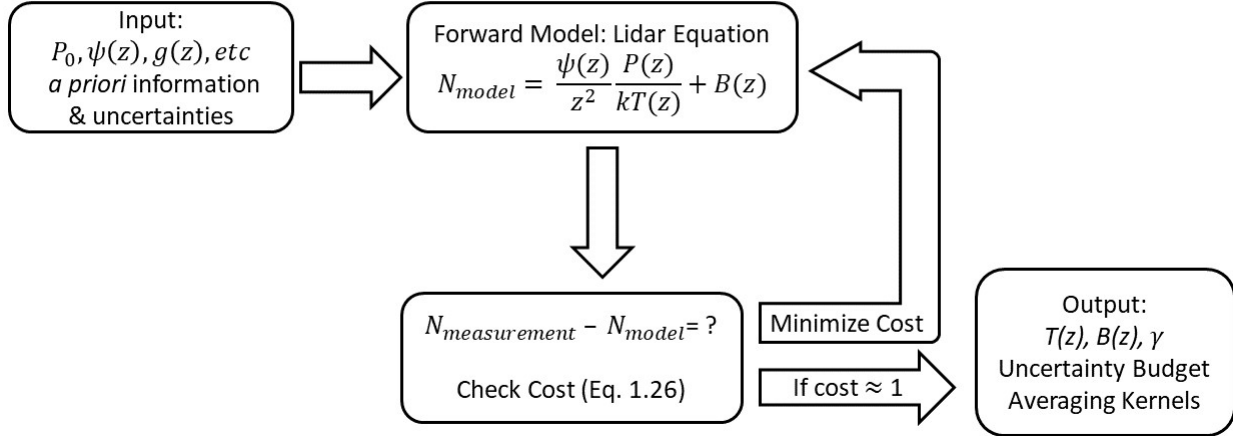
Figure 1.9: An overview of the OEM's iterative process.

Note the change of sign in the exponential term, which corrects a typo in Sica and Haefele (2015).

Practically, the OEM is often an iterative process since most forward models are somewhat non-linear. A linear solution would not require iterations and can be solved directly using Eq. 1.29. The basics of the process are shown in Fig. 1.9. First, all forward model input parameters are defined and calculated. These include parameters such as the ideal gas constant, mean molecular mass profiles, gravity profiles, and the choice of seed pressure. At this stage, the *a priori* temperature profiles are also calculated, as well as the *a priori* background and deadtime values. The uncertainties of all parameters (retrieved and forward model) are also defined or calculate and used to create the covariance matrices. The input values and *a priori* are then fed into the forward model to create the model photocount profile (N_{model}) which are compared to the measurement profile ($N_{measurements}$) using the cost function (Eq. 1.28). On the first iteration, the cost is typically very high, at which point the retrieval parameters are adjusted and the OEM iterates again. The iterations continue until the solution converges and the cost stabilizes - usually around a value of 1. The number of iterations varies depending on how far the initial guess is from the solution, but is usually less than 10. The final iteration produces the final retrieval values of the temperature, background, and deadtime as well as the averaging kernels and the uncertainty budget.

1.5 Overview of Thesis

In Chapter 2, we use the PCL temperature measurements from 1994 to 2013 to calculate a temperature climatology using the HC method and the OEM. These climatologies are compared to each other in order to validate the OEM. Also, the uncertainty budget for the PCL temperature climatology is calculated and is compared to the Monte Carlo uncertainty budget presented in Leblanc et al. (2016). Finally, the PCL temperature climatologies using OEM and HC are compared to available sodium lidar climatologies.

In Chapter 3, we will present a method that removes the effect of the *a priori* information from the final OEM lidar measurements. To validate the *a priori* removal method, we will use a typical PCL OEM temperature profile as well as OEM water vapour profiles from the RALMO lidar (located in Switzerland). The results for the water vapour will be compared with radiosonde measurements as well.

In Chapter 4, we will investigate the value in the calculation of averaging kernel matrices in the OEM . We use measurements taken from NASA and DWD (German Weather service) lidars during a campaign which was held in 2005. The averaged retrieved temperature from these two lidars will be compared with each other using the HC and OEM results. For the OEM comparison section, we also consider the averaging kernels of each lidar. Finally, the results will be compared to the MLS and SABER satellite temperature data.

Bibliography

Abo, Makoto. *Resonance Scattering Lidar*, pages 307–323. Springer New York, New York, NY, 2005. ISBN 978-0-387-25101-1. doi: 10.1007/0-387-25101-4_11.

Argall, P. S. and R. J. Sica. A comparison of Rayleigh and sodium lidar temperature climatologies. *Ann. Geophys.*, 25:27–35, 2007.

Argall, P. S., O. N. Vassiliev, R. J. Sica, and M. M Mwangi. Lidar measurements taken with a large-aperture liquid mirror: 2. The Sodium resonance-fluorescence system. *Appl. Optics*, 39:2393–2399, 2000.

Arnold, Kam S. and C. Y. She. Metal fluorescence lidar (light detection and ranging) and the middle atmosphere. *Contemporary Physics*, 44(1):35–49, 2003.

Arshinov, Yu. F., S. M. Bobrovnikov, V. E. Zuev, and V. M. Mitev. Atmospheric temperature measurements using a pure rotational raman lidar. *Appl. Opt.*, 22(19):2984–2990, Oct 1983.

Baldwin, Mark P. and Timothy J. Dunkerton. Stratospheric harbingers of anomalous weather regimes. 294(5542):581–584, 2001.

Bartman, F. L., L. W. Chaney, L. M. Jones, and V. C. Liu. Upper air density and temperature by the falling sphere method. *Journal of Applied Physics*, 27(7):706–712, 1956.

Bayes, T., Price, and Richard. An essay towards solving a problem in the doctrine of chance. *Anal. Chem.*, 53:370–418, 1964.

Bills, R. E., C. S. Gardner, and C. Y. She. Narrow band lidar technique for sodium temperature and doppler wind observations of the upper atmosphere. *Opt. Eng.*, 30, 1991.

Boville, B. A. and X. Cheng. Upper boundary effects in a general circulation model. *J. Atmos. Sci.*, 45:2592–2606, 1988.

Bransden, B.H., C. J. Joachain, and Charles J. Joachain. *Quantum Mechanics*. Benjamin-Cummings Pub Co, 2000.

Brasseur, Guy P. and Susan Solomon. *Aeronomy of the Middle Atmosphere Chemistry and Physics of the Stratosphere and Mesosphere*. Springer Netherlands, 2005.

Chapman, S. and S. R. C. Malin. Atmospheric tides, thermal and gravitational: Nomenclature, notation and new results. *Journal of the Atmospheric Sciences*, 27(5):707–710, 1970.

Colucci, S. J. Stratospheric influences on tropospheric weather systems. *J. Climate*, 67: 324–344, 2010.

Cooney, John. Measurement of atmospheric temperature profiles by raman backscatter. *Journal of Applied Meteorology*, 11(1):108–112, 1972.

Dickinson, Robert E. and Ralph J. Cicerone. Future global warming from atmospheric trace gases. *Nature*, 319:109–115, 1986.

Donovan, D. P., J. A. Whiteway, and A. I. Carswell. Correction for nonlinear photon-counting effects in lidar systems. *Applied Optics*, 32:6742–6753, 1993.

Dunkerton, Timothy. On the mean meridional mass motions of the stratosphere and mesosphere. *Journal of the Atmospheric Sciences*, 35(12):2325–2333, 1978.

Fleming, E. L., S. Chandra, M. R. Shoeberl, and J. J. Barnett. Monthly mean global climatology of temperature, wind, geopotential height and pressure for 0-120 km. *NASA Tech. Memo.*, NASA TM100697:85 pp, 1988.

Gerding, M., J. Höffner, J. Lautenbach, M. Rauthe, and F.-J. Lübken. Seasonal variation of nocturnal temperatures between 1 and 105 km altitude at 54 n observed by lidar. *Atmos. Chem. Phys.*, 8(24):7465–7482, 2008.

Gross, Michael R., Thomas J. McGee, Richard A. Ferrare, Upendra N. Singh, and Patrick Kimvilakani. Temperature measurements made with a combined rayleigh–mie and raman lidar. *Appl. Opt.*, 36(24):5987–5995, Aug 1997.

Güldner, J. and D. Spänkuch. Remote sensing of the thermodynamic state of the atmospheric boundary layer by ground-based microwave radiometry. *Journal of Atmospheric and Oceanic Technology*, 18(6):925–933, 2001.

Haefele, A., E. De Wachter, K. Hocke, N. Kämpfer, G. E. Nedoluha, R. M. Gomez, P. Eriksson, P. Forkman, A. Lambert, and M. J. Schwartz. Validation of ground-based microwave radiometers at 22 ghz for stratospheric and mesospheric water vapor. *Journal of Geophysical Research: Atmospheres*, 114(D23), 2099.

Hartley, D. E., J. T. Villarin, R. X. Black, and C. A. Davis. A new perspective on the dynamical link between the stratosphere and troposphere. *Nature*, 391:471–474, 1998.

Hauchecorne, A. and M. Chanin. Density and temperature profiles obtained by lidar between 35 and 70 km . *Geophys. Res. Lett.*, 7:565–568, 1980.

Hauchecorne, Alain, Marie-Lise Chanin, and P. Keckhut. Climatology and trends of the middle atmospheric temperature (33 - 87 km) as seen by rayleigh lidar over the south of france. *Journal of Geophysical Research: Atmospheres*, 96(D8):15297–15309, 1991.

Hedin, A. E. Extension of the msis thermosphere model into the middle and lower atmosphere. *Journal of Geophysical Research: Space Physics*, 96(A2):1159–1172, 1991.

Hocking, W. K. Temperatures using radar-meteor decay times. *Geophysical Research Letters*, 26(21):3297–3300, 1999.

Holton, J.R. *An Introduction to Dynamic Meteorology*. Elsevier, 2004.

Iserhienrhien, B., R. J. Sica, and P. S. Argall. A 7-year lidar temperature climatology of the mid-latitude upper troposphere and stratosphere. *Atmosphere-Ocean*, 51:532–540, 2013.

Jalali, A., R. J. Sica, and A. Haefele. A middle latitude rayleigh-scatter lidar temperature climatology determined using an optimal estimation method. *Atmospheric Measurement Techniques Discussions*, 2018:6043–6058, 2018. doi: 10.5194/amt-11-6043-2018.

Jalali, Ali. Extending and merging the purple crow lidar temperature rayleigh and vibrational raman climatologies. *Master's thesis, The University of Western Ontario*, 2490, 2014.

Keckhut, P., A. Hauchecorne, and M. L. Chanin. Midlatitude long-term variability of the middle atmosphere: Trends and cyclic and episodic changes. *Journal of Geophysical Research: Atmospheres*, 100(D9):18887–18897, 1995.

Keckhut, Philippe, M. L. Chanin, and A. Hauchecorne. Stratosphere temperature measurement using raman lidar. *Appl. Opt.*, 29(34):5182–5186, Dec 1990.

Khanna, Jaya, Justin Bandoro, R. J. Sica, and C. Thomas McElroy. New technique for retrieval of atmospheric temperature profiles from rayleigh-scatter lidar measurements using nonlinear iversion. *Appl. Optics*, 51:7945–52, 2012.

Kopp, M., M. Gerding, J. Höffner, and F. J. Lübken. Tidal signatures in temperatures derived from daylight lidar soundings above kühlungsborn (54n, 12e). *Journal of Atmospheric and Solar-Terrestrial Physics*, 127:37–50, 2015.

Kovalev, V. A. and W. E. Eichinger. *Elastic lidar. Theory, practice, and analysis methods.* John Wiley, 2004.

Krueger, David A., Chiao-Yao She, and Tao Yuan. Retrieving mesopause temperature and line-of-sight wind from full-diurnal-cycle na lidar observations. *Appl. Opt.*, 54:9469–9489, 2015.

Lastovicka, J., R. A. Akmaev, G. Beig, J. Bremer, and J. T. Emmert. Global change in the upper atmosphere. *Science*, 314:1253–1254, 2006.

Leblanc, T., R. J. Sica, J. A. E. Gijselvan , A. Haefele, G. Payen, and G. Liberti. Proposed standardized definitions for vertical resolution and uncertainty in the NDACC lidar ozone and temperature algorithms – part 3: Temperature uncertainty budget. *Atmos. Meas. Tech.*, 9(8):4079–4101, 2016.

Leblanc, Thierry, I. Stuart McDermid, Philippe Keckhut, Alain Hauchecorne, C. Y. She, and David A. Krueger. Temperature climatology of the middle atmosphere from long-term lidar measurements at middle and low latitudes. *J. Geophys. Res.-Atmos.*, 103(D14): 17191–17204, 1998.

Leblanc, Thierry, Thomas Trickl, and Hannes Vogelmann. *Lidar*, pages 113–158. Springer New York, New York, NY, 2013. ISBN 978-1-4614-3909-7. doi: 10.1007/ 978-1-4614-3909-7_7.

Lübken, F.-J., W. Hillert, G. Lehmacher, U.von Zahn, M. Bittner, D. Offermann, F.J. Schmidlin, A. Hauchecorne, M. Mourier, and P. Czechowsky. Intercomparison of density and temperature profiles obtained by lidar, ionization gauges, falling spheres, datasondes and radiosondes during the dyana campaign. *Journal of Atmospheric and Terrestrial Physics*, 56(13):1969 – 1984, 1994. Dynamic Adapted Network for the the Atmosphere.

Manabe, Syukuro and Fritz Moller. On the radiative equilibrium and heat balance of the atmosphere. *Monthly Weather Review*, 89(12):503–532, 1961.

Marks, Crispin J. and Clive D. Rodgers. A retrieval method for atmospheric composition

from limb emission measurements. *Journal of Geophysical Research: Atmospheres*, 98 (D8):14939–14953, 1993.

Marshall, John and R. Alan Plumb. *Atmosphere, Ocean and Climate Dynamics: An Introductory Text*. Elseveir, 2007.

Measures, R. M. *Laser Remote Sensing Fundamentals and Applications*. Krieger Publishing Company, Malabar, FL., 1992.

Meriwether, John W. and Andrew J. Gerrard. Mesosphere inversion layers and stratosphere temperature enhancements. *Reviews of Geophysics*, 42(3), 2004.

Licel Tech. *Analog + photon counting*. Mielke, B., http://licel.com/manuals/analogpc.pdf, 2005.

Palmer, Paul I. and John J. Barnett. Application of an optimal estimation inverse method to gps/met bending angle observations. *Journal of Geophysical Research: Atmospheres*, 106(D15):17147–17160, 2001.

Perlwitz, J. and N. Harnik. A new perspective on the dynamical link between the stratosphere and troposphere. *J. Climate*, 16:3011–3026, 2003.

Plane, John M. C. The chemistry of meteoric metals in the earth's upper atmosphere. *International Reviews in Physical Chemistry*, 10(1):55–106, 1991.

Plane, John M. C., Wuhu Feng, and Erin C. M. Dawkins. The mesosphere and metals: Chemistry and changes. *Chemical Reviews*, 115(10):4497–4541, 2015.

Polvani, Lorenzo M. and Darryn W. Waugh. Upward wave activity flux as a precursor to extreme stratospheric events and subsequent anomalous surface weather regimes. *Journal of Climate*, 17(18):3548–3554, 2004.

Povey, A. C., R. G. Grainger, D. M. Peters, and J. L. Agnew. Retrieval of aerosol backscatter, extinction, and lidar ratio from raman lidar with optimal estimation. *Atmospheric Measurement Techniques*, 7(3):757–776, 2014. doi: 10.5194/amt-7-757-2014.

Quiroz, R. S. *Meteorological investigations of the upper atmosphere.* American Meteorological Society, 1968.

Ramaswamy, V., M.-L. Chanin, J. Angell, J. Barnett, D. Gaffen, M. Gelman, P. Keckhut, Y. Koshelkov, K. Labitzke, J.-J. R. Lin, A. O'Neill, J. Nash, W. Randel, R. Rood, K. Shine, M. Shiotani, and R. Swinbank. Stratospheric temperature trends: Observations and model simulations. *Rev. Geophys.*, 39(1):71–122, 2001a. ISSN 1944-9208.

Ramaswamy, V., M.-L. Chanin, J. Angell, J. Barnett, D. Gaffen, M. Gelman, P. Keckhut, Y. Koshelkov, K. Labitzke, J.-J. R. Lin, A. O'Neill, J. Nash, W. Randel, R. Rood, K. Shine, M. Shiotani, and R. Swinbank. Stratospheric temperature trends: Observations and model simulations. *Reviews of Geophysics*, 39(1):71–122, 2001b.

Randel, William, Petra Udelhofen, Eric Fleming, Marvin Geller, Mel Gelman, Kevin Hamilton, David Karoly, Dave Ortland, Steve Pawson, Richard Swinbank, Fei Wu, Mark Baldwin, Marie-Lise Chanin, Philippe Keckhut, Karin Labitzke, Ellis Remsberg, Adrian Simmons, and Dong Wu. The sparc intercomparison of middle-atmosphere climatologies. *J. Climate*, 17(5):986–1003, 2004.

Randel, William J., Keith P. Shine, John Austin, John Barnett, Chantal Claud, Nathan P. Gillett, Philippe Keckhut, Ulrike Langematz, Roger Lin, Craig Long, Carl Mears, Alvin Miller, John Nash, Dian J. Seidel, David W. J. Thompson, Fei Wu, and Shigeo Yoden. An update of observed stratospheric temperature trends. *J. Geophys. Res.-Atmos.*, 114(D2), 2009. ISSN 2156-2202. D02107.

Randel, William J., Anne K. Smith, Fei Wu, Cheng-Zhi Zou, and Haifeng Qian. Stratospheric temperature trends over 1979-2015 derived from combined ssu, mls, and saber satellite observations. *J. Climate*, 29(13):4843–4859, 2016.

Roble, R. G. and R. E. Dickinson. How will changes in carbon dioxide and methane modify the mean structure of the mesosphere and thermosphere. *J. Geophys. Res.*, 16:1441–1444, 1989.

Rodgers, C D. *Inverse Methods for Atmospheric Sounding: Theory and Practice*, volume 2. World Scientific, Hackensack, NJ, USA, 2011.

Russell, James M., Martin G. Mlynczak, Larry L. Gordley, Joseph J. Tansock, and Roy W. Esplin. Overview of the saber experiment and preliminary calibration results, 1999.

Schwartz, M. J., A. Lambert, G. L. Manney, W. G. Read, N. J. Livesey, L. Froidevaux, C. O. Ao, P. F. Bernath, C. D. Boone, R. E. Cofield, W. H. Daffer, B. J. Drouin, E. J. Fetzer, R. A. Fuller, R. F. Jarnot, J. H. Jiang, Y. B. Jiang, B. W. Knosp, K. Kruger, J.-L. F. Li, M. G. Mlynczak, S. Pawson, J. M. Russell, M. L. Santee, W. V. Snyder, P. C. Stek, R. P. Thurstans, A. M. Tompkins, P. A. Wagner, K. A. Walker, J. W. Waters, and D. L. Wu. Validation of the aura microwave limb sounder temperature and geopotential height measurements. *Journal of Geophysical Research: Atmospheres*, 113(D15), 2008.

She, C. Y., S. Chen, Z. Hu, J. Sherman, J. D. Vance, V. Vasoli, M. A. White, J. Yu, and D. A. Krueger. Eight-year climatology of nocturnal temperature and sodium density in the mesopause region (80 to 105 km) over Fort Collins (41N, 105W). *J. Geophys. Res.*, 27:3289–3292, 2000.

Sica, R J and A Haefele. Retrieval of temperature from a multiple-channel Rayleigh-scatter lidar using an optimal estimation method. *Appl. Optics*, 54(8):1872–1889, 2015.

Sica, R. J. and A. T. Russell. How many waves are in the gravity wave spectrum? *Geophysical Research Letters*, 26(24):3617–3620, 1999.

Sica, R. J., S. Sargoytchev, P. S. Argall, E. F. Borra, L. Girard, C. T. Sparrow, and S. Flatt. Lidar measurements taken with a large aperture liquid mirror. 1. Rayleigh scatter system . *Appl. Optics*, 34:6925–6936, 1995.

Sica, R. J., P. S. Argall, A. T. Russell, C. R. Bryant, and M. M. Mwangi. Dynamics and Composition Measurements in the Lower and Middle Atmosphere with the Purple Crow Lidar. *Recent Research Developments in Geophysical Research*, 3:1–16, 2000.

States, R. J. and C. S Gardner. Thermal structure of the mesopause region (80–105km) at 40 degrees N latitude. Part I: Seasonal variations. *J. Atmos. Sci.*, 57:66–77, 2000.

Stroud, W. G., W. Nordberg, W. R. Bandeen, F. L. Bartman, and P. Titus. Rocket-grenade measurements of temperatures and winds in the mesosphere over churchill, canada. *Journal of Geophysical Research*, 65(8):2307–2323, 1960.

Watts, P. D., R. Bennartz, and F. Fell. Retrieval of two-layer cloud properties from multispectral observations using optimal estimation. *Journal of Geophysical Research: Atmospheres*, 116(D16), 2011.

Yuan, T., C.-Y. She, D. A. Krueger, F. Sassi, R. Garcia, R. G. Roble, H.-L. Liu, and H. Schmidt. Climatology of mesopause region temperature, zonal wind, and meridional wind over Fort Collins, Colorado (41N, 105W), and comparison with model simulations. *J. Geophys. Res.*, 113, 2008.

Chapter 2

Calculation and Validation of Optimal Estimation Method Temperature Retrievals Using Purple Crow Lidar Rayleigh-scatter Measurements[1]

2.1 Introduction

Ramaswamy et al. (2001) and Randel et al. (2004, 2009, 2016) discussed the effects of the middle atmosphere temperature trend over time using different instruments. The MLT region is too high for weather balloons to measure the temperature and the resolution of satellite measurements is on the order of 2 km or greater in this region. One of the best instruments for high-spatial and time-resolution temperature measurements is lidar. Rayleigh-scatter lidars are the best choice for temperature measurements in the stratosphere and lower mesosphere, while resonance lidars are best in the upper mesosphere and lower thermosphere. In order to retrieve temperature, it is necessary to have a seed, or tie-on, pressure at the highest point of the measurement profiles, which is usually taken from a model. This assumption causes a systematic uncertainty in the retrieved temperature profiles. Rayleigh lidars measure relative

---

[1]Jalali, A., & Sica, R. J., & Haefele, A., Atmospheric Measurement Technique, 2018, 11, 11, 10.5194/amt-11-6043-2018.

density; by assuming hydrostatic equilibrium between layers and applying the ideal gas law, a temperature profile can be calculated from the relative density measurement. Resonance lidars measure the height-dependent kinetic temperature in the upper mesosphere and lower thermosphere. Sodium lidars use the resonant scattering of the transmitted laser pulse from the sodium layer (83 to 105 km); here temperature accuracy is limited by our knowledge of the received photon noise and transmitted wavelength and line width (Bills et al., 1991; Krueger et al., 2015).

Randel et al. (2004) used several sets of measurements including lidars to calculate a temperature climatology between 10 and 80 km primarily using lidar measurements taken in the 1990s. They did a comprehensive comparison between various data sources and found good agreement between the lidar and satellites up to 64 km (0.1 mb). They also found that there is an underestimation of temperature variability in the tropical upper stratosphere in analysis data and large variability in the stratopause temperature for the different datasets. In the upper mesosphere and lower thermosphere, Rayleigh lidar temperature climatologies have been blended with sodium lidar temperature measurements to extend these climatologies in altitude (Leblanc et al., 1998), and compared against sodium lidar temperatures such as those given by She et al. (2000), States and Gardner (2000a) and Yuan et al. (2008). Hauchecorne et al. (1991), Leblanc et al. (1998), She et al. (2000), States and Gardner (2000a), Argall and Sica (2007) and Yuan et al. (2008) found significant temperature differences between the climatologies and atmospheric models, in particular between 80 km and above. The lidar measurements showed that the mesopause altitude was lower in the summer than in the winter while the empirical models did not predict the observed seasonal behavior, showing little difference in altitude.

Diurnal and nighttime temperature climatologies were published by States and Gardner (2000a) from Urbana, Illinois (40° N, 88° W) (URB) using measurements between 1996 and 1998. She et al. (2000) used 8 years of nighttime measurements from Colorado State University (CSU) sodium lidar (41° N, 105.1° W) from 1990 to 1999 to calculate a temperature climatology. The CSU lidar was upgraded in 1999 from a one-beam to a two-beam lidar to be able to probe the mesopause during daytime and nighttime (Arnold and She, 2003). Yuan et al. (2008) published the results of the upgraded CSU lidar, giving climatologies for

nighttime and daytime between 2002 and 2006. The URB and CSU climatologies are among the best datasets for the validation of upper-mesosphere and lower-thermosphere temperatures, plus they allow for a direct comparison between our new climatology and Argall and Sica (2007). Yuan et al. (2008) provide additional years of overlap with our new climatology for the validation of our OEM-derived temperatures.

We have created a new climatology with measurements from The University of Western Ontario's Purple Crow Lidar (PCL) using the optimal estimation method (OEM) with a full uncertainty budget that goes higher in altitude than the climatology using the method of Hauchecorne and Chanin (henceforth the HC climatology), in addition to including systematic and random uncertainties. We then compare the OEM-derived climatology with sodium lidar climatologies to validate the Rayleigh-scatter temperatures. Section 2 summarizes the Rayleigh temperature retrieval methods, including the HC method and the OEM, as well as the procedure for generating the climatology. Section 3 compares the OEM results with the HC results. Section 4 presents the comparison between the PCL temperature OEM climatology with other sodium lidar climatologies. Section 5 is a summary and Section 6 is the conclusion.

2.2 Procedure for Generating the Climatology

This study uses 519 nightly averaged temperature profiles from 1994 to 2013 distributed in time as shown in Tables 2.1 and 2.2. The distribution histogram of number of nights are brought in Fig. 2.1.

2.2.1 Methodology to Calculate Temperature Climatology

OEM methodology

The OEM uses the forward model and non-paralyzable dead time correction equation (Sica and Haefele, 2015) (henceforth SH2015) to retrieve the nightly average temperature profiles from the LLR and HLR channels simultaneously. In SH2015 the dead time, background, and temperature were retrieved. They considered the lidar constant as a forward model

Table 2.1: Number of nightly mean profiles used to calculate the PCL temperature climatology by month between 1994 and 2013.

Month	Number of profiles
January	9
February	14
March	17
April	19
May	63
June	72
July	109
August	99
September	39
October	37
November	26
December	15
Total	519

parameter, but in this study, the lidar constants for LLR and HLR channels were retrieved rather than specified . The OEM uses an estimation of the covariances of the measurements, retrieval, and forward model parameters. The model parameter covariance matrices used in this study are based on SH2015, in which the summary of the values and related uncertainties of the measurements and the retrieval and forward model parameters are presented in Table 2.3. The data grid is $264\,\mathrm{m}$, and the retrieval grid is $1056\,\mathrm{m}$. Due to the PCL measurements between 1994 and 1998 having only the HLR channel measurements, temperature and background were retrieved but not dead time. Instead, the systematic uncertainty due to the saturation was calculated. The PCL measurements from 1999 to 2011 used the LLR digital channel to get more temperature information and the dead time of the HLR channel was retrieved using an *a priori* value of $10\,\mathrm{ns}$ (Table 2.3). The LLR dead time was treated as a model parameter and a standard deviation of 5.7% was considered.The CIRA-86 model atmosphere was chosen as the temperature *a priori* with a variance of $(35\,\mathrm{K})^2$ at all altitudes

Table 2.2: Number of profiles used to calculate the PCL temperature climatology per year between 1994 and 2013.

Year	Number of profiles
1994	36
1995	40
1996	22
1997	17
1998	78
1999	57
2000	43
2001	2
2002	57
2003	34
2004	5
2005	37
2006	32
2007	34
2012	20
2013	5
Total	519

(Fleming et al., 1988).

HC methodology

The climatology was formed using the methodology of Argall and Sica (2007) (henceforth AS2007), who used the HC method as follows. First, the quality of each 1 min scan profile of measurements was checked. Then, nightly averaged temperature profiles were calculated. The quality of the nightly averaged measurements was assessed based on the measurement signal-to-noise ratio. Measurements were accepted if the signal-to-noise ratio was greater than 2 at the highest altitude for the initialization of downward integration. AS2007 used
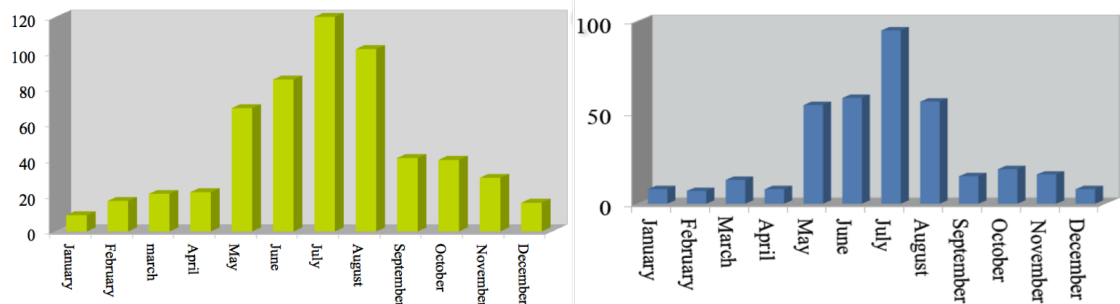
Figure 2.1: Histogram distribution of number of nights of PCL measurements for HLR channel (left) and LLR channel (right).

Table 2.3: Values and associated uncertainties of the measurements and the *a priori*, retrieval and forward model parameters

Parameter	Value	Standard deviation
Measurement		
HLR (1994-2013)	Measured	Poisson statistics
LLR (1999-2013)	Measured	Poisson statistics
Retrieval parameters (a priori)		
Temperature profile	taken from CIRA-86	35 K
Background for LLR	Average of photocounts above 90 km	SD above 90 km
Background for HLR	Average of photocounts above 115 km	SD above 115 km
Dead time for LLR and HLR (1999-2011)	10 ns	5.7 and 11.19%, respectively
Dead time for HLR (2012-2013)	4 ns	0.5%
Lidar constant for HLR	Estimated using forward model (55-60 km)	10%
Lidar constant for LLR	Estimated using forward model (45-50 km)	10%
Forward model parameters		
Pressure profile	Fleming et al. (1988)	5%
Ozone density	McPeters et al. (2007)	4%
Ozone cross section	Griggs (1968)	2%
Acceleration due to gravity	Mulaire (2000)	0.001%
Rayleigh-scattering cross section	Nicolet (1984)	0.2%
Air number density	CIRA-86	5%

the nightly averaged measurements with a minimum signal-to-noise ratio of 2 at the initial height of integration of 95 km; however, this height was reduced to 90 km in this study because the decrease in the initial height of integration led to having more nights, which allowed for a better comparison with the OEM climatology. The raw photon count profiles

have been co-added to produce height bins of 1008 m and a "3's and 5's" filter (Hamming, 1989) was applied to the calculated temperature profiles to smooth them in the climatology. A 3's and 5's filter is a filter made by convolution of 3 point and 5 point running means, resulting in a filter with coefficients given by

$$\frac{1}{15}[1 \quad 2 \quad 3 \quad 3 \quad 3 \quad 2 \quad 1]$$

and side lobes 20 dB lower than either a 3 or 5 point filter (Hamming, 1989). The co-added height value of 240 m was chosen as a data grid for the OEM to be consistent with the vertical resolution of the HC. The vertical resolution definition and calculation are based on Leblanc et al. (2016a).

The following steps were taken to make a composite year temperature climatology after calculating all lidar temperature profiles. Only the profiles were used that, after removing the top 10 km, extended up to 80 km. Each temperature profile was then interpolated to an altitude grid with 1 km intervals between 35 and 110 km. For dates with multiple measurements over the years (e.g. 25 July 1994, 2003, and 2003), a weighted-average profile was calculated using each profile's statistical uncertainty as weights. Then, linear interpolation was used to fill the gaps where no measurements existed and a 33-day triangular filter was applied to smooth the composite temperature climatology.

2.2.2 Effect of *a priori* on the retrieval temperature profiles in the OEM

A retrieved temperature profile using the CIRA and the US Standard Atmosphere as the *a priori* for a sample PCL night (24 May 2012) was plotted in order to demonstrate the contribution of the *a priori* temperature profiles in the retrieval results and the temperature difference between the *a priori* temperature profiles (Fig. 2.2). The temperature difference between the *a priori* profiles is shown in Fig. 2.2a. The temperature difference around 94 km, which is below the OEM cutoff heights, is about 20 K. In Fig. 2.2b, the red profile is the temperature difference due to the *a priori* and the blue profile is the statistical uncertainty calculated by the OEM. The 0.9 and 0.8 value lines in the **Au** are the cut-off heights for the OEM and are shown with solid and dashed lines, respectively. It can be seen that the choice
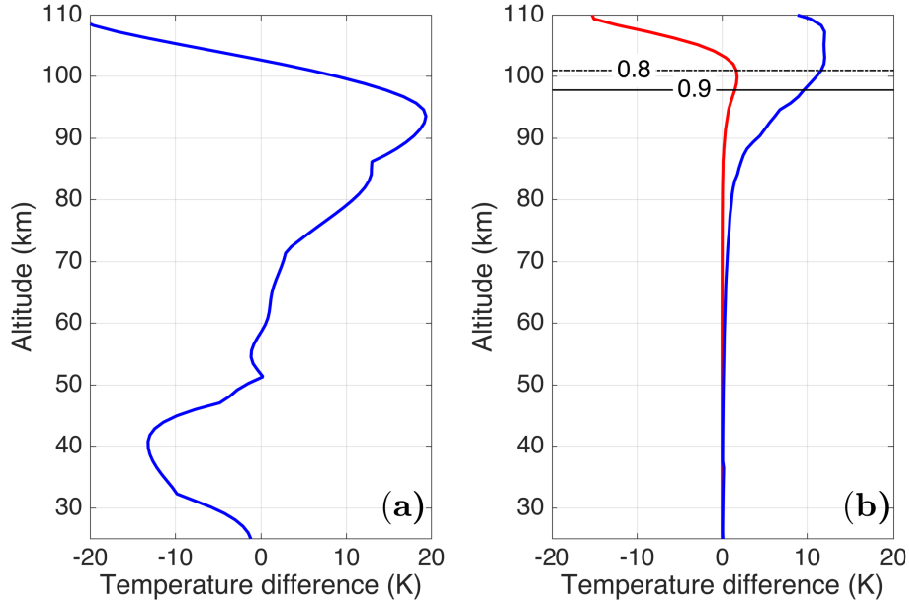
Figure 2.2: a) Temperature difference between the *a priori* temperature profiles, US Standard Atmosphere and CIRA-86 (blue line). b) Temperature difference between the OEM retrieved temperature profiles using the *a priori* profile used in Fig 2.2a, for 24 May 2012 (red line) and the calculated OEM statistical uncertainty (blue line). The solid black and solid-dashed black lines are the height below which the temperature profile is more than 90% (0.9) and 80% (0.8) due to the measurements, respectively.

of *a priori* has little effect (1.5 K below the 0.9 line and less than 2 K below the 0.8 line) on the retrieved temperature and that the difference between the retrieved temperatures from each choice is much less than the statistical uncertainty (10 K below the 0.9 line and 12 K below the 0.8 line) at the top of the profiles.

2.3   Results

The percentage of nights at each altitude for the HC method and OEM for 0.9 and 0.8 cutoff height are given in Fig. 2.3. It can be seen that the OEM cutoff height is much higher than the HC method cutoff height for all 519 nights.

To create the temperature climatology, we used the nightly OEM temperature profiles to calculate an average temperature profile for each day of the year (Fig. 2.4). The 0.9 and

54
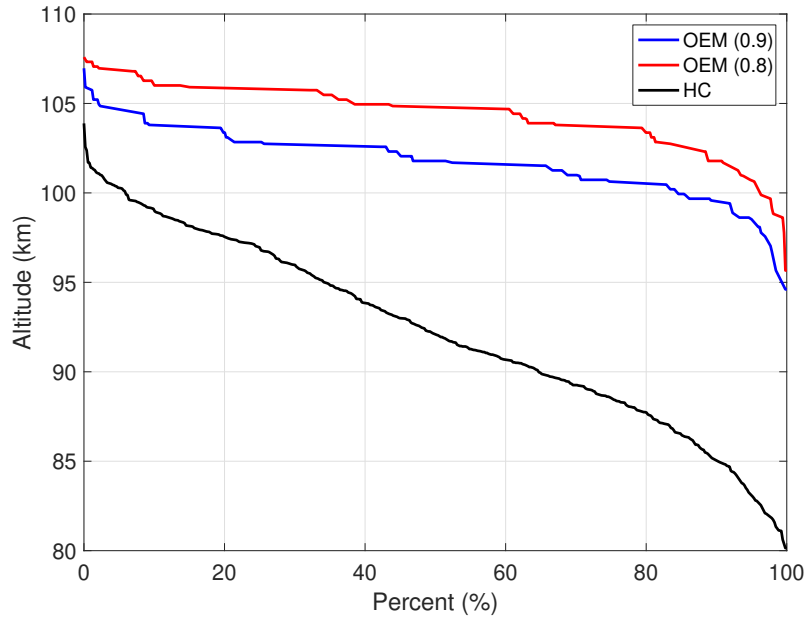
Figure 2.3: The percentage of number of nights at each altitude for the HC method and OEM for 0.9 and 0.8 cutoff height.

0.8 values of **Au** are superimposed in Fig. 2.4 with white lines. To estimate the annual temperature variability, the temperature difference between PCL temperature climatology using the OEM and the calculated climatology from monthly CIRA-86 temperature profiles is plotted in Fig. 2.5 for each month. There is a temperature difference on the order of $5\,\mathrm{K}$ below $52\,\mathrm{km}$. There is a bias smaller than $3\,\mathrm{K}$ between the CIRA profiles and the PCL monthly mean temperatures between 55 and $65\,\mathrm{km}$ except in the winter. Above $65\,\mathrm{km}$ the CIRA is warmer, on average around $8\,\mathrm{K}$, than the PCL up to $90\,\mathrm{km}$, but much colder (on the order of $20\,\mathrm{K}$) above $90\,\mathrm{km}$. CIRA temperature profiles have a smaller difference (less than $10\,\mathrm{K}$) compared to the PCL in summertime rather than wintertime up to around $90\,\mathrm{km}$.

The geophysical variability for the OEM PCL temperature climatology (Fig. 2.6) was calculated based on the difference between the 33-day temperature standard deviation and the variability of the PCL measurements. The geophysical variability shows the wave activity in the time range of 2 to 33 days, encompassing the scale range of planetary waves. We followed the procedure from AS2007 based on Leblanc et al. (1998) to calculate the geophysical variability. Figure 2.6 shows the temperature variability related to waves from 2 to 33 days.
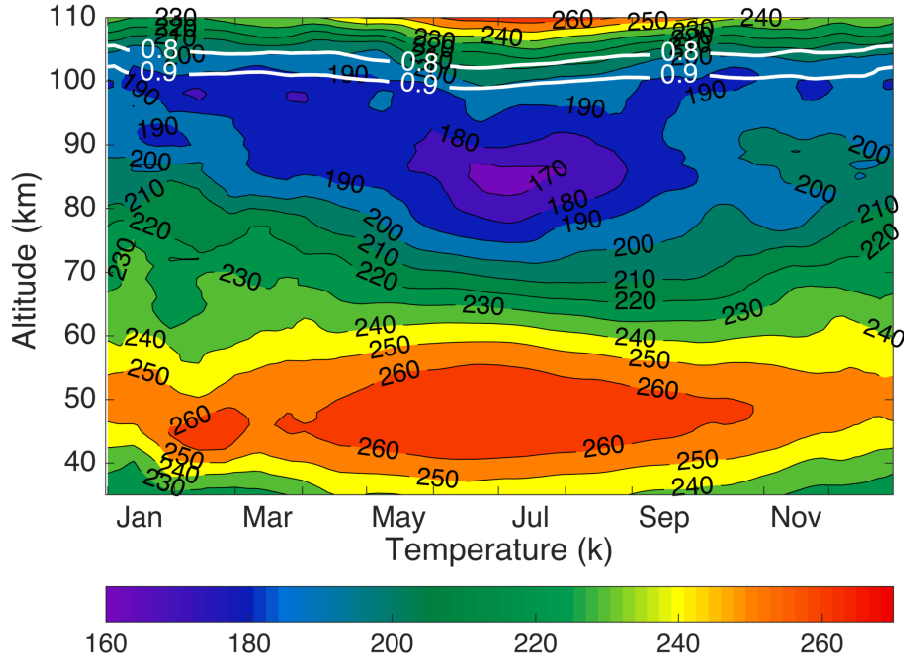
Figure 2.4: Composite PCL Rayleigh temperature climatology using the OEM. The white lines are the height below which the temperature climatology is more than 90% (0.9) and 80% (0.8) due to the measurements.

The temperature variability from mid-April to the end of September below 70 km is less than 4 K. However, in the same period of time the highest temperature change is between 80 and 90 km due to the wave activity in the mesosphere. There is a peak at 41 km in January which may be related to sudden stratospheric warmings during winter. However, the lower number of measurements in January will also contribute to the variability, and determining the extent of each contribution is not possible (AS2007). The temperature variability due to mesospheric inversion layers reaches a maximum between 62 and 72 km during December and January. These results are in good agreement with the results presented in Figure 6 of AS2007.

2.3.1 Uncertainty budget and vertical resolution

The lidar measurements include both systematic and random uncertainty. Systematic uncertainties originate in the forward model from uncertainties due to model parameters. One of the advantages of the OEM is that it provides systematic uncertainties for all retrieved
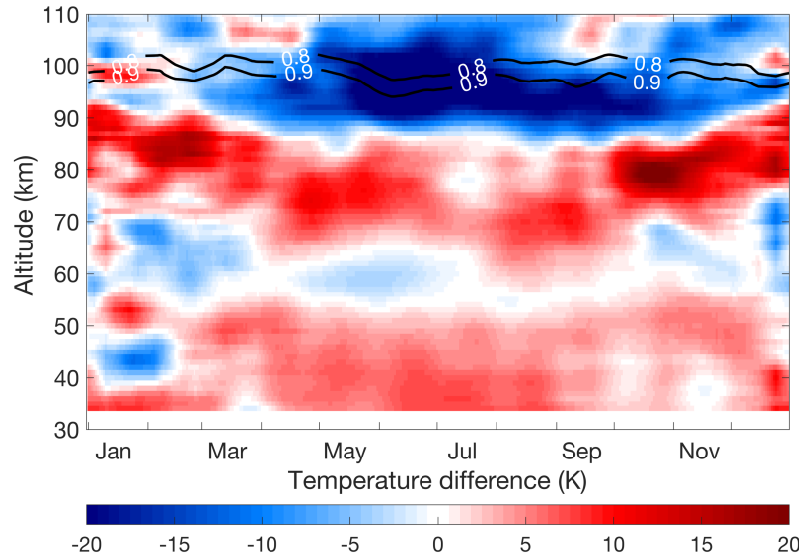
Figure 2.5: Temperature difference between the calculated climatology from monthly CIRA-86 temperature profiles and the OEM PCL temperature climatology. The black lines are the height below which the temperature climatology is more than 90% (0.9) and 80% (0.8) due to the measurements.

parameters, as well as the random uncertainties. The systematic uncertainties calculated in the PCL OEM technique (Table 2.3) are based on the following model parameters:

1. knowledge of the HLR dead time (1994-1998 only);

2. determination of the Rayleigh-scatter cross section for air;

3. Rayleigh cross section variation with composition in the mesosphere and thermosphere;

4. air number density influence effect on Rayleigh extinction;

5. ozone absorption cross section;

6. ozone concentration effect on transmission;

7. seed (tie-on) pressure;

8. acceleration due to gravity; and
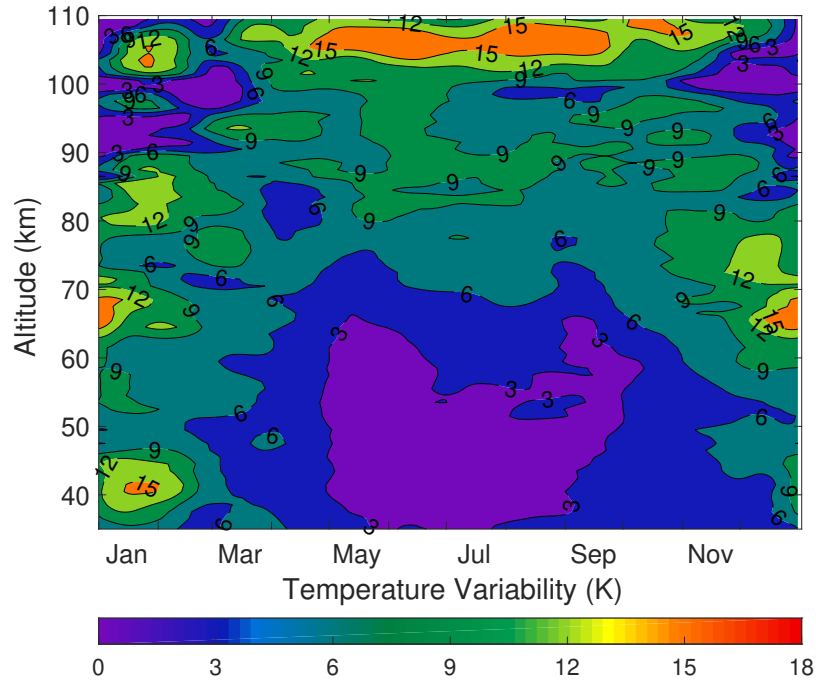
Figure 2.6: Geophysical variability in temperature for the OEM PCL climatology.

9. mean molecular mass variations with height above 80 km.

Uncertainty budget for the PCL climatology

A typical case for the temperature statistical and systematic uncertainties for a nightly average retrieval is shown in Fig. 2.7. The temperature uncertainty due to the seed pressure has the highest contribution among all of the systematic uncertainties at the altitudes above the mesopause. However, temperature uncertainties related to ozone, including the ozone absorption cross section, have the largest effect below 40 km. The uncertainty contribution for the gravity model is almost constant with height and is on the order of 0.002 K.

The nightly OEM statistical uncertainty profiles were used to form the statistical temperature uncertainty of the PCL temperature climatology (Fig. 2.8) using the procedure described in AS2007. The statistical uncertainty below 75 km is less than 1 K and gradually increases with height until it reaches 0.9 **Au** where it is less than 10 K. The monthly average minimum, maximum and median of temperature uncertainties related to the systematic
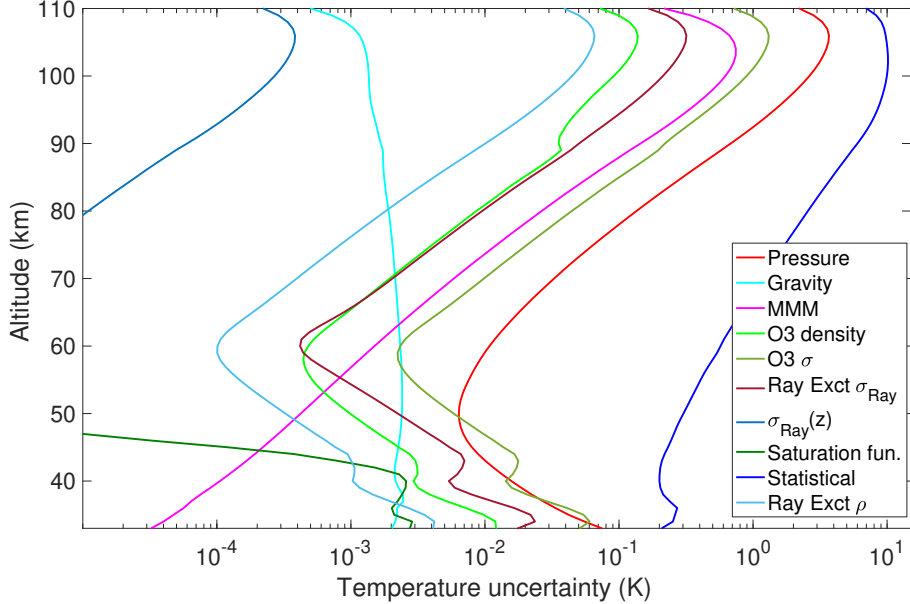
Figure 2.7: A typical night's systematic and random uncertainties for the OEM temperature retrieval. Here the uncertainty due to the pressure is coming from the seed pressure uncertainty.

uncertainties for all months are plotted in Fig. 2.9.

The OEM directly gives the vertical resolution of the retrieval at each height from the averaging kernels (Fig. 2.10) and does not employ an digital filtering of the measurements or retrieved quantities. The vertical resolution is 1056 m below 95 km and is equal to the retrieval grid. It is 3000 m below the 0.9 cutoff height; however, it increases rapidly to 5000 m around the 0.8 cutoff line. Leblanc et al. (2016b) recommended two standardized definitions for a temperature profile vertical resolution. In order to compare the retrieved temperature profiles using the OEM and the HC method, the two vertical resolution definitions given by Leblanc et al. (2016b) were used to find the best bin size for the HC method so it would have an identical vertical resolution to the OEM retrieval. We found that 264 m co-added bins and a "3's and 5's" filter gave a vertical resolution of 1008 m, close to the OEM temperature retrieval grid (1056 m).

Comparison with uncertainty budget of the traditional method

Leblanc et al. (2016b), hereafter NDACC2016, used a Monte Carlo method to calculate the
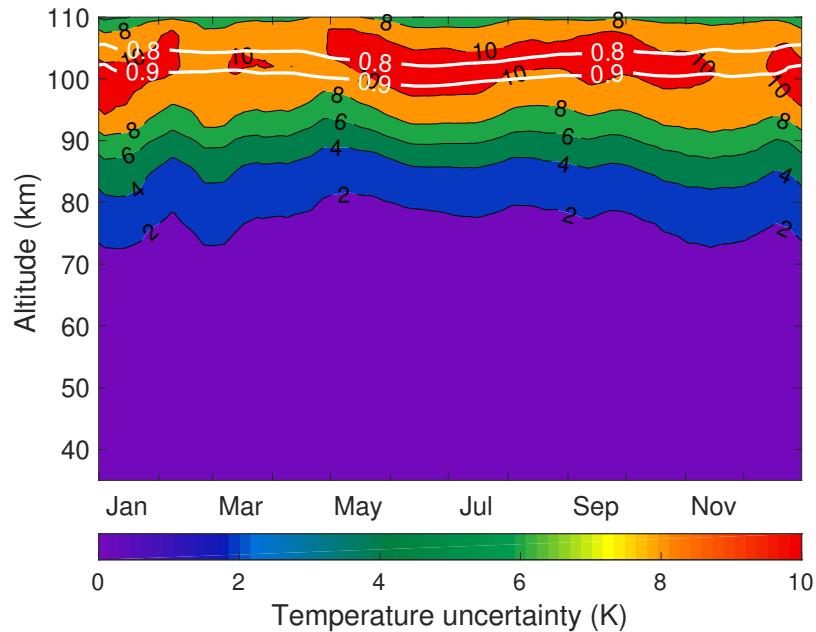
Figure 2.8: Statistical temperature uncertainty of the temperature climatology. The white lines are the height below which the temperature climatology is more than 90% (0.9) and 80% (0.8) due to the measurements.

statistical and systematic uncertainties for the temperature retrieval. We have compared our results with his ND:YAG 532 nm lidar results. NDACC2016 and our climatology give the temperature uncertainties for several of the same parameters (Table 2.3), including the statistical uncertainty (detection noise), the Rayleigh cross section, air number density, ozone absorption cross section, ozone number density, and the gravity model. NDACC2016 calculated the temperature uncertainty due to each parameter per 1% uncertainty. In order to compare NDACC2016 results with the PCL uncertainties using the OEM, we need to scale NDACC2016 simulations to the PCL as recommended by Leblanc et al. (2016b). For example, if the temperature uncertainty due to air number density is per 1% uncertainty in NDACC2016, then we must multiply NDACC2016 uncertainties by a factor of 5 because we assume an air number density uncertainty of 5% (recommended by NDACC2016) in the PCL forward model (Table 2.3). We have compared our results with the statistical and systematic uncertainties presented in Figures 1 to 9 in NDACC2016 for the case of a 532 nm laser beam with a 1 MHz count rate at 45 km, a height resolution of 300 m, and an integration time of
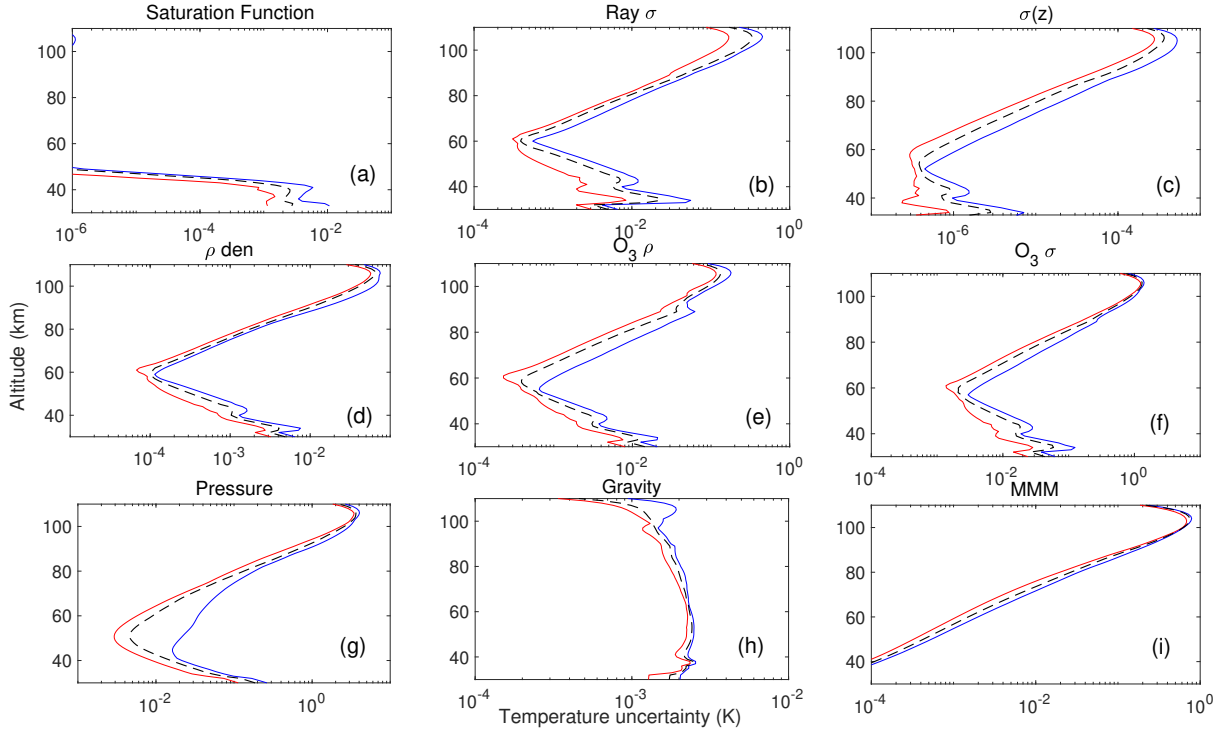
Figure 2.9: PCL temperature systematic uncertainty due to the (a) saturation function (1994 to 1998 only), (b) Rayleigh extinction cross section, (c) Rayleigh cross section variation with height, (d) air density affect on Rayleigh extinction, (e) ozone absorption cross section (f) ozone concentration, (g) seed (tie-on) pressure, (h) gravity model, and (i) mean molecular mass variation with height. In each figure, red, blue, and black lines are the minimum, maximum, and median between all months, respectively.

2 hours (Fig. 2.11).

The statistical uncertainty comparison between the PCL and NDACC2016 is shown in dark blue in Fig. 2.11. It can be seen that the NDACC2016 statistical uncertainty almost equals the scaled PCL statistical uncertainty above the stratopause. However, there is a difference at altitudes below 50 km. The statistical uncertainty difference in the lower altitudes is due to using the two Rayleigh channel measurements (HLR and LLR) to calculate the temperature in the lower altitudes. The uncertainties at these altitudes are then a combination of the LLR and HLR uncertainties.

The temperature uncertainty due to the uncertainty in the Rayleigh cross section in NDACC2016 for each 1% at two sample altitudes, 30 and 38 km, is on the order of 0.001 K
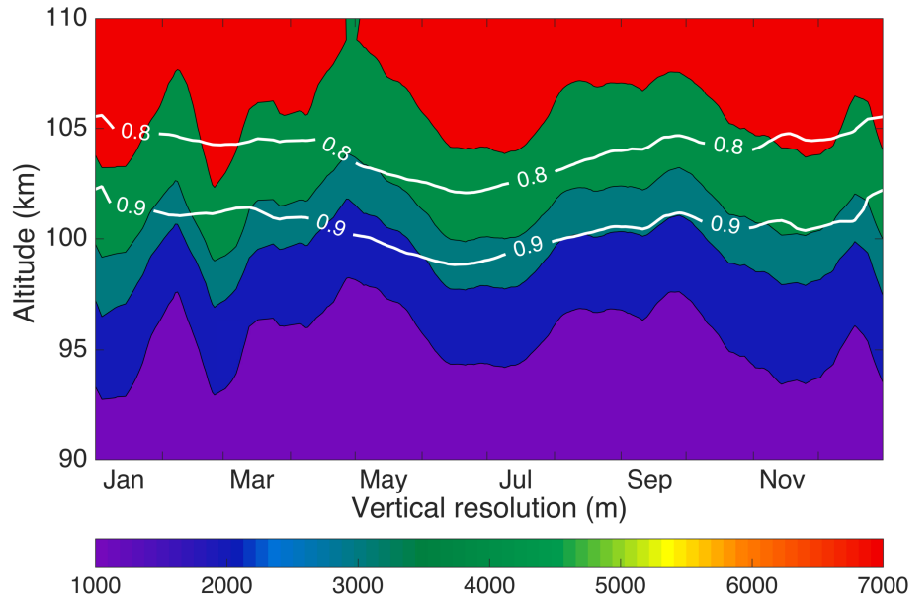
Figure 2.10: The OEM vertical resolution. The vertical resolution below 80 km is 1056 m; that is, it is equal to the retrieval grid spacing (not shown). The white lines are the height below which the temperature climatology is more than 90% (0.9) and 80% (0.8) due to the measurements.

(NDACC2016, Figure 4). The temperature uncertainty due to the Rayleigh cross section in the OEM is presented per 0.2%; therefore, the scaled cross section uncertainty for NDACC2016 is 1 order of magnitude smaller than the PCL Rayleigh cross section uncertainty. However, this temperature uncertainty is very small.

The uncertainty due to air number density as an input quantity per 1% is shown in NDACC2016 (their Figure 5 left panel). The NDACC2016 scaled temperature uncertainty due to air number density is of the same order of magnitude as the OEM-derived uncertainty for the PCL (Fig. 2.11).

The standard deviation for the ozone cross section in the OEM forward model is 2%. Therefore, the NDACC2016 ozone cross section temperature uncertainties should be doubled to compare them with the PCL. The temperature uncertainty due to the ozone cross section uncertainty in NDACC2016 (their Figure 6 left) after scaling is about 4 times smaller. The other temperature uncertainty due to ozone is the ozone number density. The temperature uncertainty due to ozone number density uncertainty for the NDACC (their Figure 7 left),
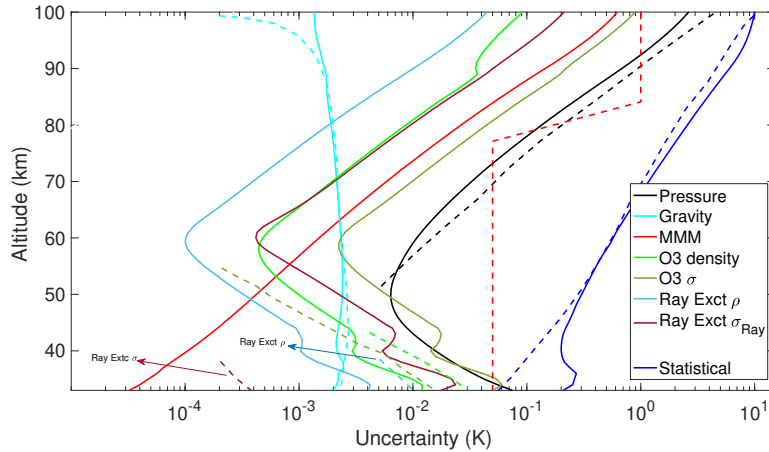
Figure 2.11: Comparison of the PCL statistical and systematic uncertainties with scaled uncertainties from Leblanc et al. (2016b) as described in the text. The solid lines are the uncertainties due to the PCL and the dashed lines are uncertainties due to NDACC2016.

after scaling by a factor of 0.25 (as the PCL *a priori* assumes 4% uncertainty), is almost twice that of the PCL's. The uncertainties due to ozone number density are so small above 45 km that they have not been listed in the total uncertainty budget in NDACC2016's final results.

The temperature uncertainty due to the choice of pressure at the highest altitude (seed pressure) is called the tie-on uncertainty in NDACC2016. The tie-on uncertainties are in the same range and the small differences between the PCL and NDACC2016 (their Figure 8) are related to the fact that the seed pressure altitude is at 99 km for NDACC2016 and at 110 km for the PCL.

The gravity temperature uncertainties for both NDACC2016 and the scaled PCL are consistent and are roughly 0.002 K. NDACC2016 states that the temperature uncertainty due to the molecular mass is negligible below 85 km and is on the order of 0.05 K and above 85 km can increase up to 1 K (NDACC2016, Table 3). The OEM shows that the PCL molecular mass temperature uncertainty at 85 km is 0.06 K. The PCL molecular mass temperature uncertainties from 90 to 100 km are between 0.1 and 0.6 K. However, the semi-empirical mean molecular mass variation of the US Standard model is considerably different from the variation assumed by NDACC2016, accounting for the differences in the calculated

uncertainties.

2.4 Comparison of the OEM climatology with other climatologies

In order to evaluate the OEM results, the new OEM PCL temperature climatology was compared with the existing PCL temperature climatology using the HC method, as well as other climatologies including sodium lidar climatologies.

2.4.1 Comparison between the PCL climatology using the OEM and HC methods

AS2007 used PCL measurements between 1994 and 2004 to calculate a PCL temperature climatology (henceforth, 2004 PCL climatology) using the HC method. The top $10\,\mathrm{km}$ of all temperature profiles was removed from the 2004 PCL climatology in order to reduce the effect of seed pressure and the same procedure was followed in the HC calculations for the updated PCL climatology (between 1994 and 2013). The temperature differences between the OEM and updated HC PCL temperature climatologies are shown in Fig. 2.12. The white space in the upper part of Fig. 2.12 is due to removing $10\,\mathrm{km}$ from the top of each profile for the updated HC PCL climatology. In addition, the lines corresponding to the 10 and $15\,\mathrm{km}$ cutoff for the HC method and the 0.9 cutoff line for the OEM are superimposed onto Fig. 2.12.

The OEM temperature climatology is $0.55 \pm 0.23\,\mathrm{K}$ warmer than the updated HC climatology average from 40 to $60\,\mathrm{km}$. Although the difference is within the statistical uncertainty of the measurements (Fig. 2.7), there is a warm bias. The bias due to differences in ozone profile between the two climatologies is only $+0.05$ K. The OEM used measurements from two Rayleigh channels (HLR and LLR) after 1999 to calculate the OEM climatology while only the HLR channel measurements were used for the HC method and the OEM before 1999. The effective LLR signal is up to about $60\,\mathrm{km}$ of altitude. The temperature difference in the bottom range (between 40 and $60\,\mathrm{km}$) of measurements is because of using a

two-channel retrieval in the OEM and comparing it with a one-channel (HLR) retrieval in the HC method. The two channel OEM method retrieves the dead time for each profile, while the dead time in the HC method was an empirically determined constant based on count measurements using a pulsed LED source. In order to compare the OEM with HC temperature climatology, we could have merged the calculated LLR and HLR temperature profiles in the HC method. However, the temperature uncertainty induced by the merging will be more than the ± 0.05 K temperature difference between the OEM and HC climatology (Jalali, 2014).

The OEM temperature above 80 km up to the 10 and 15 km cutoffs is colder than the temperatures obtained using the HC method. The temperature differences above 80 km are mostly due to the sensitivity of the model seed pressure in the HC method. Figure 2.12 shows that the OEM temperature climatology reaches 5 to 10 km higher in altitude than the HC temperature climatology. The differences between the OEM and HLR are not calculated below 40 km due to the lack of HLR data in some time periods.

Finally, in order to evaluate the effect of the *a priori* on the temperature differences, the same temperature climatologies were calculated using the OEM with the US Standard model as the *a priori* temperature profile and the same differences as discussed above were obtained, again demonstrating that the results show little sensitivity to the choice of any reasonable *a priori* profile.

The HC method usually uses a seed pressure value at the highest point of the profile. However, the seed pressure can be substituted by temperature and density and is called the seed temperature (Gardner et al. (1989), equation 86). When a seed temperature is used, the temperature is obtained from the CIRA-86 model, and the measured relative density profile is normalized (typically by a model) to obtain a seed pressure to use in the HC retrieval. The temperature differences between the OEM climatology and the updated HC climatology using the seed temperature (instead of seed pressure) are shown in Fig. 2.13. Comparing Figs. 2.12 and 2.13 reveals that the temperature difference above 80 km between the OEM and the updated HC using seed temperatures is larger than the differences between the OEM and the updated HC using seed pressures. However, the differences below 80 km are identical and the small temperature differences between the OEM and HC method are due
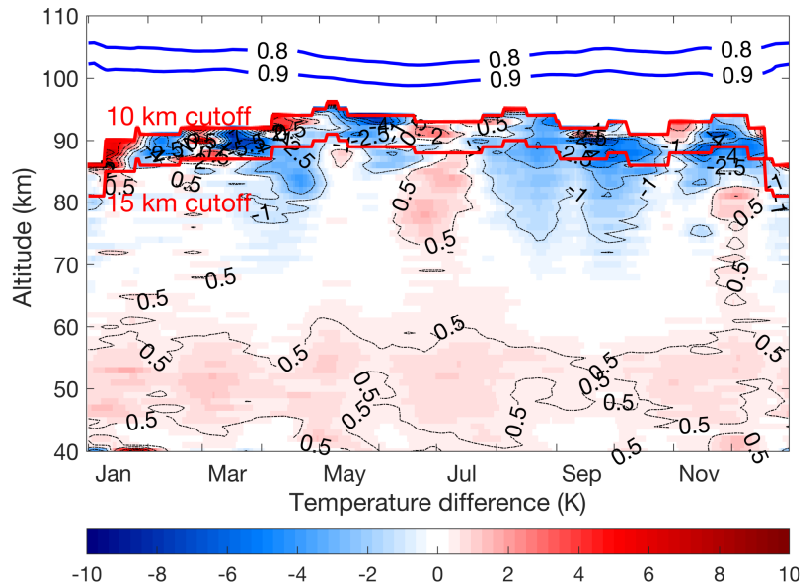
Figure 2.12: PCL temperature climatology difference between the OEM and HC method (OEM-HC) using seed pressure. The blue lines show the height below which the OEM temperature climatology is more than 90% (0.9) and 80% (0.8) due to the measurements. The red lines are the 10 and 15 km cutoff height for the HC method.

to the tie-on temperature or pressure value. The difference between the HC climatologies calculated by these two methods highlights the sensitivity to seed pressure at the greatest heights in this method.

Gerding et al. (2008) used coincident Rayleigh and sodium resonance lidar temperature measurements to minimize the seed pressure. For altitudes below the sodium layer, Rayleigh lidar measurements are used to determine the temperature. While having this combination of a Rayleigh and resonance temperature lidar is ideal, most Rayleigh temperature lidar systems are not colocated with a resonance temperature lidar, and hence the effect of seed pressure is the largest systematic uncertainty at the upper range of the temperature profile determined.
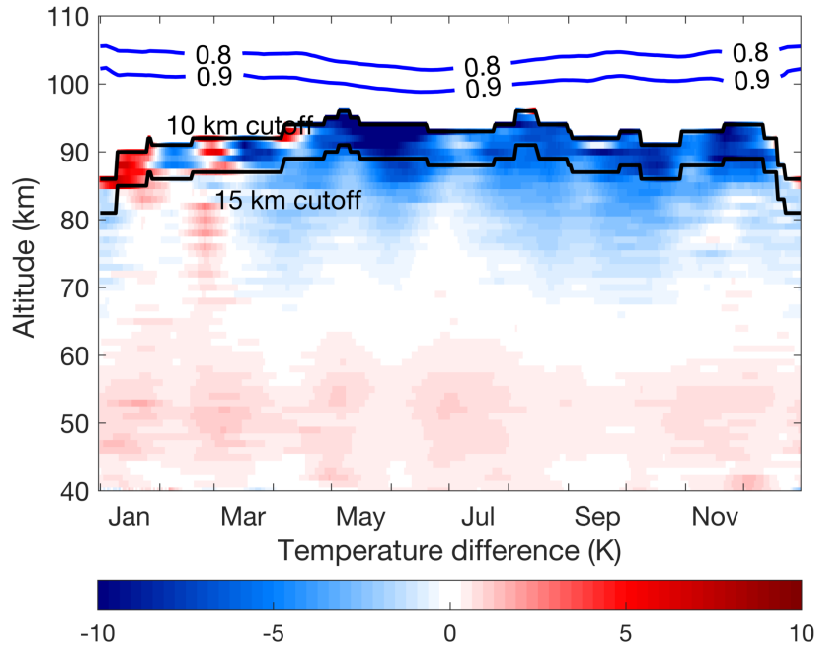
Figure 2.13: PCL temperature climatology difference using the OEM and HC method (OEM-HC) using seed temperature. The blue lines show the height below which the OEM temperature climatology is more than 90% (0.9) and 80% (0.8) due to the measurements. The black lines are the 10 and 15 km cutoff height for the HC method.

2.4.2 Comparison with sodium lidar climatologies

The comparison between the PCL Rayleigh temperature climatology using the HC method with sodium lidars was done by AS2007. Their results showed that the average temperature between 83 and 95 km measured by the PCL was between 7 and 7.4 K colder than CSU and URB climatologies, respectively. Using the OEM to extend the PCL Rayleigh lidar temperature climatology to above 100 km provides the opportunity to validate the PCL results against sodium lidar climatologies, which have their highest signal-to-noise ratio in a few kilometer-wide regions between about 90 and 95 km of altitude, and obtain sufficient high-quality measurements to calculate climatologies from 85 to 105 km. Sodium lidars directly measure the kinetic temperature without assuming hydrostatic equilibrium or requiring the knowledge of mean molecular mass and molecular cross section variations with height and

can be configured to obtain temperatures during both the day and night. She et al. (2000), Yuan et al. (2008), and States and Gardner (2000a) have published sodium temperature lidar climatologies in the same latitude range as PCL. Both sites are west of the PCL, but in the case of URB the separation in longitude is less than 8°. The URB and CSU climatologies are among the best datasets for validation of upper-mesosphere and lower-thermosphere temperatures, plus they allow for a direct comparison between our new climatology and AS2007. The upgraded CSU (Yuan et al., 2008) provides additional years of overlap with our new climatology for validation of our OEM-derived temperatures. The nighttime URB and upgraded CSU temperature climatologies were compared with the PCL temperature climatology.

The PCL temperature climatology differences using the OEM compared with the sodium lidars are presented in Figures 2.14, 2.15 and 2.16. The absolute value of the average differences in 5 km height bins between the sodium lidar temperature climatologies and the PCL climatology using the OEM and the HC method are given in Table 2.4. The absolute value is used to avoid differences canceling each other. The bottom part of the table is important, as it gives the differences between the sodium lidars themselves. The differences between the sodium lidars are taken as the level of difference defining the agreement between the PCL lidar and the sodium systems. The PCL HC climatology in general does not agree with the sodium lidar climatologies to the same extent to which they agree with each other, while the PCL OEM climatology typically does agree with the sodium lidar climatologies to the level at which they agree with each other. The temperature differences between the PCL OEM and sodium lidar climatologies for the entire range of altitudes (80 to 105 km) are smaller than the temperature difference between the PCL HC climatology and the sodium lidar climatologies in the range of 80 to 95 km for which PCL HC temperatures are available. There is a temperature difference at the winter mesopause between the PCL climatology and CSU climatology, but this difference has decreased in the upgraded nighttime CSU climatology compared to that determined by AS2007. The large temperature differences between the PCL (OEM) and URB temperature climatology during summertime below 85 km existed in AS2007 and may be in part due to the signal-to-noise ratio of the sodium lidar measurements rapidly decreasing below 85 km.

Table 2.4: Absolute value of the average PCL temperature differences with sodium lidars and the temperature difference between sodium lidars. The HC method does not provide the temperature above 95 km; therefore, the columns with an altitude range greater than 95 km are shown as '-'.

Lidars	Difference (K)			**Au** = 0.9	**Au** = 0.8
	80-85 km	85-90 km	90-95 km	95-100 km	100-105 km
PCL(OEM) - URB	11.3	6.0	4.4	3.9	8.3
PCL(HC) - URB	12.8	8.1	6.7	-	-
PCL(OEM) - CSU	-	6.9	5.1	6.6	14.2
PCL(HC) - CSU	-	8.4	6.2	-	-
PCL(OEM) - upgraded CSU	5.6	4.1	3.8	7.8	13.5
PCL(HC) - upgraded CSU	6.7	4.7	3.4	-	-
CSU - URB	-	4.5	3.8	5.1	6.7
CSU - upgraded CSU	-	4.4	4.0	3.2	3.2
URB - upgraded CSU	7.3	4.6	5.7	7.1	5.6

Overall comparisons between the PCL climatologies and sodium lidar climatologies (Table 2.4) show that in the 85-90 and 90-95 km height ranges, where both the Rayleigh and Na methods have good measurement signal-to-noise ratio, the OEM-calculated temperatures show 20% better agreement with the sodium lidars than the HC method temperatures: that is, 5.0 K versus 6.3 K in average. The variability of the temperature difference between the sodium lidars themselves is around 4.5 K. The difference among the sodium lidars is approximately the same as the differences with the OEM-derived temperatures, meaning the temperatures derived using the OEM retrieval are approximately the same as those from the sodium lidars; this is contrary to the AS2007 comparison, which showed significant differences between the two techniques. Furthermore, the OEM temperature retrievals allow valid retrievals to be obtained in the 95-100 km altitude region, where the systematic uncertainty of the tie-on pressure of the HC-derived temperatures is too large for the temperatures to be useful. Possible sources of these differences were addressed in AS2007, but they did not have the uncertainty budget now available to assess systematic uncertainties. These differences

could include the following factors.

1. The assumption of a seed pressure can introduce uncertainty in the PCL temperature retrievals. Using an OEM allows us to calculate the effect of this assumption quantitatively (Fig. 2.9). In the altitude range of 80 to 95 km, it is less than 1.5 K, increasing to a maximum of 3.5 K at 100 km.

2. The effects of Rayleigh-scatter cross section, Rayleigh-scatter density, and mean molecular mass were mentioned in AS2007 as possible reasons for discrepancies with the sodium lidar temperatures. Figure 2.9 shows a quantitative determination of the magnitude of these effects. The uncertainties for the Rayleigh-scatter cross section and Rayleigh-scatter density are much less than the temperature differences between the two measurement techniques. Mean molecular mass uncertainty is larger than the other two parameters, but its maximum value is less than 0.7 K at 105 km.

3. The other significant contribution to the temperature uncertainty budget at higher altitudes is ozone cross section, whose uncertainty increases with altitude due to increasing measurement uncertainty (as do many of the retrieval uncertainties due to the model parameters). The uncertainty on the retrieved temperatures due to ozone reaches a maximum of 1 K at 100 km.

4. Geographic location could be another possible cause. The PCL is about 3° north of the sodium lidars and, while relatively close to URB in longitude, the PCL is 24° east of CSU. Hence, tides and planetary waves could be the primary cause of the temperature differences between the PCL, URB and CSU lidars. Gravity waves could also contribute, although the effect of gravity waves is minimized by averaging temperature over several hours and using common days in different years to calculate the composite climatology. Sica and Argall (2007) have shown that the seasonal gravity wave activity over London, Canada, is large and highly variable, and is possibly related to London's proximity to both Lake Ontario to the west and Lake Erie to the east. The effect of solar tides on the sodium lidar temperature is discussed in States and Gardner (2000b) and Yuan et al. (2006). The upgraded CSU is capable of continuous observation during day and night. Yuan et al. (2008) removed tidal signals from the mean values and
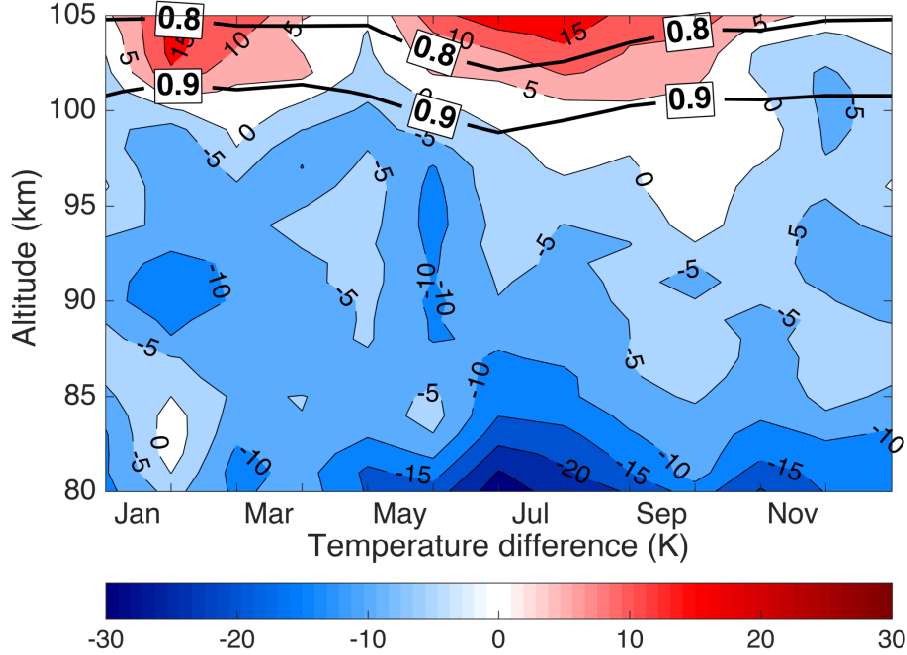
Figure 2.14: PCL temperature climatology difference from the URB sodium lidar climatology (PCL-URB). The horizontal black lines are the height below which the temperature climatology is more than 90% (0.9) and 80% (0.8) due to the measurements.

> calculated diurnal mean monthly temperatures. They show that the amplitude of the diurnal tide is around 5 K at night between 84 and 95 km, increasing to 8 K at 100 km. Hence, we conclude that large-scale waves cause many of the discrepancies between locations.

The comparison with sodium lidars shows that the PCL Rayleigh temperature climatology using the OEM in general agrees as well with the sodium lidar climatologies as the sodium climatologies agree with one another, validating the PCL OEM height-extended climatology.

2.5   Summary

Here we have confirmed the validity of using the OEM to retrieve Rayleigh-scatter lidar temperatures on a long-term measurement set. The results of our investigation using the OEM on 519 nights of measurements are summarized as follows.
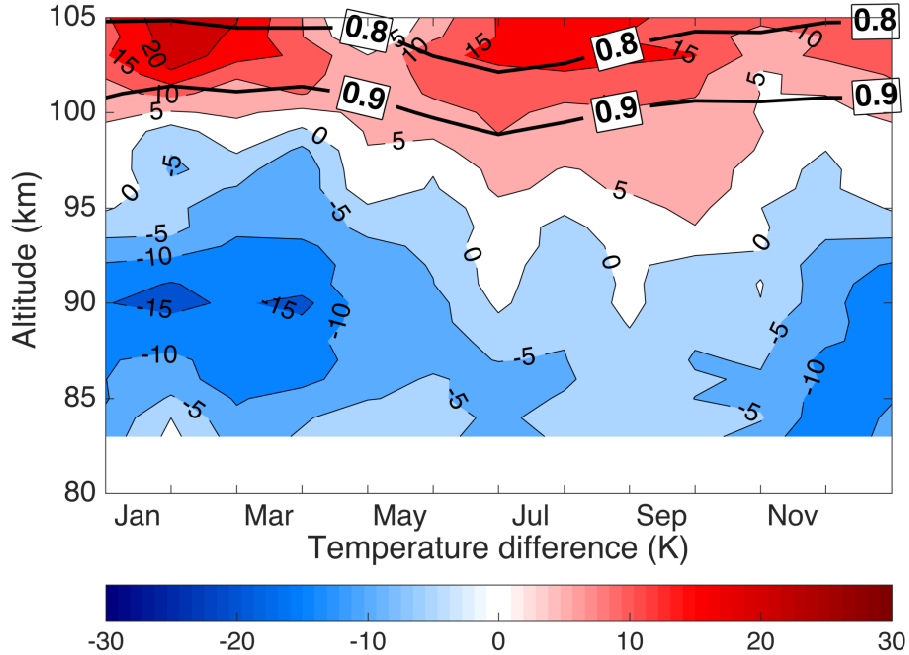
Figure 2.15: PCL temperature climatology difference from the CSU (1990-1999) sodium lidar climatology (PCL-CSU). The horizontal black lines are the height below which the temperature climatology is more than 90% (0.9) and 80% (0.8) due to the measurements.

1. Our OEM can estimate a valid cutoff height where the entire temperature profile below that level depends less than a specified level on the choice of the *a priori* temperature profile. Based on best practice in the OEM community, we suggest using measurements whose summed averaging kernels at a retrieval altitude are greater than 0.9.

2. The effect of the temperature *a priori* on the OEM result was evaluated using the CIRA-86 and US Standard model. It was shown that the effect of the *a priori* is much smaller than the statistical uncertainty below the OEM cutoff heights for the PCL.

3. We presented a full uncertainty budget for our climatology, which includes both random and systematic uncertainties, including the systematic uncertainty for nine model parameters including mean molecular mass, Rayleigh cross section, Rayleigh cross section variation with composition, seed pressure, air number density (for extinction), ozone absorption cross section, ozone density, and acceleration due to gravity. This uncertainty budget is available on a profile-by-profile basis.
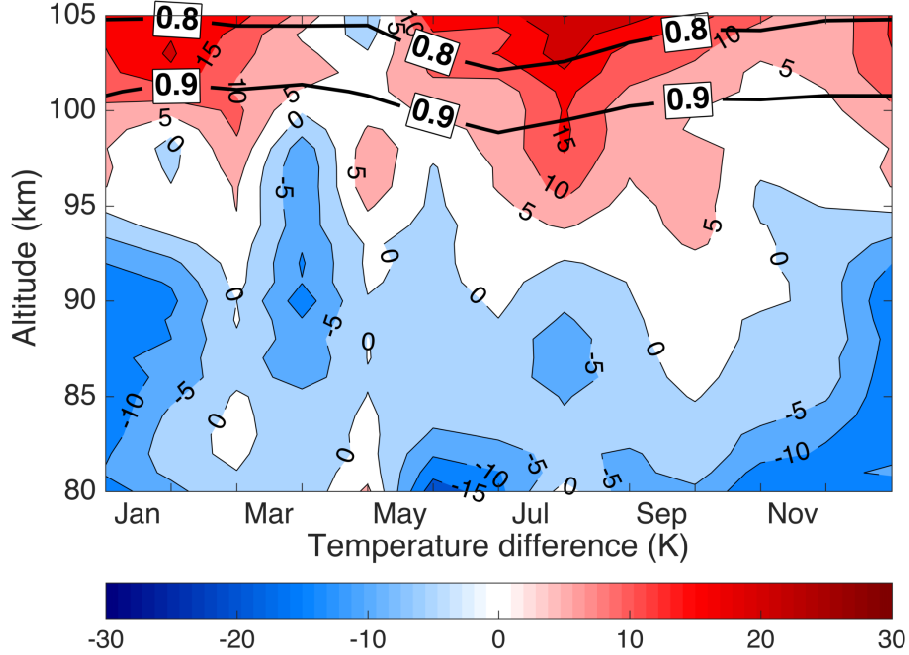
Figure 2.16: PCL temperature climatology difference from the upgraded CSU (2002-2006) sodium lidar climatology (PCL-upgraded CSU). The horizontal black lines are the height below which the temperature climatology is more than 90% (0.9) and 80% (0.8) due to the measurements.

4. The PCL uncertainties were compared to the uncertainty budget simulations presented by Leblanc et al. (2016b). The comparison shows in general similar orders of magnitude, except for the Rayleigh-scatter cross section, which has a larger difference but makes a very small (0.001 K) contribution to the uncertainty budget.

5. Our OEM computes the vertical resolution of each temperature profile. The vertical resolution is equal to the retrieval grid (1056 m) until about 75 km, where it starts to increase and is about 3 km around the 0.9 cutoff height.

6. The PCL temperature climatology is calculated using both the OEM and the HC method. By 15 km below the cutoff height, any differences in the temperature are within the statistical uncertainty at those heights. Our OEM retrieval determines temperature profiles, which reach 5 to 10 km higher than the temperature profiles calculated by the HC method due to the OEM's ability to evaluate the effect of seed

pressure on the retrieved temperature.

7. The temperature difference between the OEM PCL temperature climatology with the HC method PCL climatology using seed pressure was smaller than the temperature difference between the OEM PCL temperature climatology with the HC method temperature climatology using seed temperature. Hence, we recommend that when using the HC method it is better to take the seed pressure from the model than a seed temperature.

8. The PCL temperature climatology is compared with three other sodium lidar climatologies. The temperature differences between the PCL climatology using the OEM and the sodium lidar climatologies are smaller by $1\,\mathrm{K}$ than the differences between the PCL–OEM and the PCL–HC differences. The temperature differences between the PCL–OEM and the sodium lidars are within the temperature differences between the sodium lidars themselves (Table 2.4). The OEM provides the PCL temperature profiles to higher altitudes and these profiles show smaller differences with the sodium lidars than the HC method; thus, using the OEM improves the climatology between 80 and $100\,\mathrm{km}$, as validated by the sodium lidar measurements.

9. The statistical uncertainty of the sodium lidar temperatures is lowest in the $95 \pm 5\,\mathrm{km}$ region of the peak of the sodium layer. Here the precision is about $1\,\mathrm{K}$ to $2\,\mathrm{K}$ (Papen et al., 1995). The accuracy of the measurement in this region has been studied in detail by Krueger et al. (2015), who obtain an accuracy of 1 to $2.5\,\mathrm{K}$. The statistical uncertainty increases rapidly away from the sodium layer peak. The closest agreement between the PCL temperature climatology and the sodium lidars' climatology is in the range of 85 to $100\,\mathrm{km}$, with larger temperature differences below $85\,\mathrm{km}$ and above $100\,\mathrm{km}$ where the sodium density is lowest. The URB climatology, which was obtained from a station much closer in longitude to the PCL, shows better agreement than the CSU measurements, although all three sodium lidar climatologies have overall good agreement with the PCL OEM climatology. Overall the OEM provides closer temperature results to the sodium lidars than the HC method at all heights, and allows the climatology to extend to a greater altitude.

2.6 Conclusions

We have shown that using the OEM to retrieve temperature from Rayleigh-scatter lidar measurements has significant advantages over the traditional method, and the advantages shown in our initial study for a small number of nights is practical for a large dataset. These advantages include the ability to calculate a full uncertainty budget on a profile-by-profile basis, determination of the vertical resolution, and the availability of averaging kernels. Applying the OEM will help in the standardization of the uncertainty budget and vertical resolution calculations for comparisons between lidars, as well as comparisons among other instruments with differing vertical resolutions.

We found that a cutoff height of $\mathbf{Au} = 0.9$ is a good estimate for a cutoff height of the retrieval based on the comparison with the sodium lidars. It would be recommended to use the 0.9 height cutoff to minimize the effect of the *a priori* temperature profile on the temperature retrieval while keeping the *a priori* effect on the temperature retrieval less than the statistical uncertainty.

Sodium lidars are well characterized and make the best temperature measurements in the mesosphere and lower thermosphere for validation of the PCL temperature climatology, particularly as the URB and CSU systems are relatively near the PCL. The agreement between the OEM-based PCL climatology and the sodium lidars has improved over the traditional method, and the agreement between the PCL and the sodium lidars is typically as good as the agreement between the sodium lidars themselves. Much of the variability seen in the measurements made at the different locations is likely due to tides and planetary waves.

We hope the results of this study encourage other Rayleigh lidar groups to process their measurements using our OEM retrieval method.

Bibliography

Argall, P. S. and R. J. Sica. A comparison of Rayleigh and sodium lidar temperature climatologies. *Ann. Geophys.*, 25:27–35, 2007.

Arnold, Kam S. and C. Y. She. Metal fluorescence lidar (light detection and ranging) and the middle atmosphere. *Contemp. Phys.*, 44(1):35–49, 2003.

Bills, R. E., C. S. Gardner, and C. Y. She. Narrow band lidar technique for sodium temperature and doppler wind observations of the upper atmosphere. *Opt. Eng.*, 30, 1991.

Fleming, E. L., S. Chandra, M. R. Shoeberl, and J. J. Barnett. Monthly mean global climatology of temperature, wind, geopotential height and pressure for 0-120 km. *NASA Tech. Memo.*, NASA TM100697:85 pp, 1988.

Gardner, C. S., D. C. Senft, T. J. Beatty, R. E. Bills, and C. A. Hostetler. Rayleigh and sodium lidar techniques for measuring middle atmosphere density, temperature, and wind perturbations and their spectra. *In World Ionosphere/ Thermosphere Study Handbook*, 2: 141–187, 1989.

Gerding, M., J. Höffner, J. Lautenbach, M. Rauthe, and F.-J. Lübken. Seasonal variation of nocturnal temperatures between 1 and 105 km altitude at 54 n observed by lidar. *Atmos. Chem. Phys.*, 8(24):7465–7482, 2008.

Griggs, M. Absorption coefficients of ozone in the ultraviolet and visible regions. *J. Chem. Phys.*, 49:857–859, 1968.

Hamming, R. W. *Digital Filters*. Prentice Hall, Englewood Cliffs, New Jersey, third edition, 1989.

Hauchecorne, Alain, Marie-Lise Chanin, and P. Keckhut. Climatology and trends of the middle atmospheric temperature (33-87 km) as seen by rayleigh lidar over the south of france. *Journal of Geophysical Research: Atmospheres*, 96(D8):15297–15309, 1991.

Jalali, Ali. Extending and merging the purple crow lidar temperature rayleigh and vibrational raman climatologies. *Master's thesis, The University of Western Ontario*, 2490, 2014.

Krueger, David A., Chiao-Yao She, and Tao Yuan. Retrieving mesopause temperature and line-of-sight wind from full-diurnal-cycle na lidar observations. *Appl. Opt.*, 54:9469–9489, 2015.

Leblanc, T., R. J. Sica, J. A. E. Gijselvan , S. Godin-Beekman, A. Haefele, T. Trickl, G. Payen, and F. Gabarrot. Proposed standardized definitions for vertical resolution and uncertainty in the NDACC lidar ozone and temperature algorithms – Part 1: Vertical resolution. *Atmos. Meas. Tech.*, 9:4029–4049, 2016a.

Leblanc, T., R. J. Sica, J. A. E. Gijselvan , A. Haefele, G. Payen, and G. Liberti. Proposed standardized definitions for vertical resolution and uncertainty in the NDACC lidar ozone and temperature algorithms – part 3: Temperature uncertainty budget. *Atmos. Meas. Tech.*, 9(8):4079–4101, 2016b.

Leblanc, Thierry, I. Stuart McDermid, Philippe Keckhut, Alain Hauchecorne, C. Y. She, and David A. Krueger. Temperature climatology of the middle atmosphere from long-term lidar measurements at middle and low latitudes. *J. Geophys. Res.-Atmos.*, 103(D14): 17191–17204, 1998.

McPeters, R D, G J Labow, and J A Logan. Ozone climatological profiles for satellite retrieval algorithms. *J. Geophys. Res. Atmos.*, 112(D05308), 2007.

Mulaire, W. Department of defense world geodetic system 1984. its definition and relationship with local geodetic systems. *NIMA TR8350.2*, pages 1–175, 2000.

Nicolet, M. On the molecular scattering in the terrestrial atmosphere: an empirical formula for its calculation in the homosphere. *Planet. Space Sci.*, 32:1467–1468, 1984.

Papen, George C., William M. Pfenninger, and Dale M. Simonich. Sensitivity analysis of na narrowband wind–temperature lidar systems. *Appl. Opt.*, 34:480–498, 1995.

Ramaswamy, V., M.-L. Chanin, J. Angell, J. Barnett, D. Gaffen, M. Gelman, P. Keckhut, Y. Koshelkov, K. Labitzke, J.-J. R. Lin, A. O'Neill, J. Nash, W. Randel, R. Rood, K. Shine, M. Shiotani, and R. Swinbank. Stratospheric temperature trends: Observations and model simulations. *Rev. Geophys.*, 39(1):71–122, 2001. ISSN 1944-9208.

Randel, William, Petra Udelhofen, Eric Fleming, Marvin Geller, Mel Gelman, Kevin Hamilton, David Karoly, Dave Ortland, Steve Pawson, Richard Swinbank, Fei Wu, Mark Bald-

win, Marie-Lise Chanin, Philippe Keckhut, Karin Labitzke, Ellis Remsberg, Adrian Simmons, and Dong Wu. The sparc intercomparison of middle-atmosphere climatologies. *J. Climate*, 17(5):986–1003, 2004.

Randel, William J., Keith P. Shine, John Austin, John Barnett, Chantal Claud, Nathan P. Gillett, Philippe Keckhut, Ulrike Langematz, Roger Lin, Craig Long, Carl Mears, Alvin Miller, John Nash, Dian J. Seidel, David W. J. Thompson, Fei Wu, and Shigeo Yoden. An update of observed stratospheric temperature trends. *J. Geophys. Res.-Atmos.*, 114(D2), 2009. ISSN 2156-2202. D02107.

Randel, William J., Anne K. Smith, Fei Wu, Cheng-Zhi Zou, and Haifeng Qian. Stratospheric temperature trends over 1979-2015 derived from combined ssu, mls, and saber satellite observations. *J. Climate*, 29(13):4843–4859, 2016.

She, C. Y., S. Chen, Z. Hu, J. Sherman, J. D. Vance, V. Vasoli, M. A. White, J. Yu, and D. A. Krueger. Eight-year climatology of nocturnal temperature and sodium density in the mesopause region (80 to 105 km) over Fort Collins (41N, 105W). *J. Geophys. Res.*, 27:3289–3292, 2000.

Sica, R. J. and P. S. Argall. Seasonal and nightly variations of gravity-wave energy density in the middle atmosphere measured by the purple crow lidar. *Ann. Geophys.*, 25:2139–2145, 2007.

Sica, R J and A Haefele. Retrieval of temperature from a multiple-channel Rayleigh-scatter lidar using an optimal estimation method. *Appl. Optics*, 54(8):1872–1889, 2015.

States, R. J. and C. S Gardner. Thermal structure of the mesopause region (80–105km) at 40 degrees N latitude. Part I: Seasonal variations. *J. Atmos. Sci.*, 57:66–77, 2000a.

States, Robert J. and Chester S. Gardner. Thermal structure of the mesopause region (80âĂŞ105 km) at 40 n latitude. part ii: Diurnal variations. *J. Atmos. Sci.*, 57(1):78–92, 2000b.

Yuan, T., C.-Y. She, D. A. Krueger, F. Sassi, R. Garcia, R. G. Roble, H.-L. Liu, and H. Schmidt. Climatology of mesopause region temperature, zonal wind, and meridional

wind over Fort Collins, Colorado (41N, 105W), and comparison with model simulations. *J. Geophys. Res.*, 113, 2008.

Yuan, Tao, C. Y. She, Maura E. Hagan, B. P. Williams, Tao Li, Kam Arnold, Takuya D. Kawahara, P. E. Acott, J. D. Vance, David Krueger, and Raymond G. Roble. Seasonal variation of diurnal perturbations in mesopause region temperature, zonal, and meridional winds above fort collins, colorado (40.6 n, 105 w). *J. Geophys. Res.-Atmos.*, 111(D6), 2006. ISSN 2156-2202. D06103.

Chapter 3

Removing *a priori* Information from Lidar Optimal Estimation Method Retrievals[1]

3.1 Introduction

Rodgers (2011) introduced an Optimal Estimation Method (OEM) based on information theory to use for atmospheric remote sensing retrievals. The OEM has primarily been used in passive remote sensing (Rodgers, 1976; Cunnold et al., 1989; Boersma et al., 2004) and it was not until recently that the OEM was applied to lidar measurements to retrieve atmospheric aerosol properties, temperature, and water vapor profiles (Povey et al., 2014; Sica and Haefele, 2015, 2016). OEM is advantageous for lidar work not only because desired geophysical quantities are retrieved (e.g. temperature, water vapour mixing ratio, etc.) but also because it produces averaging kernels and a full uncertainty budget on a profile-by-profile basis.

Lidars have high temporal and spatial resolution compared to passive remote sensing instruments, coupled with high signal-to-noise (SNR) ratio measurements over much of their dynamic range, and thus have averaging kernels close to unity for the majority of their re-

---

[1]Jalali, A., & Hicks-Jalali, S., & Sica, R. J., & Haefele, A., & von Clarmann, T. 2018, Atmospheric Measurement Techniques, https://doi.org/10.5194/amt-2018-347.

trievals with a grid spacing much finer than passive instruments. At most retrieval altitudes, the majority of the information comes from the lidar measurements. However, near the top of the lidar retrieval range, and in other regions where the SNR is low, the *a priori* contribution to the retrieval increases and consequently the amount of information from the measurement decreases. The *a priori* influence at the top of the retrieval should be considered when comparing OEM lidar measurements, particularly if different *a priori* profiles are used.

An example of the *a priori*'s influence is shown in Fig. 1 of Jalali et al. (2018). Jalali et al. (2018) used more than 500 nights of measurements from the Purple Crow Lidar in London, Ontario between 1994 and 2013 to calculate the OEM temperature climatology. The cutoff height used for the climatology was the altitude at which the measurement response equaled 0.9, or where the retrieval is roughly comprised of 90% measurements and 10% *a priori* information. In order to see the influence of the *a priori* on the temperature retrieval, temperature profiles from two different models, CIRA 86 and the US Standard Model (NASA, 1976), were chosen to use as *a priori* temperatures. Temperatures were retrieved using both *a priori* profiles, and the differences between the two were compared at the altitudes where $\mathbf{Au} = 0.9$ and $\mathbf{Au} = 0.99$. The distribution of the influence of the *a priori* at these altitudes for the entire climatology was also calculated (Fig. 3.1). However, the temperature *a priori*'s effect is always one or two degrees smaller than the random uncertainties at these altitudes.

The mean value of the histogram at the altitude where $\mathbf{Au} = 0.99$ is $0.53 \pm 1.29\,\mathrm{K}$ and the mean at $\mathbf{Au} = 0.9$ increases to $0.96 \pm 3.25\,\mathrm{K}$. There is a positive bias in both histograms which is due to the fact that the monthly CIRA-86 temperature profiles are consistently warmer than the yearly US Standard Model profile. The effect of the *a priori* increases as the values of $\mathbf{Au}$ decrease. Also, all values in the histogram are within two sigma of the statistical uncertainty of the PCL climatology.

As Rodgers (2011) suggested, it is important to pick the most accurate *a priori* for the retrieval. We used the CIRA-86 and US Standard Model to investigate the influence of the choice in *a priori* more clearly, as the differences between these two model temperatures profiles is large. If *a priori* profile values from the CIRA-72 and CIRA-86 models had been chosen for comparison, the mean values on the histogram would have been much smaller.
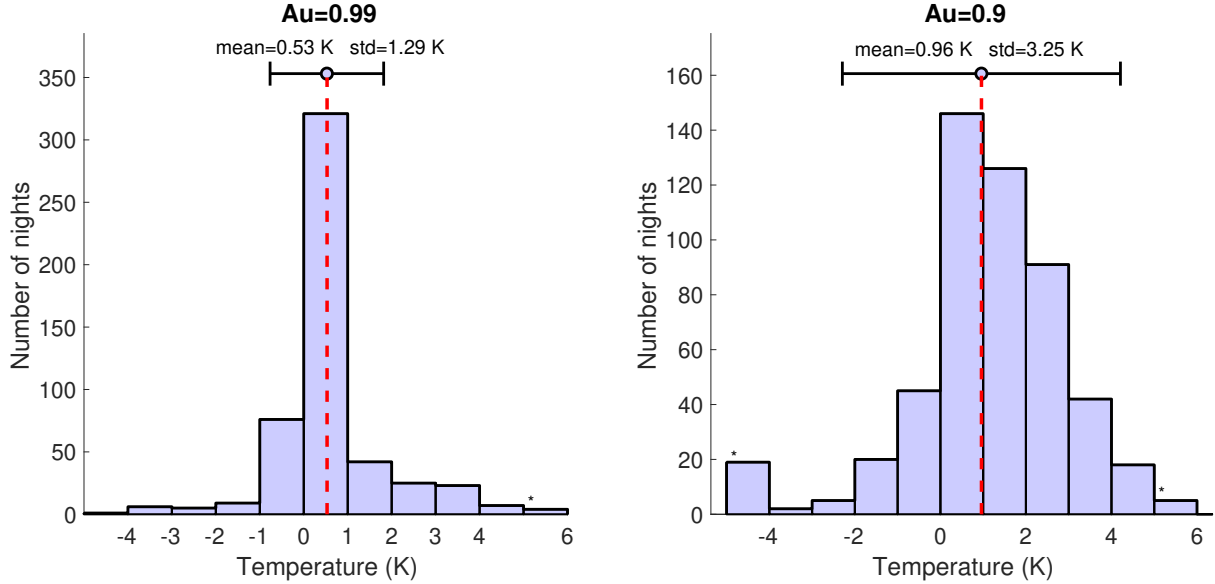
Figure 3.1: Distribution of the differences in temperatures retrieved at the altitudes where the sum of the averaging kernels (**Au**) is 0.99 (a) and 0.9 (b) using two *a priori* temperature profiles - the US Standard Model and CIRA-86 for over 500 nights as detailed in Jalali et al. (2018). The red dashed line shows the mean. For each case, the difference in temperatures is always smaller than the statistical uncertainty at the same altitude.

Several solutions regarding reducing the *a priori*'s influence on the retrieval have been suggested by Vincent et al. (2015), Ceccherini et al. (2009), Von Clarmann and Grabowski (2007) and Joiner and Silva (1998). Their method to minimize the effect of the *a priori* was based on transforming a regularized to a maximum likelihood retrieval by moving from a fine grid to a coarser grid. Our work applies the methodology of Von Clarmann and Grabowski (2007) to a Rayleigh lidar OEM temperature retrieval and a Raman lidar OEM water vapour retrieval. The method uses a grid transformation on the retrieved temperature and water vapor lidar profiles to remove the *a priori* temperature and water vapour contribution. The transformation is applied in such a way that each final grid point carries roughly one degree of freedom. Then, the retrieved profiles are calculated on the coarse grid by re-running the OEM in a way that the effect of the *a priori* constraint is minimized.

We have used two lidars in this study, whose specifications are discussed in more detail in Section 2. Section 3 summarizes some basic foundation material of the OEM which will

be referenced throughout the paper. Section 4 discusses the *a priori* removal methodology with a simple example. The method is then applied in Section 5 for three cases: Raman water vapour daytime, Raman water vapour nighttime, and Rayleigh nightly temperature retrievals. Section 6 discusses the differences between our practical application and the method in Von Clarmann and Grabowski (2007) and some of the method's advantages. Sections 7 and 8 are the Summary and Conclusions respectively.

3.2 Description of the Raman Lidar for Meteorological Observation

Two lidars were used in this study, the RAman Lidar for Meteorological Observation (RALMO) in Payerne, Switzerland and the Purple Crow Lidar in London, Ontario. A detailed description of the PCL is given in Chapter 2. RALMO was used for the water vapour daytime and nighttime retrievals and the PCL was used for the Rayleigh temperature retrievals.

RALMO is located at the MeteoSwiss research station in Payerne, Switzerland (46.81° N, 6.94° E, 491 m a.s.l.). RALMO was built at the École Polytechnique Fédérale de Lausanne (EPFL) and was designed as an operational lidar for model validation and climatological research. RALMO uses a 355 nm wavelength laser operating at 30 Hz with a nominal power of 300 mJ. Measurements are made in one-minute intervals with an altitude resolution of 3.75 m. A typical 30 min water vapour profile will extend to 10 - 12 km at night and 4 to 5 km during the day. Detailed specifications for the RALMO can be found in Dinoev et al. (2013) and Brocard et al. (2013). The water vapour retrieval for daytime and nighttime followed the same procedure as described in Sica and Haefele (2016), with the exception that we now retrieve the overlap, which is no longer a model parameter. Only raw (uncorrected) photocount measurements are used for the water vapour retrievals. The lidar input measurements are 30 min profiles beginning at the same time as the coincident radiosonde launch from the Payerne station. The US Standard Model water vapour profile is used as the water vapour *a priori* input for both daytime and nighttime retrievals.

3.3 Methodology

Our objective in this study is to find a practical method to remove the *a priori* information from the retrieval vector. We have based our work upon the methodology of Von Clarmann and Grabowski (2007), and have developed a quick and straightforward method to remove the *a priori* from the lidar retrieval. Von Clarmann and Grabowski (2007) proposed removing the effect of the *a priori* by using an information-centered grid approach. Each level of the retrieval on the information-centered grid contains one degree of freedom and therefore, the number of degrees of freedom of the signal is the same as the number of the retrieval levels. In this condition, the formal *a priori* information can be removed without de-stabilizing the retrieval.

To create an information-centered grid that contains close to one degree of freedom per level requires the averaging kernel of the fine grid retrieval. For a lidar, this is either the raw measurement spacing or a grid found by integrating some number of raw measurements into larger bins. Therefore, the first step is to run the OEM retrieval following the same procedures as in Sica and Haefele (2015) or Sica and Haefele (2016). This produces a temperature or water vapor retrieval along with their respective averaging kernel matrices and uncertainty budgets on the "fine grid" or first retrieval grid. For RALMO water vapour retrievals, the fine grid altitude resolution is 100 m and 50 m resolution for the daytime and nighttime retrievals respectively, and 1024 m for the PCL Rayleigh temperature retrieval. The fine grid averaging kernel contains the information regarding the degrees of freedom of the retrieval along the diagonal elements of the matrix. The cumulative trace of the averaging kernel is the total degrees of freedom of the retrieval (Eq. 1.32).

To illustrate the method, we will give a simple example with the fine grid levels, diagonal components of the averaging kernel matrix, and the cumulative trace of the averaging kernel, as shown in Table 3.1.

We then use the triangular representation from Von Clarmann and Grabowski (2007) to create the information-centered grid using the fine grid averaging kernel. First, the cumulative trace of the averaging kernel matrix is used to determine the amount of information

Fine Grid Levels	Diagonal elements of **A**	Cumulative Trace of **A**
1	1	1
2	1	2
3	1	3
4	1	4
5	0.9	4.9
6	0.8	5.7
7	0.7	6.4
8	0.6	7.0
9	0.5	7.5
10	0.4	7.9
11	0.2	8.1
12	0.1	8.2

Table 3.1: A simple example for demonstrating the averaging kernel matrix's role in finding the coarse grid which resembles the typical structure of a lidar temperature retrieval averaging kernel. The first column is the retrieval level and for lidar OEM retrievals is typically an altitude. The second column is the elements along the diagonal of the averaging kernel matrix **A**. The third column is the cumulative trace of **A**, where the last value determines the number of degrees of freedom per grid point for the coarse grid using Eq. 3.1.

needed for each grid point on the coarse grid using Eq. 3.1:

$$dgf_c = \frac{dgf}{int(dgf) - 1} \approx 1, \tag{3.1}$$

where dgf_c refers to the degrees of freedom per level on the coarse grid, dgf is the cumulative trace of the fine grid averaging kernel matrix (Eq. 1.32), and $int(dgf)$ is the integer value of dgf. The degrees of freedom per grid point is determined by dividing the total degrees of freedom by one less than the integer value of the total. For example, if the total degrees of freedom of the retrieval is 8.2, then the degrees of freedom per grid point is $8.2/(8\text{-}1) = 1.1$ degrees of freedom per grid point. In the triangular representation the information is spread over $dgf - 1$ grid points because the first and last points remain the same as those in the
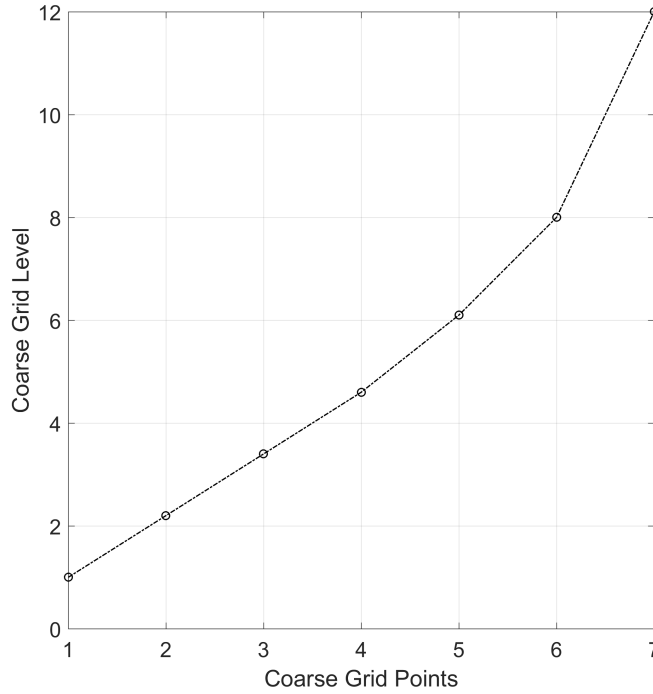
Figure 3.2: The coarse grid levels are shown for the example case as a function of the cumulative trace of the averaging kernel matrix. The total degrees of freedom for the retrieval is 8.2, which is spread over the entire retrieval grid such that each point has roughly one degree of freedom. As the SNR of the measurements decreases, more fine grid points are used in the coarse grid, therefore the distance between points generally increases with altitude.

fine grid. It is then necessary to interpolate the fine grid to the points where the diagonal elements are equal to the appropriate degrees of freedom to create the coarse grid. As each grid point contains equal amounts of degrees of freedom, the grid points are distributed irregularly. The final levels which are used in the coarse grid are shown in Fig. 3.2. In this case, we now have coarse grid points at 1, 2.2, 3.4, 4.6, 6.1, 8, and 12. As the sensitivity of the averaging kernel decreases the number of points used in the coarse grid from the fine grid increases due to decreasing lidar signal level with altitude.

The resulting coarse grid is then used as the retrieval grid for a second iteration of the OEM calculation. However, before running the retrieval again it is necessary to remove the regularization term, or equivalently, the inverse of the *a priori* covariance matrix $(\mathbf{S_a^{-1}})$ in

86

Eq. 1.29. If $\mathbf{S_a^{-1}}$ is set to zero, the optimal estimation becomes the unconstrained weighted least squares solution (Von Clarmann and Grabowski, 2007). We set $\mathbf{S_a^{-1}}$ to be close to zero by choosing a large uncertainty for the *a priori* covariance matrix.The OEM is then run using the new coarse retrieval grid, and the effect of the *a priori* is minimal due to minimizing the regularization term. The coarse grid averaging kernel now equals one at all levels.

3.4   Results

We now apply our information-centered approach, using the triangular representation from Von Clarmann and Grabowski (2007), to lidar OEM retrievals in order to minimize the effect of the *a priori*. We will examine the method's effectiveness with RALMO daytime and nighttime water vapor retrievals, as well as with a PCL Rayleigh temperature retrieval. This method is also applicable in general, and can be applied to other lidar retrievals. First, we will discuss the results from the triangular representation and the creation of the "coarse grid" and how it is used as the new retrieval grid. Then we will discuss its effect on the retrieval, vertical resolution, uncertainty budgets, and averaging kernel.

3.4.1   Daytime RALMO water vapor *a priori* removal

RALMO water vapour mixing ratio retrievals typically extend up to 4 or 5 km due to the large daytime background signal. This daytime water vapor retrieval on 22 January 2013 at 1200 UT (Fig. 3.5) shows the large impact our method has on low signal-to-noise ratios, which occur during the daytime due to the high solar background or in dry layers. The example retrieval is a 30 min integration obtained in conjunction with a Vaisala RS92 radiosonde launch from the Payerne station. The input data grid for this case was binned to 50 m to remove numerical features in the retrieval due to the high background noise levels.

The daytime case fine grid averaging kernels (Fig. 3.3a) quickly drop below 1 after 2 km due to a dry layer. The measurement response is shown by the red line and drops below the altitude at which $\mathbf{Au} = 0.9$ at 2.7 km, or the last altitude at which we consider the retrieval to have significant influence from the *a priori*. The coarse grid averaging kernels (Fig. 3.3b), by design, are all equal to 1 as discussed in Sect. 3.3 and reach up to 10 km. While the coarse

grid insures that each altitude has 1 degree of freedom, we do not necessarily consider the entire retrieval valid, which will be discussed further below. The vertical resolution of each
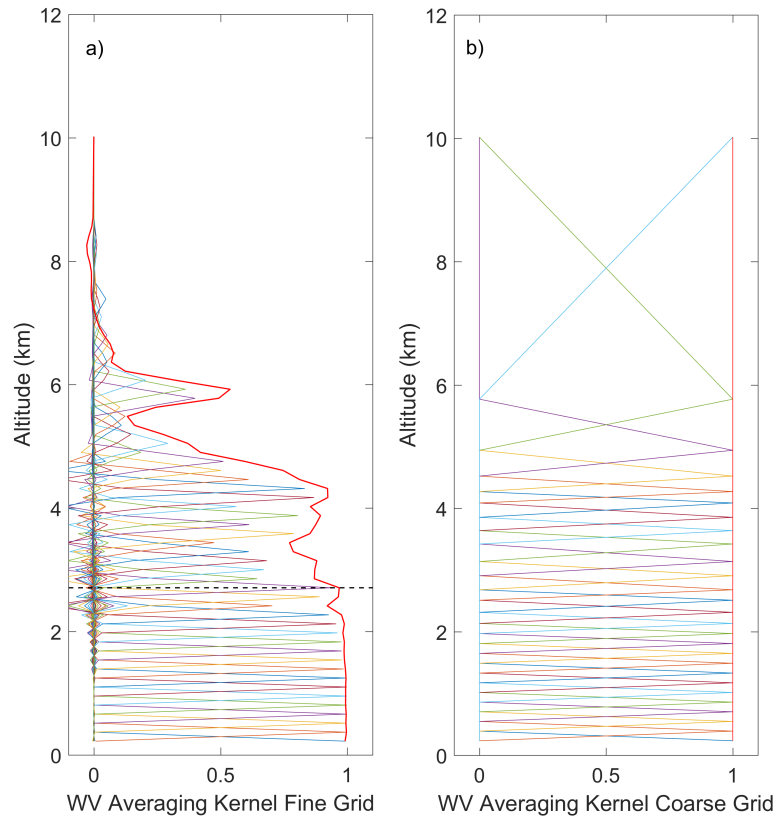
Figure 3.3: The clear daytime water vapour averaging kernel matrix for 22 January 2013 at 1200UT (a) on the fine grid and (b) on the coarse grid. Every other averaging kernel has been plotted for clarity. a)The measurement response **Au**, or the sum of the averaging kernel rows, is the red solid line. The horizontal dashed line is the height at which the measurement response is equal to 0.9 and is the line above which we would consider there to be large influence from the *a priori*. b) The coarse grid averaging kernels all equal 1 and reach up to the last retrieval altitude at 10 km.

point on the fine and coarse retrieval grids is shown in Fig. 3.4. In this case, the fine grid averaging kernels are never exactly 1, therefore they have some *a priori* contribution which is why the vertical resolution is generally lower in the coarse grid retrieval. The second to last point in the coarse retrieval grid has a vertical resolution of over 600 m. The coarse grid

points which have incorporated more fine grid points have a lower vertical resolution than others (between 2.8 and 10 km).
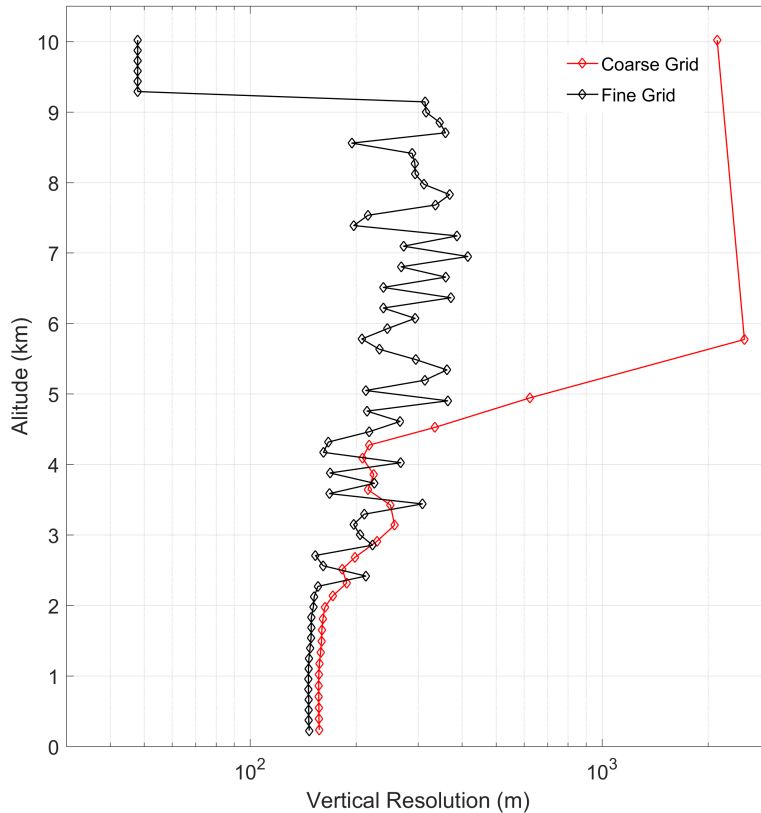
Figure 3.4: The vertical resolution profile on 22 January 2013 1200 UT. The vertical resolution will decrease on the coarse grid as the points are used to reach one degree of freedom. The last two points have vertical resolutions of several hundred meters and are not used in the retrieval.

The daytime water vapor fine and coarse grid retrievals are shown in Fig. 3.5a and Fig. 3.5b respectively. The fine and coarse grid retrievals are the same up to 2.5 km, at which point the coarse grid retrieval (in red) begins to more closely follow the path of the radiosonde and the traditional profile (dotted blue) and not the fine grid retrieval (black). The coarse grid retrieval agrees with the radiosonde until 4.5 km. At 4.8 km the statistical uncertainty is above 100%, and the last two points are above 80% statistical uncertainty; therefore, the retrieval is no longer viable. All valid points are below the red dotted line.

The large peaks in the fine grid retrieval above 5 km show features that are numerical and not physical. If we consider the last valid point to be 4.5 km with a statistical uncertainty of 27%, the *a priori* removal method extends the valid altitude range of the daytime OEM retrievals by 2 km.
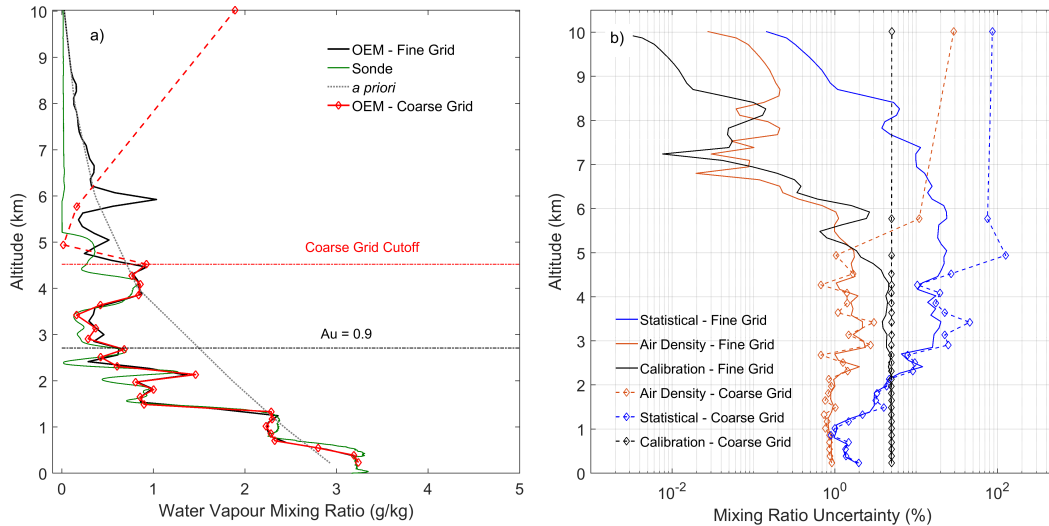
Figure 3.5: a) The retrieved daytime water vapour profile for 22 January 2013 1200 UT. The fine grid retrieval is in black and includes the *a priori* information. The coarse grid retrieval is in red and the *a priori*(grey) has been removed. The radiosonde is shown in green. The points which we do not consider meaningful because their uncertainties are larger than 80% in the retrieval are shown in dashed red lines. The coarse grid retrieval increases the last valid point by 2 km (red dashed line) and now more closely resembles the radiosonde above the original cutoff altitude of 2.7 km (black dashed line). b) The three primary contributors to the uncertainty budget on January 22 2013 1200 UT are shown for comparison: the statistical uncertainty, the uncertainty due to the calibration constant, and the uncertainty due to air density. The solid lines are the uncertainties from the fine grid retrieval, and the dashed lines are from the coarse grid retrieval. The *a priori* begins influencing the profile above 2 km where the uncertainty increases.

The three main components of the uncertainty budget are shown in Fig. 3.5b. The fine grid statistical and air density uncertainties increase with altitude due to decreasing SNR of the return photocounts and then decrease as the retrieval falls back to the *a priori* as

the signal goes to zero. The coarse grid statistical uncertainties and the uncertainty due to air density continue to increase with altitude, instead of falling back to zero, on the coarse grid because the *a priori* has been removed. The *a priori* covariance matrix is now zero in Eq. 1.30. The *a priori* covariance also acts as a constraint on the uncertainty by minimizing the gain, which acts as an scaling factor for the uncertainties (Rodgers, 2011). When the *a priori* covariance is removed, the solution space is no longer constrained and the coarse grid uncertainties increase compared to the fine grid uncertainties. The calibration uncertainty also increases, but now remains constant at all altitudes with the exception of the last point, as it is no longer influenced by the *a priori* constraint. The second-to-last point in the statistical uncertainty has a mixing ratio uncertainty of 100% due to the lack of signal above 4.5 km. Therefore, the meaningful section of the coarse grid retrieval is 4.5 km and below. The maximum uncertainty is 46% statistical uncertainty at 3.8 km, where the water vapour signal is very small due to the presence of a dry layer at that altitude. While the *a priori* removal technique increases the maximum retrieval altitude, in addition to removing the contribution from the *a priori* profile, it will increase the statistical uncertainty of the retrieval as well.

Finally, we compare the fine and coarse grid retrievals with the radiosonde profile in Fig. 3.6. Below 2.3 km, where the fine grid *a priori* influence is below 10%, both of the retrievals are equivalent and show the same difference with respect to the radiosonde. However, between 2.3 and 4.8 km, where the fine grid retrieval has above 10% *a priori* information, the coarse grid retrieval more closely matches the radiosonde, and reduces the difference by 10 to 50% depending on the altitude. Above 4.8 km the coarse grid and fine grid are no longer valid due to the lack of signal at those altitudes. The coarse grid method improves the retrieval in regions where the *a priori* has significant influence and performs as we would expect.

3.4.2 Nighttime RALMO water vapour *a priori* removal

The nighttime retrieval uses a 30-minute integration on 24 April 2013 0000 UT which coincides with the time of the radiosonde launch. The fine retrieval grid for the RALMO water vapor retrieval is 50 m.
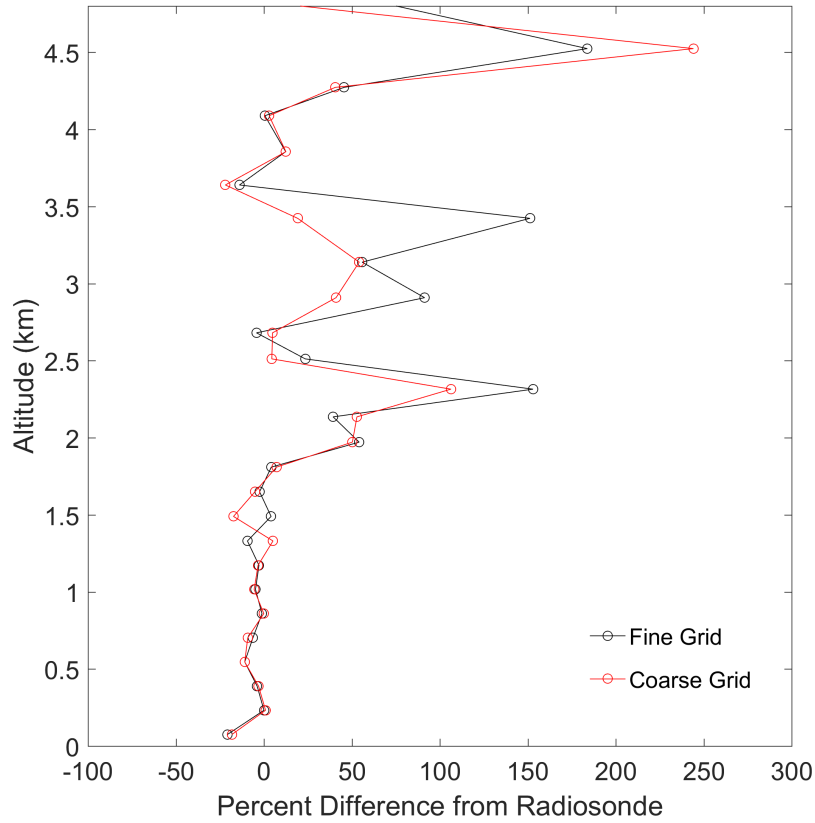
Figure 3.6: The percent difference between the radiosonde and the fine and coarse grid retrievals on 22 January 2013 1200 UT. The two retrievals are the same below 2 km, where the fine grid retrieval has less than 10% of *a priori* contribution. However, the coarse grid retrieval is closer to the radiosonde above 2 km and decreases the percent difference between the fine grid and the radiosonde by up to 50% in regions where the *a priori* contributes to more than 10% to the fine grid retrieval. Above 4.5 km the statistical uncertainties are too large to consider the retrieval meaningful.
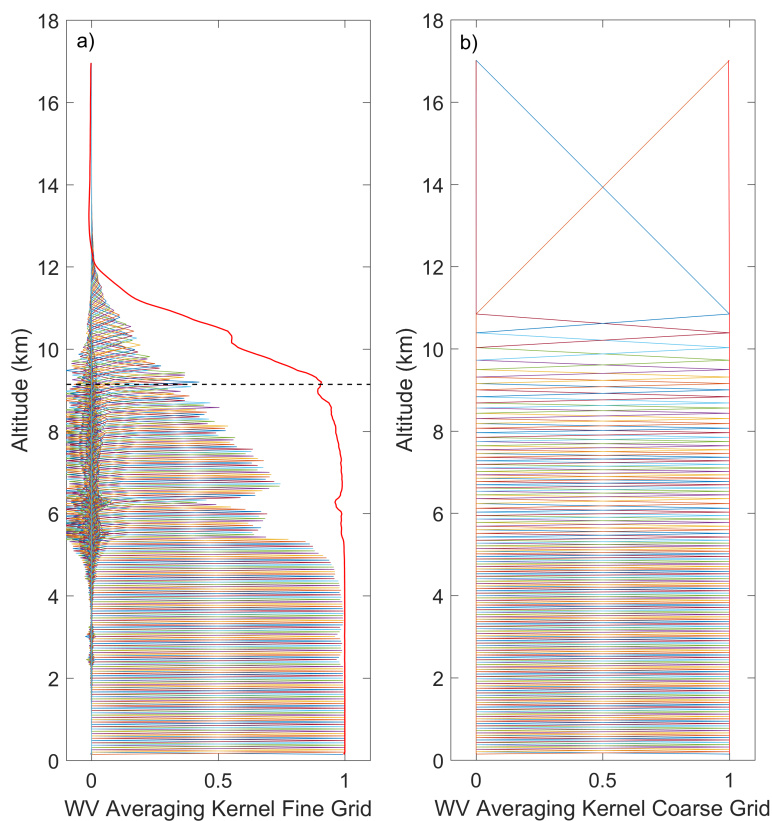
Figure 3.7: The averaging kernel matrix for the nighttime water vapour retrieval on 24 April 2013 0000 UT. a)The fine grid retrieval with a maximum altitude of 9.1 km (black dashed line). The measurement response is shown in red. b) The coarse grid retrieval, where each averaging kernel is 1 for all altitudes.

The averaging kernel matrix for the fine and coarse grid retrievals is shown in Fig. 3.7a and Fig. 3.7b, respectively. The altitude where $\mathbf{Au} = 0.9$ for the fine grid retrieval is at 9.1 km, which is typical for a 30 min nighttime measurement. The coarse grid averaging kernels all equal 1, with the second to last altitude at 11 km.

Unlike the daytime case, the nighttime vertical resolution between the fine and coarse grid retrievals is very close up to 5 km where they begin to diverge (Fig. 3.8). This is because the nighttime averaging kernels are very close to 1 until 5 km, therefore the fine and coarse grid are the same or very close to each other. As the *a priori* enters the signal, more points from the fine grid are used to create the coarse grid, resulting in larger coarse grid
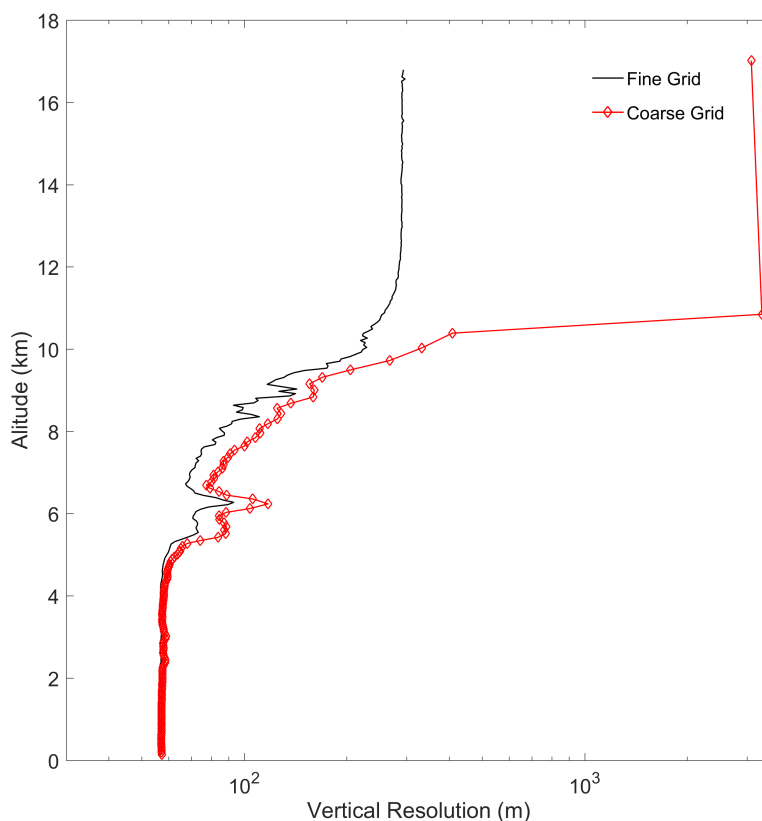
Figure 3.8: The vertical resolution for April 24 2013 0000 UT. The vertical resolution on the coarse grid retrieval decreases as more points are added to ensure that each bin has one degree of freedom. The coarse grid resolution is shown in red and each point is marked. The fine grid has points every 50 m therefore they are not shown individually.

averaging kernels and decreasing the vertical resolution. Figure 3.9 shows the final water vapor retrievals on the fine and coarse grid, as well as a GRUAN Vaisala RS92 radiosonde profile and the traditional method results for comparison. Both fine and coarse grid profiles agree past the 0.9 cutoff and up to 9 km at which point the coarse grid retrieval diverges from both the fine grid retrieval and the radiosonde. We do see small differences in dry layers where the signal level is lower, however, the differences are inside the total uncertainty. The last four points in the retrieval are shown in dashed lines because we do not consider them to be meaningful points as their total uncertainties are 70% or larger.

The uncertainties for the nighttime retrievals are shown in Fig. 3.9b. Similarly to the
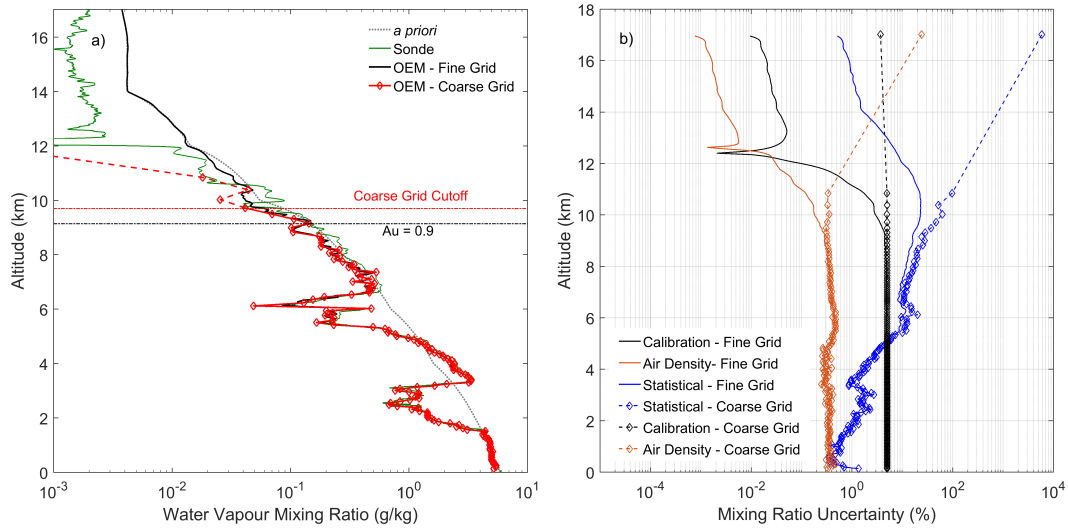
Figure 3.9: a)The water vapour retrieval for 24 April 2013 0000 UT. The fine grid retrieval is in black, the coarse grid retrieval is in red. In general, both OEM retrievals on the coarse and fine grid, and the radiosonde agree until the original cutoff altitude at 9.1 km (dashed black line). The dashed red lines above 9.7 km show the points we do not consider meaningful due to their large uncertainties. Therefore, the *a priori* removal technique increases the last altitude bin by 600 m. The method is limited by the lack of water vapour in the upper troposphere which causes a large and rapid drop in signal. b)The three largest uncertainty components are compared here on the fine and coarse grid. The drawback of the *a priori* removal technique is that while you gain in altitude, you increase the uncertainty. At 9.7 km the statistical uncertainty is 52%, which is where we no longer consider the rest of the retrieval to be viable.

daytime retrievals, we have shown the top three uncertainty contributors for comparison. Below 5 km the uncertainties are the same, as there is no influence from the *a priori*. However, above 5 km the uncertainties begin to increase due to the removal. The statistical uncertainty increases to almost 100% uncertainty at the second-to-last point due to the lack of signal above 11 km.The mixing ratio uncertainty due to the calibration uncertainty is now constant with altitude, which we would intuitively expect and contributes roughly 5% uncertainty to the mixing ratio measurements. The uncertainty due to air density increases by a maximum of 0.2% at the second-to-last point. We would consider anything above 9.7 km to be invalid
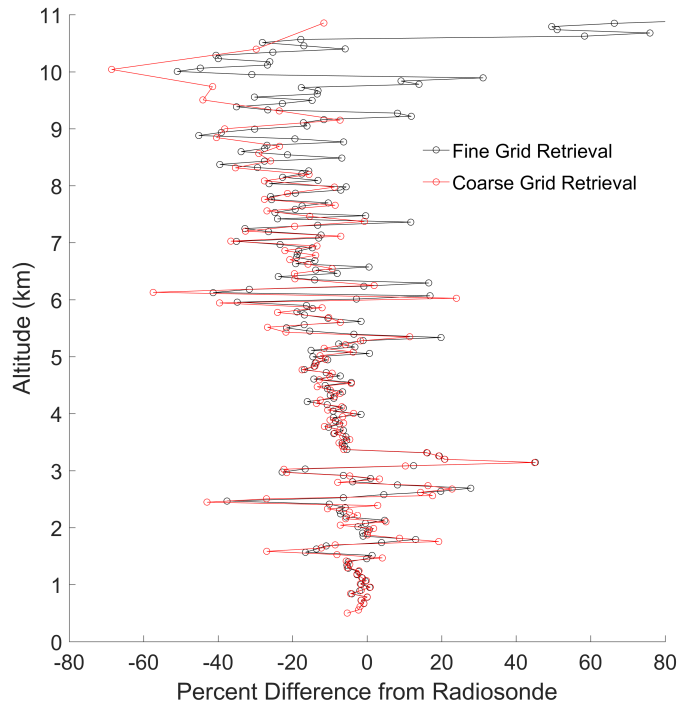
Figure 3.10: The percent difference from the radiosonde for both the fine and coarse grid retrievals. Both show similar differences with the radiosonde and the last valid height is 9.7 km.

since points above that height have a total uncertainty of 60% or higher. The last valid point has a total uncertainty of 52% at 9.7 km. Therefore, the *a priori* removal technique increases the maximum valid altitude of the retrieval by 600 m.

The fine and coarse grid retrievals do not change very much with respect to each other until 9.1 km where the averaging kernels begin to drop off significantly. They both produce similar differences with the radiosonde (Fig. 3.10) until 9.7 km where the coarse grid retrieval shows a larger difference with the radiosonde. However, above this altitude we would no longer consider the coarse grid retrieval viable since its total uncertainties at that height are above 70%.

Using the *a priori* removal technique for nighttime retrievals may be helpful when trying to improve water vapour measurements of the Upper Troposphere and Lower Stratosphere (UTLS) region. However, in this case, because the nighttime measurements have large SNRs

and a rapid change from high to low signal values, we do not see as large of a difference between the coarse and fine grid retrievals as we do in the daytime retrievals.

3.4.3 Purple Crow Lidar Rayleigh temperature *a priori* removal

We picked a sample night, 12 May 2012, from the Rayleigh temperature climatology in Jalali et al. (2018) to illustrate the *a priori* removal procedure for a Rayleigh temperature retrieval. The original OEM retrieval fine grid was 1024 m, and the *a priori* temperatures were taken from the CIRA-86 model. The details regarding the OEM retrieval are discussed in Sica and Haefele (2015) and its applied result to the climatology is discussed in Jalali et al. (2018).

The averaging kernels for the fine grid and coarse grid retrievals are shown in Fig. 3.11a and Fig. 3.11b. The red line is the measurement response or the estimate of the averaging kernel's sensitivity to the measurements. The height at which the measurement response equals 0.9 was chosen as a "cutoff" height in Jalali et al. (2018), which is shown in Fig. 3.11a with a dashed line. After applying the *a priori* removal, the averaging kernel on the coarse grid is equal to 1 at each point. Fig. 3.11b shows that at the coarse grid points, the averaging kernel is completely sensitive to the measurements and therefore there is no *a priori* contribution.

The vertical resolution for both grids is similar up to 85 km altitude (Fig. 3.12). Above this height the coarse grid incorporates more points from the fine grid, and thus, the vertical resolution decreases. The values of the vertical resolution (Fig. 3.12) of the two highest points for the coarse grid are 10 km at 100 km and 8 km at 110 km. However, the corresponding total uncertainties at these altitudes is above 100% and 60%, therefore we do not consider them to contribute to the retrieval.

Figure 3.13a shows the temperature retrieval calculated using the OEM, with and without the *a priori*. The two retrievals are identical up to 88 km. After 88 km the coarse grid retrieval differs from the fine grid retrieval and provides 4 more levels to the retrieval. The last 2 levels are shown with dashed lines in Fig. 3.13a and are points that we would not consider in the retrieval due to their large uncertainties. The last valid point shown in Figure 3.13a is around 100 km, where the corresponding statistical uncertainty and systematic uncertainties due to the tie-on pressure and ozone cross section are 15, 9 and 2.3 K, respectively (Fig. 3.13b).
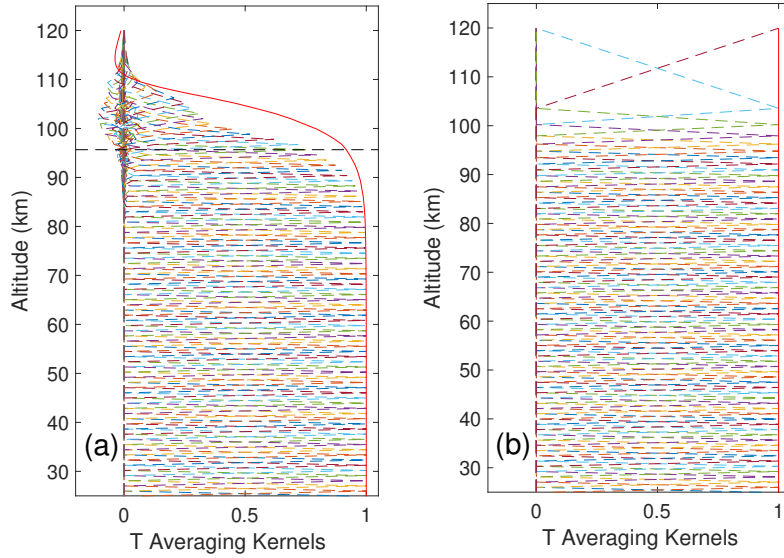
Figure 3.11: The PCL averaging kernels for the temperature retrieval on 12 May 2012 on the fine grid (a) and on the coarse grid (b). The **Au** = 0.9 cutoff height on the fine grid is shown by the black horizontal dashed line at 97 km. The red lines on the edges of the averaging kernels are the measurement response. The coarse grid extends the temperature upwards by 4 km.

Therefore, the last valid point of the retrieved temperature on the fine grid is within the total uncertainty of the coarse grid and the final retrieval altitude increases by 4 km.

A consequence of applying this method is that the uncertainties in the retrieval increase where the coarse grid is not equal to the fine grid. Figure 3.13b shows the statistical uncertainty on the fine and coarse grid, as well as two of the largest systematic uncertainties, including the uncertainty in the retrieved temperature due to the tie-on pressure and ozone cross section. The most sensitive uncertainty parameter is the statistical uncertainty, which changes from 13 K to 20 K at 98 km. The details of the systematic uncertainties on the fine grid are discussed in Sica and Haefele (2015) and Jalali et al. (2018). The systematic uncertainties increase after *a priori* removal due to the gain matrix (Eq. 1.30) increasing after the regularization term is removed. In general, all uncertainties on the coarse grid (Fig. 3.13b) increase at higher altitudes, where contribution from the *a priori* starts. The increasing of the random uncertainties at the highest altitudes is due to decreasing photocounts from the
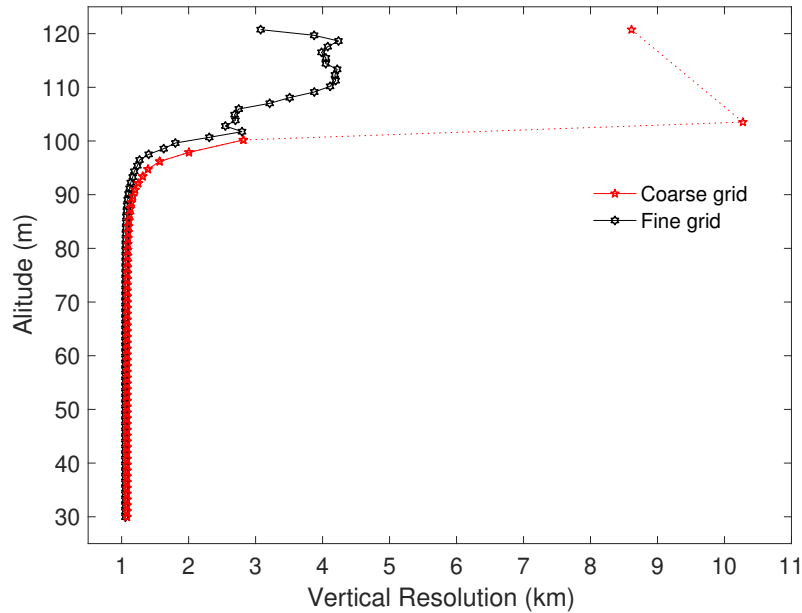
Figure 3.12: The PCL vertical resolution for 12 May 2012 on the fine and coarse grid. The vertical resolution is similar up to 85 km on both grids. Above this height the vertical resolution decreases until it is 10 km in resolution above 100 km altitude (dotted red line). We consider 100 km to be the highest meaningful point on the coarse grid due to large uncertainties above that height.

exponential decrease in air density.

To illustrate that the *a priori* is in fact being removed, we compared the temperature retrievals using two very different *a priori* temperature profiles, one calculated by CIRA-86 and one calculated by the US Standard Model (Fig. 3.14). The difference between the two temperatures on the fine grid retrieval is shown by the black curve and is about 2 K at the 0.9 cutoff line, within the statistical uncertainty. The difference increases rapidly above that height. The same temperature difference after the *a priori* is removed is shown in red and is on the order of zero at all altitudes.
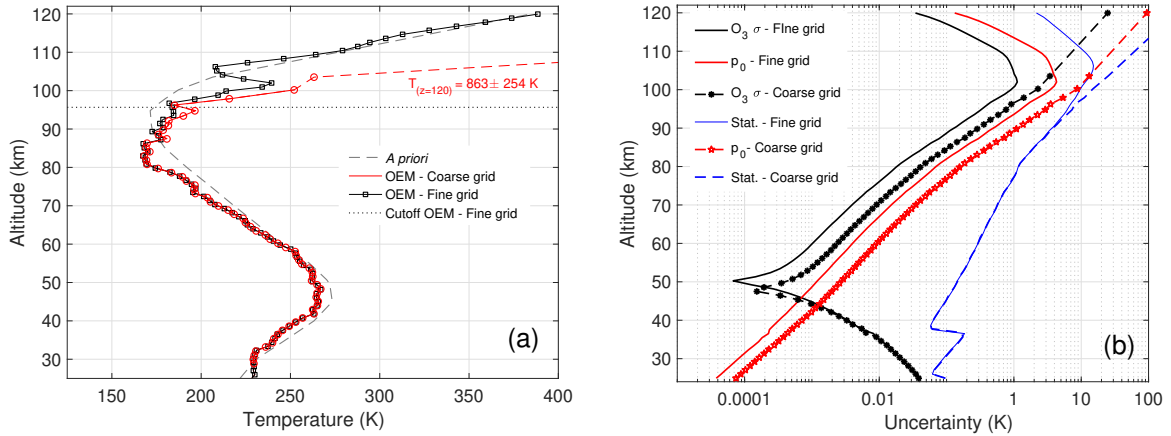
Figure 3.13: (a) PCL temperature retrieval for the fine and coarse grids on 12 May 2012. The temperature and its uncertainty for the last coarse grid point has a large value and it is not shown. (b) The statistical and systematic uncertainties due to the tie-on pressure and ozone cross section for the PCL temperature retrieval. The other systematic uncertainty terms included in our retrieval are not shown.

3.5 Discussion

We have developed a method to remove the influence of the *a priori* temperature and water vapour profiles on the retrieval based on the method discussed in Von Clarmann and Grabowski (2007). Von Clarmann and Grabowski (2007) presented a method to re-regularize the retrieval on a coarser grid after performing the OEM retrieval on a fine grid, effectively removing the *a priori* information from the retrieval. The method transformed the retrieved data from the "fine grid", or the initial retrieval grid, to a coarser grid in a way that the averaging kernel matrix on the coarse grid equals unity (that is, no *a priori* effect) at each vertical grid point.

Von Clarmann and Grabowski (2007) presented two approaches, a "staircase" representation, and a "triangular" representation, to transform the retrieval from the fine to the coarse grid. The cumulative trace of $\mathbf{A}$ shows the total degrees of freedom of the retrieval. In these representations, the cumulative trace of the averaging kernel matrix $\mathbf{A}$ as a function of altitude is calculated and is then interpolated to the coarse grid based on the centered information approach. As each space contains only one degree of freedom, the spaces are
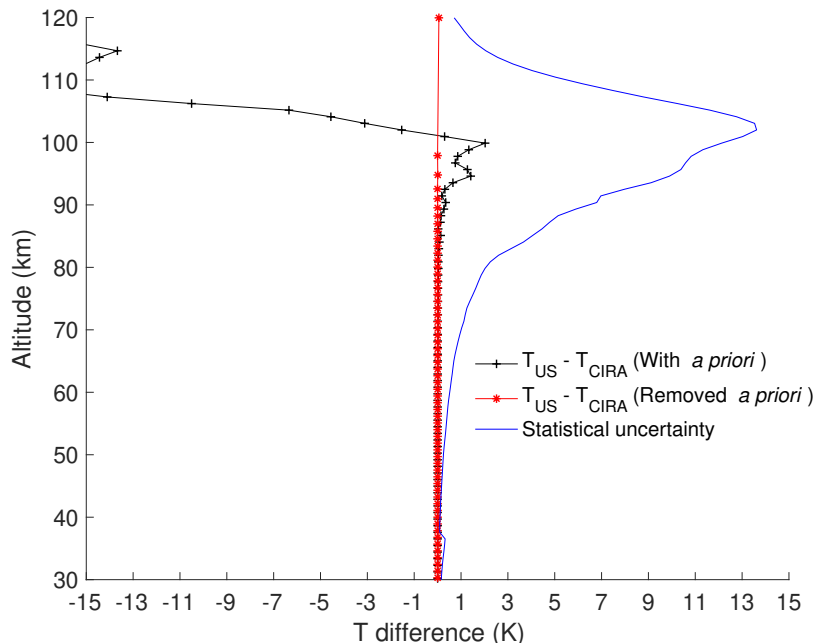
Figure 3.14: PCL temperature difference between the OEM retrieved temperature profiles using values from the US Standard Atmosphere and CIRA-86 as the *a priori*.

distributed irregularly. The staircase representation is not a realistic representation of the atmosphere (Von Clarmann and Grabowski, 2007), therefore we use the triangular representation here to create the coarse grid. In the triangular representation, the highest and lowest level of the coarse grid are considered to be the same as the fine grid and the rest of the grid points are distributed such that each element of **A** at each level is close to one.

Our method differs from Von Clarmann and Grabowski (2007) in that we do not re-regularize the retrieval to remove the *a priori*. Instead, after the initial retrieval, we remove the regularization term from the retrieval and re-run the retrieval using the triangular coarse grid. Both methods are equally effective, however, this method is more of a brute-force technique but easier to practically implement.

We have shown how the *a priori* removal method works for three sample retrievals: water vapor during both daytime and nighttime, and a nighttime Rayleigh temperature. The *a priori* removal technique is most useful when the SNR is low, particularly in dry layers. The method increased the retrieval altitude by roughly 2 km which is highly beneficial for me-

teorological studies that rely on accurate tropospheric measurements. The nighttime water vapor retrieval was provided for contrast to illustrate how the *a priori* removal technique does not provide significantly more information when the signal level falls off rapidly. However, the method did improve the difference between the radiosonde and the retrieval in the dry layer regions. The signal in the upper troposphere is significantly weaker and as such there is no measurement information left with which to increase the retrieval altitudes.

For Rayleigh temperature retrievals, we used measurements from the PCL in London, Ontario. Jalali et al. (2018) suggested that the 0.9 level be used as the valid cut-off height. In the case of the PCL, we see that the second to last point on the coarse grid has a vertical resolution not much larger than the fine grid retrieval (Fig. 3.12) and is very close to the same height; therefore, the 0.9 measurement response value seems to be a conservative choice for a valid cutoff. We also showed that the effect of the *a priori* is removed completely in the Rayleigh temperature retrieval when we compared the differences in the retrieved temperature using the values from CIRA-86 and from the US Standard Model as the *a priori* profiles (Fig. 3.14). The presented method provides us with higher altitudes for the retrieved temperature profiles. Additionally, where the retrieved temperature profile in the coarse grid is the same as it is for the fine grid, we can be confident the temperature retrieval has a negligible contribution from the chosen *a priori* temperature profile.

An advantage of our method is that the entire coarse grid profile is valid, in the sense that the regularization term does not contribute to the retrieval. In regions where the SNR is low or the averaging kernel is significantly less than 1, the *a priori* removal method improves the validity of the retrieval. However, the systematic and statistical uncertainties in the retrieval increase due to the removal of the inverse of the *a priori* covariance matrix from the gain equation (Eq. 1.30). The vertical resolution of the profile also increases as a consequence of the method. While the *a priori* removal gives us more confidence in the retrieval, we may not consider the entire profile meaningful due to high uncertainties. Hence, the last few points with unity averaging kernel value on the coarse grid may not be recognized as valid retrieval levels.

3.6   Summary

We have developed a practical and robust method which removes the effect of *a priori* information in lidar OEM retrievals. The method utilizes an information-centered coarse grid which is derived using the averaging kernels from the initial "fine grid" retrieval. The resulting coarse grid is then used, in addition with setting the inverse of the *a priori* covariance matrix to zero, to create the final retrieval without any *a priori* information. The method has little computational cost; the OEM retrieval is extremely fast even on a laptop computer, so having to do the retrieval twice for each profile is not critical. We illustrated the method using a simple example in Sect. 3.3 and demonstrated the removal method using the water vapour signal from the RALMO and the Rayleigh temperature signal from the PCL. We summarize the results from both of these examples as follows:

1. Figure 3.1b) shows that 90% of the nights in the temperature climatology from Jalali et al. (2018) had less than a $5\,\mathrm{K}$ influence from the *a priori* temperature profiles at the $\mathbf{Au} = 0.9$ cutoff height. Additionally, in all cases the *a priori* temperature influence was less than the statistical uncertainty, as was illustrated in Fig. 6 in Jalali et al. (2018). Although small, the *a priori* temperature profile does contribute to the retrieved temperature in regions where the measurement response is smaller than 1.

2. The daytime water vapor *a priori* removal showed better agreement between the OEM coarse grid retrieval and radiosonde by up to 50% in regions where the fine grid measurement response was smaller than 0.9. Using this method helped to increase the altitude range of the daytime and nighttime water vapor retrievals by up to $2\,\mathrm{km}$ and $600\,\mathrm{m}$, respectively. The nighttime water vapor *a priori* removal does not show large differences with the fine grid retrieval, but does show differences in dry regions with low signal. The difference in improvement between the daytime and nighttime retrievals is due to the difference in SNR of the RALMO measurements.

3. Applying the method to the PCL temperature retrieval showed a gain in information above the $\mathbf{Au} = 0.9$ cutoff height by $2\,\mathrm{km}$, validating the choice of $\mathbf{Au} = 0.9$ for a cutoff made in Jalali et al. (2018) to form their climatology up to an altitude where tie-on

pressure effects were minimal. The temperatures below the cutoff height were the same.

4. In all cases, the vertical resolution of the OEM retrieval decreases after *a priori* removal.

5. The systematic uncertainties after *a priori* removal increase roughly by a factor of 2, but remain on the same order of magnitude as before the *a priori* removal. The values of the systematic uncertainties also remain significantly smaller than the statistical uncertainties.

6. The temperature difference between the PCL retrieved temperature profiles using two different *a priori* profiles were used to show the efficiency of the *a priori* removal method. The temperature difference before removal around the 0.9 cutoff height was more than 2 K, however, this value was zero for the entire range after *a priori* removal.

3.7   Conclusions

A question that often arises from our colleagues when introduced to the OEM is: what is the effect of the *a priori* on the retrieval? This effect has been explored in detail for satellite-based and passive ground-based instruments, but not for the new area of applying OEM to active-sensing measurements such as lidar. Lidars are high resolution instruments with significant amounts of information available from their measurements, as evidenced by the retrieval averaging kernels. The OEM helps to illustrate the robustness of the lidar data products with the advantage of providing diagnostic tools, such as the averaging kernel and a full uncertainty budget.

Newcomers to the OEM may find this *a priori* removal technique helpful for checking their *a priori*'s influence on the retrieval and in determining the appropriate *a priori*. It is most useful for lidar measurements with low signal to noise and a slow transition from regions of high signal to low signal. The method is less effective when signal strength changes

rapidly, such as when the nighttime water vapour measurements quickly enter the dry upper troposphere or lower stratosphere.

Another advantage of this method is that the same coarse grid for a typical night can be used for multiple lidar retrievals. In some cases, the coarse grid will not be optimal but still reasonable. With this consistent grid choice, the altitude resolution of a multi-year time series will be consistent. Varying information content of the individual measurements will lead to error bars of different size. The coarse grid allows time series analysis or trend analysis for single altitudes without problems caused by varying altitude resolution.

In the future, this method will be applied to the entire 10 years of RALMO measurements to retrieve the water vapour day time and nighttime measurements and create a water vapour climatology. We anticipate that this technique will increase the altitude of the daytime water vapour retrievals by several kilometers. It is also our hope that this method may provide statistically significant measurements in the UTLS region. Finally, the RALMO water vapour climatology will be used to find trends.

Bibliography

Boersma, K. F., H. J. Eskes, and E. J. Brinksma. Error analysis for tropospheric no2 retrieval from space. *Journal of Geophysical Research: Atmospheres*, 109(D4), 2004.

Brocard, E, R Philipona, A Haefele, G Romanens, A Mueller, D Ruffieux, V Simeonov, and B Calpini. Raman Lidar for Meteorological Observations , RALMO - Part 2 : Validation of water vapor measurements. *Atmospheric Measurement Techniques*, 6:1347–1358, 2013. doi: 10.5194/amt-6-1347-2013.

Ceccherini, S., P. Raspollini, and B. Carli. Optimal use of the information provided by indirect measurements of atmospheric vertical profiles. *Opt. Express*, 17:4944–4958, 2009.

Cunnold, D. M., W.P. Chu, R.A.Barnes, M. P. McCormick, and R. E. Veiga. Validation of sage ii ozone measurements. *Journal of Geophysical Research: Atmospheres*, 94(D6): 8447–8460, 1989.

Dinoev, T, V. Simeonov, Y. Arshinov, S. Bobrovnikov, P Ristori, B Calpini, M Parlange, and H Van Den Bergh. Raman Lidar for Meteorological Observations , RALMO - Part 1 : Instrument description. *Atmospheric Measurement Techniques*, 6:1329–1346, 2013. doi: 10.5194/amt-6-1329-2013.

Jalali, A., R. J. Sica, and A. Haefele. A middle latitude rayleigh-scatter lidar temperature climatology determined using an optimal estimation method. *Atmospheric Measurement Techniques Discussions*, 2018:6043–6058, 2018. doi: 10.5194/amt-11-6043-2018.

Joiner, J. and A. Da Silva. Efficient methods to assimilate remotely sensed data based on information content. *Q. J. Roy. Meteor. Soc.*, 124:1669–1694, 1998.

NASA, . U.s. standard atmosphere. *US Government Printing Office*, (1976):1–227, 1976. doi: NASA-TM-X-74335,NOAA-S/T-76-1562.

Povey, A. C., R. G. Grainger, D. M. Peters, and J. L. Agnew. Retrieval of aerosol backscatter, extinction, and lidar ratio from raman lidar with optimal estimation. *Atmospheric Measurement Techniques*, 7(3):757–776, 2014. doi: 10.5194/amt-7-757-2014.

Rodgers, C D. Retrieval of atmospheric temperature and composition from remote measurements of thermal radiation. *Rev. Geophys.*, 14:609–624, 1976.

Rodgers, C D. *Inverse Methods for Atmospheric Sounding: Theory and Practice*, volume 2. World Scientific, Hackensack, NJ, USA, 2011.

Sica, R J and A Haefele. Retrieval of temperature from a multiple-channel Rayleigh-scatter lidar using an optimal estimation method. *Appl. Optics*, 54(8):1872–1889, 2015.

Sica, R. J. and A Haefele. Retrieval of water vapor mixing ratio from a multiple channel Raman-scatter lidar using an optimal estimation method. *Appl. Optics*, 55(4):763–777, 2016.

Vincent, R. A., A. Dudhia, and L. J. Ventress. Vertical level selection for temperature and trace gas profile retrievals using IASI. *Atmos. CMeas. Tech.*, 8:2359–2369, 2015.

Von Clarmann, T. and U. Grabowski. Elimination of hidden a priori information from remotely sensed profile data. *Atmos. Chem. Phys.*, 7:397–408, 2007.

Chapter 4

Intercomparison of Temperature Retrievals from Two Coincidentally Located Lidars Using Averaging Kernels

4.1 Introduction

Remote sensing instruments like lidars from the surface and satellites from the sky are used to measure atmospheric states. Different methods have been used to derive temperatures from remote sounder measurements, one of which is the inversion technique. An Optimal Estimation Method (OEM) is a type of inversion technique which was recently applied to lidar measurements (Sica and Haefele, 2016, 2015). OEM has also successfully been applied to Rayleigh lidar temperature measurements to calculate the Purple Crow Lidar (PCL) temperature climatology (Jalali et al., 2018b). The OEM calculates the best estimate of atmospheric temperature using a combination of measurements and available prior knowledge of the atmospheric states (*a priori*). *A priori* information is typically taken from a model, and is used as a "first guess" approximation to the solution, but its effect can be completely removed if desired (Jalali et al., 2018a). In order to validate remote sensing instruments, it is necessary to compare their measurements to others sources. Many studies have been done to compare temperatures measured by satellite instruments like the Aura Microwave Limb

Sounder (MLS) and the Sounding of the Atmosphere using Broadband Emission Radiometry (SABER) to lidar retrieved temperatures (Wu et al., 2003; Randel et al., 2004; Sica et al., 2008; Wing et al., 2018).

Rayleigh lidar temperature statistical uncertainties typically increase with altitude due to decreasing signal-to-noise ratios. Lidars co-add the signal in time (minutes to hours) and altitude in order to retrieve the temperature to higher altitudes while satellites make near instanenous measurements from a platform moving at $7000\,\text{m/s}$ over or near a lidar location. These differences in atmospheric sampling mean comparisons between instruments often must account for potentially large spatial-temporal ambiguities. However, direct comparisons can be improved by using an OEM diagnostic tool called averaging kernels, also known as weighting functions, which improve the ability to sample the measurement from one instrument as "seen" by another instrument.

The goal of this paper is to show the advantages of the OEM in the Rayleigh lidar temperature retrieval when comparing two lidars to each other and to other instruments such as satellites, radiosondes, and the United State's National Oceanographic and Atmospheric Administration (NOAA) National Center for Environmental Prediction (NCEP) reanalysis model. The NCEP reanalysis project is using a forecast system to perform data assimilation using past data from 1948 to the present. In Section 2 the basic concepts of the OEM retrieval and how to make comparisons using the OEM will be introduced. In Section 3 we will describe the properties of the lidars and the input measurements used for this study. Section 4 presents the results of the OEM retrieval for each individual lidar as well as the comparisons with other instruments. Sections 5 and 6 are the summary and conclusions, respectively.

4.2   Description of measurements used in this study

4.2.1   Lidar description

The NASA (National Aeronautics and Space Administration) Goddard Space Flight Center (GSFC) lidar system (henceforth referred to as the NASA lidar) is a mobile trailer lidar

which is designed primarily to measure stratospheric ozone. In addition, the NASA lidar is capable of measuring temperatures in the middle atmosphere from 30 to 80 km using Rayleigh scattering at 355 nm. The NASA lidar has 4 elastic channels (high and low gain at 308 and 355 nm) as well as N_2 Raman-scattered channels. The NASA elastic channels at 355 nm were used to retrieved the temperature. The NASA High Level Rayleigh (HLR) channel is typically used between 35 km and 80 km, whereas the NASA Low Level Rayleigh (LLR) channel is used below 35 km with a grey filter to reduce the photomultiplier nonlinearity. A grey filter is a neutral-density filter which reduces the intensity of backscatter signal at all wavelengths. Profiles are measured every minute with range bins of 150 m. The NASA lidar also receives the signals at 308 and 355 nm. The lidar signal at 308 nm is absorbed by ozone significantly, and the return signal at 355 nm is less sensitive to ozone absorption. These two channels signal can be used to retrieve ozone density (Leblanc et al., 2016). Detailed specifications of the lidar and previous validations of the NASA lidar temperature profiles are discussed in Ferrare et al. (1995), Singh et al. (1996) and Gross et al. (1997). After an upgrade in 1992 (McGee et al., 1993, 1995), nitrogen and water vapour vibrational Raman channels were added to the system at 332 nm and 387 nm, and 407 nm respectively. The Rayleigh channels are used for the temperature retrieval above 30 km where the effect of aerosols is typically negligible. Below 30 km, the Raman channel measures temperature down to 8 km. The complete description of the NASA lidar is reported in McGee et al. (1995). The NASA lidar is a portable lidar with he characteristics of measuring ozone and temperature profiles in the lower and middle atmosphere makes it suitable for inter-comparison campaigns with other lidars.

The German Weather Service lidar (henceforth, the DWD lidar) is located in Hohenpeisenberg, Germany at 47.8° N, 11.0°E and has been operated since 1987. The DWD lidar is an ozone DIAL lidar which measures an absorption signal at 308 nm and Rayleigh signal at 353 nm, similar to the NASA system. The DWD lidar has only one Rayleigh scatter channel and uses a grey filter 30 minutes after the sunset and 30 minutes before sunrise to reduce the photomultiplier saturation effect caused by high count rates. DWD temperature profiles typically range from 30 km to 70 km with raw range bins of 300 m below 80 km and 17 km above. The DWD lidar transmitted pulse energy at 353 nm is 10 mJ, the NASA lidar's

pulse energy at 355 nm is 150 mJ. Therefore, the return signal for the DWD lidar is several orders of magnitudes weaker than the NASA lidar. The details of schematic and properties of DWD lidar is described in Steinbrecht et al. (2009).

In the HC method procedure, the nonlinearity correction is applied to every profile and then integrated in time and height. However, in the OEM it is impossible to follow the same procedure as the HC method and the nonlinearity correction is applied to the nightly-integrated measurement profile inside the forward model. In order to get the most accurate results from the OEM, the nightly-integrated signal must be created from a set of profiles which follow a normal distribution.

All HC method results for the DWD and NASA lidar temperatures in this paper are identical to the results presented in Steinbrecht et al. (2009). The OEM uses the same raw photocount profiles, with the exception of DWD where we omit the scans that were affected by clouds or misalignment.Therefore, all signals for the DWD lidar were re-evaluated for the OEM temperature retrieval and all scans that were significantly different from the average profile were removed. These extraneous scans were likely caused by passing clouds over the lidar site, a misaligned laser, or high background signal.

The NASA lidar was brought to the DWD lidar location for an intercomparison campaign, called the Hohenpeisenberg Ozone Profiling Experiment (HOPE), in October 2005 for 13 nights. The temperature results were also compared with radiosondes and the NCEP reanalysis model. The results of the temperature inter-comparison revealed that the DWD temperature profiles have a 1 to 2 K cold bias from 30 to 65 km in comparison to the NASA temperature profiles and a 2-4 K against radiosonde and NCEP model (Steinbrecht et al., 2009). The campaign revealed a 290 m range error in the DWD altitudes as well as incorrect statistical uncertainty calculations which were off by a factor of 2.2 and the need for a better gravity model. After applying these improvements, the temperature difference between the DWD and NASA temperature profiles reached less than 1 K between 27 and 55 km. The other results relating to temperature reported in Steinbrecht et al. (2009) are:

1. Both lidars showed colder temperatures than the radiosonde temperature between 25 and 30 km as well as the NCEP temperature between 30 and 45 km.

2. The NASA lidar showed $1\,\mathrm{K}$ colder temperature than the radiosonde and NCEP analyses.

3. The average temperature difference between the DWD and NASA lidar is less than $1\,\mathrm{K}$ between 27 and $55\,\mathrm{km}$.

4. The NASA lidar temperature precision is less than $1\,\mathrm{K}$ between 20-50 km and less than $3\,\mathrm{K}$ around $70\,\mathrm{km}$.

5. The DWD lidar temperature precision is less than $2\,\mathrm{K}$ between 30 to $50\,\mathrm{km}$ and $10\,\mathrm{K}$ around $70\,\mathrm{km}$.

4.2.2   Comparison methodology

The NASA LLR and HLR channels and DWD Rayleigh channel were used to retrieve temperature profiles from $25\,\mathrm{km}$ up to each lidar's maximum nightly range. The details of the OEM methodology is described in Sica and Haefele (2015). The DWD lidar used a vertical resolution of $1.5\,\mathrm{km}$ in the original intercomparison using the HC method; therefore we chose an OEM retrieval grid of $1.5\,\mathrm{km}$ for both lidars. The retrieval parameters for the NASA lidar are the temperature profile, the lidar constant, background values for each channel, as well as the dead time for the HLR channel. The dead time value used for the NASA HC result was used as an *a priori* dead time value. The DWD lidar has only one Rayleigh channel, therefore only the temperature profile, lidar constant and background were retrieved. The DWD lidar uses an empirical function to correct the nonlinearity due to photomultiplier saturation. Therefore, the empirical function was used as a model parameter and the systematic uncertainty due to the saturation was included in the final uncertainty budget. The CIRA-86 model atmosphere was chosen as the temperature *a priori* profile for both lidars.

In order to compare the OEM retrieved temperature profiles with other instruments, e.g. SABER and MLS, the averaging kernel matrix of the satellite measurements can be used to improve the comparisons. Using the averaging kernels helps to consider the different height resolutions as well. The temperature profile that the lidar would measure if it was looking through the same atmosphere as MLS can be calculated with an independent measurement

of an atmospheric temperature state ($\hat{\mathbf{x}}$) assuming the true temperature profile is in the state given by $\mathbf{x}$ and the combination of the lidar averaging kernel ($\mathbf{A}$) and the lidar *a priori* temperature profile ($\mathbf{x_a}$) according to

$$\hat{\mathbf{x}} = \mathbf{A}(\mathbf{x} - \mathbf{x_a}) + \mathbf{x_a}. \tag{4.1}$$

When comparing two lidar temperature profiles or a lidar profile with a satellite profile using averaging kernels, we should decrease the temperature profile resolution of an instrument with higher degrees of freedom (henceforth called the degraded profile). When comparing DWD and NASA lidar temperatures, the NASA lidar temperature profile has the measurement with higher degrees of freedom. When comparing lidar measurements with satellites, the lidar measurements typically have higher degrees of freedom. The following relation is the same as Eq. 4.1 but rewritten in the more details for the case of applying Eq. 4.1 to the DWD and NASA lidar comparison.

$$\mathbf{T_{NASA-degraded}} = \mathbf{A_{DWD}} \times (\mathbf{T_{NASA}} - \mathbf{Ta_{DWD}}) + \mathbf{Ta_{DWD}}. \tag{4.2}$$

where $\mathbf{A_{DWD}}$ is the averaging kernel matrix of the DWD lidar and $\mathbf{T_{NASA-degraded}}$ is the degraded NASA temperature profile which is what the NASA lidar would see if it was looking through the same atmosphere with the same instrumentation as DWD.

The OEM has several advantages over the HC method. Unlike the HC method, which included estimates of random uncertainty, the OEM produces a complete uncertainty budget for all effective parameters in the retrieval procedure.

4.3   Results

4.3.1   The NASA and DWD OEM temperature retrievals

This section will discuss the results of the OEM temperature retrievals for both lidars. Figure 4.1 shows a typical OEM temperature profile for the NASA (Fig. 4.1a) and DWD (Fig. 4.1b) lidars and compares it with the HC method. The example night used here is 29 October 2005. For both lidars, the OEM and HC methods show very good agreement. The NASA OEM
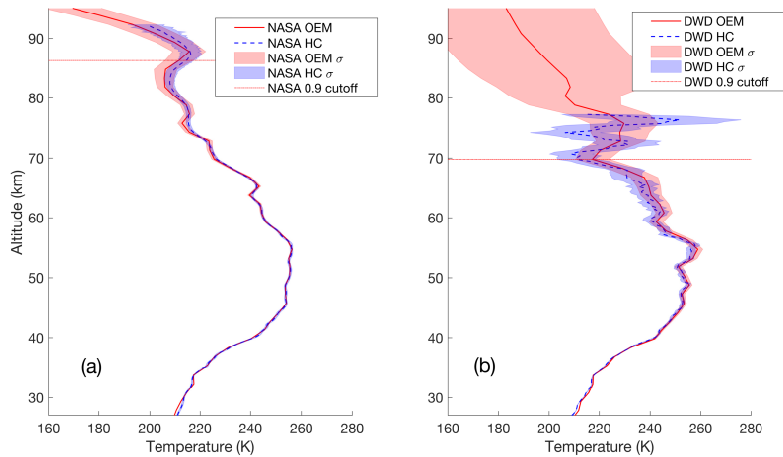
Figure 4.1: Temperature retrieval using the OEM on 29 October 2005 from a) NASA lidar measurements and b) DWD lidar measurements. The blue and red shaded area is the statistical uncertainty of the HC method and OEM, respectively.

temperature retrieval lies on the HC temperature completely up to 80 km, above 80 km there is slightly difference between them but the difference is inside their statistical uncertainty. The DWD OEM temperature profile agrees with HC up to 55 km, the HC temperature is slightly colder than the OEM above 50 km up to 70 km however they are inside their each others statistical uncertainty. The DWD HC temperature has a large fluctuations above 70 km.

Using the measurement response, we calculated the cutoff height for each lidar throughout the campaign (Fig. 4.2). We compared the cutoff heights for both lidars at the altitudes where **Au** was 0.9. We show the 0.8 cutoff line to highlight the differences in the retrieval when we compare with other lidars or satellite instruments using the averaging kernel. The average 0.9 cutoff altitude for the DWD and NASA lidars is at 70 and 87 km, respectively. These altitudes are roughly 10 km higher than the cutoff altitude of the HC retrieved temperature. The 0.8 cutoff line is almost 7 km higher than the 0.9 cutoff. Figure 4.3 shows the averaging kernels of the OEM temperature retrievals on 29 October 2005 for the NASA and DWD lidars. The NASA lidar's typical return signal is several orders of magnitude larger than the DWD lidar and this difference is visible in the averaging kernels. The NASA averaging kernels (Fig. 4.3a) are almost 1 up to 70 km and then they drop to 0.9 around 86 km. However, the
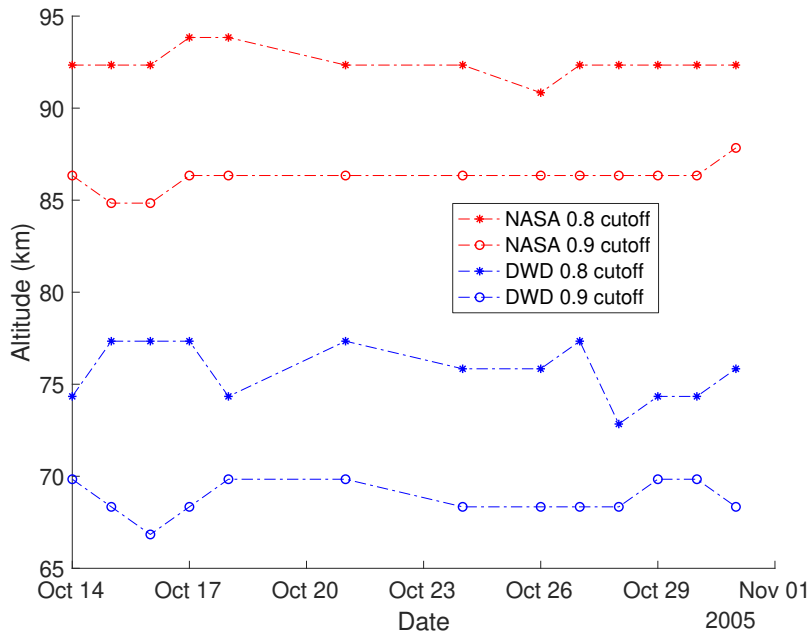
Figure 4.2: The OEM temperature cutoff heights for the NASA and DWD lidars for the entire HOPE campaign. The average 0.9 cutoff height for NASA is at 87 km, while the average 0.9 cutoff height for DWD is at 70 km.

DWD averaging kernels are unity up to 50 km and 0.9 value is around 70 km.

Both DWD and NASA HC algorithms used a boxcar averaging function to decrease their vertical resolutions and thereby increase their signal-to-noise ratios (SNR) and reduce the photon count noise. The DWD lidar used a fixed 5 point boxcar for all altitudes to create 1.5 km vertical resolution. The NASA lidar also used a boxcar average but with a variable width to make the vertical resolution less than 2 km for all altitudes below 60 km. After 60 km, the vertical resolution increases by 1 km for every 5 km in altitude. The NASA vertical resolution reaches 6 km at 80 km and after 80 km is constant at 7 km vertical resolution.

The OEM provides the vertical resolution using the full width at half maximum of the averaging kernels at each altitude. The OEM uses a 1.5 km retrieval grid for both lidars. Figure. 4.4 shows the vertical resolution for NASA and DWD lidar using the HC method and OEM, as well as the vertical resolutions for SABER and MLS temperature profiles. The OEM vertical resolution for DWD lidar is 1.5 km up to 60 km and above that increases to 3 km at 80 km. The vertical resolution values for the NASA OEM temperature retrieval
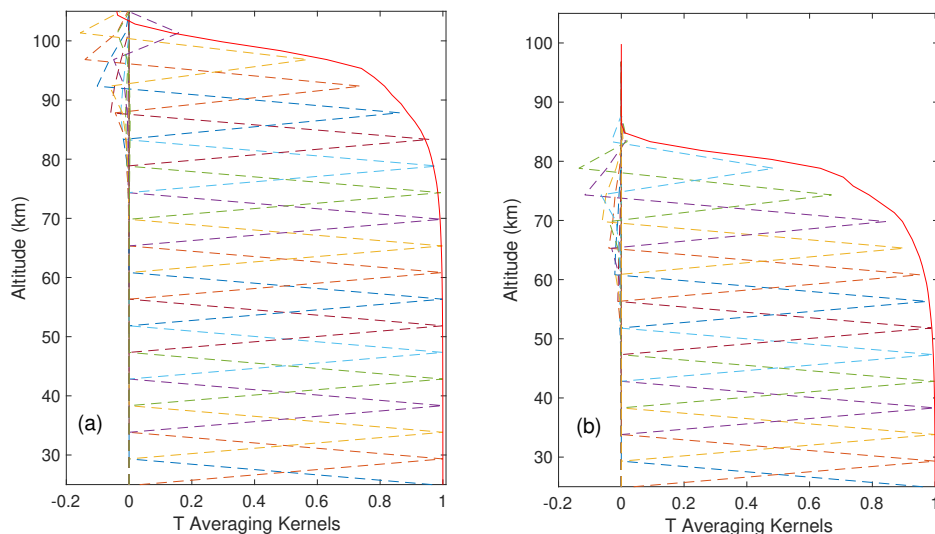
Figure 4.3: Temperature averaging kernels for the OEM temperature retrieval on 29 October 2005 for a) NASA lidar measurements and b) DWD lidar measurements. The NASA averaging kernels are larger and do not decrease as rapidly as the DWD averaging kernels due to the NASA lidar's higher energy per pulse and larger telescope diameter.

are $1.5\,\mathrm{km}$ until $80\,\mathrm{km}$ altitude, where it increases up to $4\,\mathrm{km}$ at $100\,\mathrm{km}$ altitude. SABER's vertical resolution is $2\,\mathrm{km}$ for all altitudes. However, MLS's resolution is much larger than the others, with a maximum of $10\,\mathrm{km}$ at $55\,\mathrm{km}$ and at $98\,\mathrm{km}$.

Figures 4.5a and 4.5b illustrate the statistical uncertainty and all systematic uncertainties larger than $0.001\,\mathrm{K}$ for the NASA and DWD temperature retrievals on 29 October 2005. Table 4.1 summarizes the uncertainties from Fig. 4.5 for every $10\,\mathrm{km}$ in altitude between 30 and $80\,\mathrm{km}$. To be consistent and compare with the NASA lidar's uncertainties at $80\,\mathrm{km}$, we have also included the DWD lidar uncertainties. However, $80\,\mathrm{km}$ is several km above the DWD 0.9 cutoff height. The statistical uncertainties for the DWD lidar are around $1\,\mathrm{K}$ at $50\,\mathrm{km}$ but quickly increase to $2.9\,\mathrm{K}$ at $60\,\mathrm{km}$ and finally $6\,\mathrm{K}$ at $70\,\mathrm{km}$. However, Steinbrecht et al. (2009) mentioned that the statistical uncertainty for the DWD lidar at $70\,\mathrm{km}$ is around $10\,\mathrm{K}$. For the NASA lidar, the statistical uncertainty is less than $1\,\mathrm{K}$ below $70\,\mathrm{km}$ and is around $2\,\mathrm{K}$ at $80\,\mathrm{km}$ which is consistent with Steinbrecht et al. (2009). The temperature uncertainty due to the tie-on pressure (p_0) for the DWD lidar is around
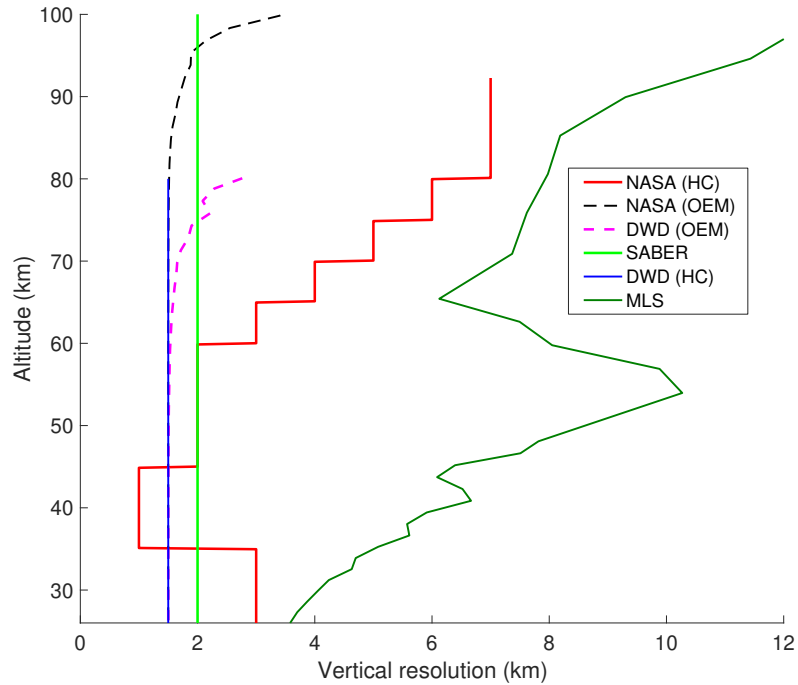
Figure 4.4: The vertical resolutions for the NASA and DWD lidar temperature retrievals using the OEM and HC method, as well as the SABER and MLS satellites.

0.1 to 1.7 K between 50 and 70 km and below 50 km is on the order of 0.01 K. However, the uncertainty due to the tie-on pressure for the NASA lidar is small for all heights and reaches a maximum of 0.14 K at 80 km.

The temperature uncertainty due to the uncertainty in the Rayleigh scatter cross section for the DWD lidar is less than 0.1 K below 50 km and its maximum is 1.1 K at 70 km. The values of the uncertainty due to the Rayleigh scatter cross section for the NASA lidar is less than 0.1 K below 60 km and is around 0.8 K at 80 km. The interesting point is that the temperature uncertainty due to the Rayleigh scatter cross section is more than the uncertainty due to the tie-on pressure for NASA lidar. The reason is that the Rayleigh scattering cross section is proportional to the quarter of wavelength inversely (Nicolet, 1984) and also, the signal in the NASA lidar is several orders of magnitude stronger than the DWD lidar and the tie-on pressure smaller. The temperature uncertainty due to gravity is identical for both lidars. The temperature uncertainty due to the uncertainty in the air number density
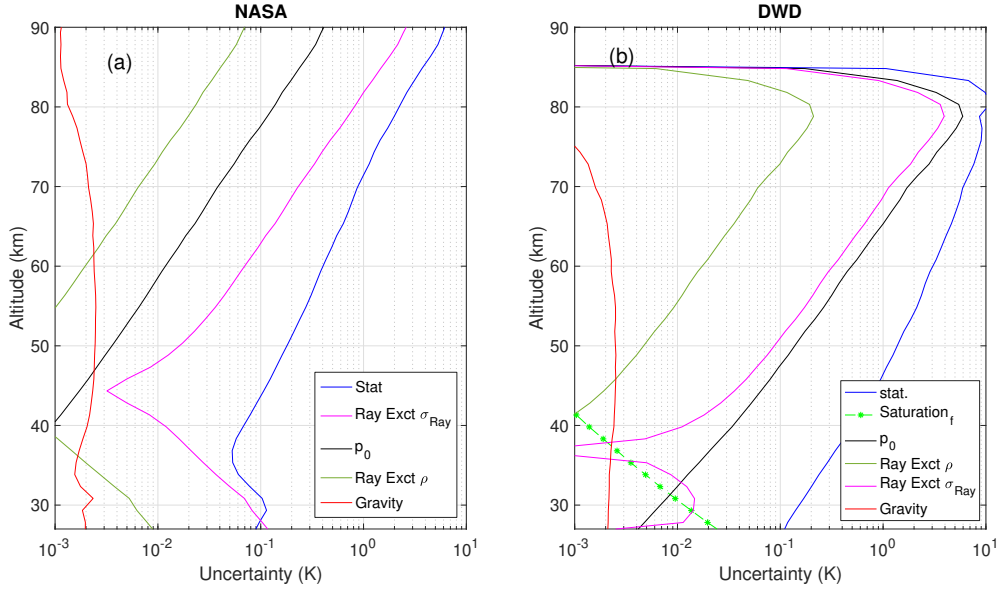
Figure 4.5: Temperature uncertainties due to the parameters inside the forward model greater than $0.001\,\mathrm{K}$ on 29 October 2005 for a) NASA lidar measurements b) DWD lidar measurements.

is at least one order of magnitude smaller than the other systematic uncertainties shown in Table 4.1 except the gravity.

The last systematic uncertainty, which only applies to the DWD lidar, is the uncertainty due to the empirical saturation function. It has a maximum contribution of $0.04\,\mathrm{K}$ at $25\,\mathrm{km}$ and decreases with height to reach a minimum of 0.001 at $40\,\mathrm{km}$.

4.3.2 Comparison of the average temperature differences between instruments

In this section we will compare the average temperature profiles from the NASA and DWD lidars. We will compare the results using three average temperature profiles which were created using three measurement techniques: the HC method and the OEM method to compare the measurements directly together, and using the averaging kernels from the OEM retrievals to compare two profiles using Eq. 4.1. The average temperature differences between the two lidars using all methods are plotted in Fig. 4.6. The average temperature differences

Table 4.1: Statistical and systematic uncertainties greater than 0.001 K of the OEM temperature retrieval for the DWD and NASA lidars on the 29 October 2005. This is a summary of Fig. 4.5.

Uncertainties	30 km	40 km	50 km	60 km	70 km	80 km
Stat. DWD	0.15	0.5	1.3	2.9	6.0	10.5
Stat. NASA	0.11	0.06	0.18	0.4	0.8	2.2
Press. DWD	0.007	0.03	0.14	0.45	1.7	5.4
Press. NASA	< 0.001	< 0.001	0.003	0.01	0.03	0.14
Ray. ext.$_\sigma$ DWD	0.01	0.01	0.09	0.3	1.1	3.5
Ray. ext.$_\sigma$ NASA	0.09	0.01	0.01	0.06	0.2	0.8
Ray. ext.$_\rho$ DWD	< 0.001	< 0.001	0.004	0.015	0.06	0.19
Ray. ext.$_\rho$ NASA	0.006	< 0.001	< 0.001	0.002	0.006	0.02
Gravity DWD	0.002	0.002	0.002	0.002	0.002	< 0.001
Gravity NASA	0.002	0.002	0.002	0.002	0.002	0.001
Saturation fun. DWD	0.014	0.001	< 0.001	< 0.001	< 0.001	< 0.001

between the DWD and NASA using the OEM is less than 1 K between 25 and 63 km, then increases up to 3.2 K around 67 km and at 70 km is 2 K. If we considered the altitude where the measurement response is 0.8 as a valid cutoff height, the temperature differences between the lidars using the OEM at 75 km is 8 K. However, the conservative cutoff height where the measurement response is 0.9 which shows a difference in OEM profiles of 2 K at 70 km and a difference of -1 K at 70 km using the HC method. If we use the averaging kernel of the DWD lidar to degrade the NASA temperature profiles, the average temperature difference remains similar to the differences using the OEM where the averaging kernels of DWD are close to 1 (below 58 km). Degrading the NASA profile improves the differences between the NASA and DWD temperatures by up to 0.8 K between 58 and 70 km. If we were to consider the DWD temperature profiles valid up to 75 km, the degraded OEM improves the temperature by 2 K at 75 km. The only region that the degraded OEM does not provide better results is between 58 and 62 km where the temperature differences increase by 0.2 K when using the degraded NASA OEM. The black dashed lines show one standard deviation
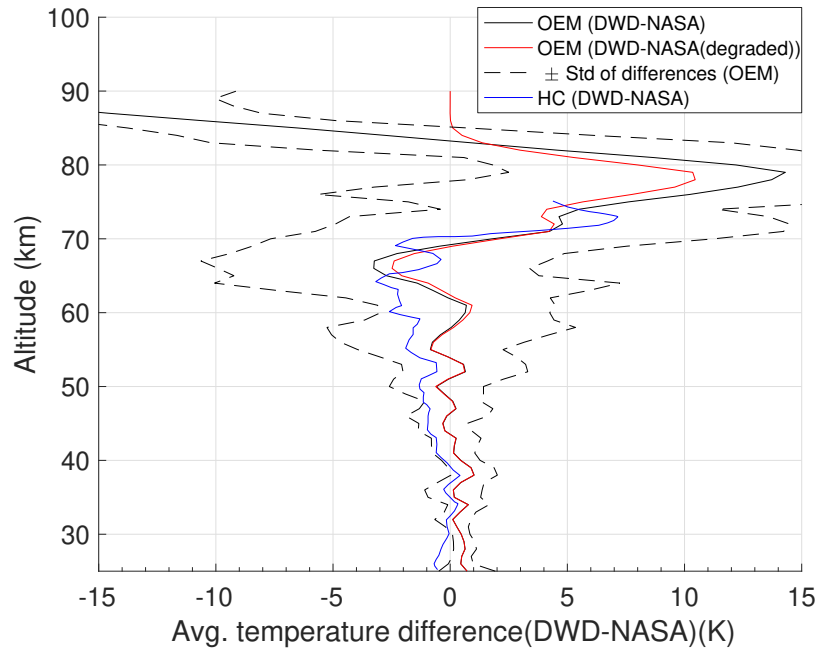
Figure 4.6: The average temperature difference between the DWD and NASA temperature profiles using the HC method, OEM and degraded OEM. The standard deviation of the average differences using the non-degraded OEM is in dashed black lines.

of OEM temperature differences between the lidars. The temperature difference using the HC method in Fig. 4.6 is less than 1 K between 25 and 48 km, and it increases up to -3 K at 65 km.

4.3.3 Comments on the differences in temperature measured by NASA and DWD

The average temperature difference profiles between the lidars and the Munich radiosondes are shown in Fig. 4.7. The temperature differences between the average NASA lidar HC temperature profile is 0.2 K closer to the average radiosonde profile between 25 km and 29 km. However, above 29 km, the OEM improves the difference by almost 0.4 K. The DWD average OEM temperature profile is 0.7 K closer to the radiosonde average profile compared to the average HC temperature profile. At this altitude, the effects of ozone on the temperature is less than 0.01 K, therefore the differences between the lidar average temperature profiles and
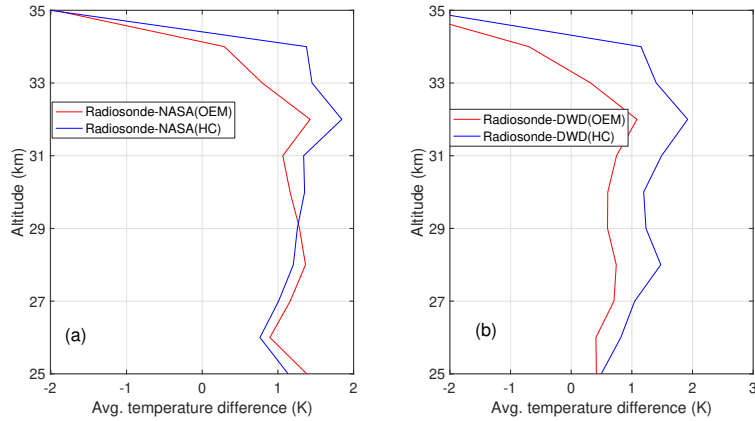
Figure 4.7: The temperature difference between the average radiosonde temperature profiles and the average (a) NASA and (b) DWD lidar temperatures.

radiosonde must be due to the nonlinearity correction. The DWD lidar OEM temperature retrievals are closer to the radiosonde profiles than the HC temperature profiles. The reason could be due to this fact that the influence of empirical saturation function is dominant between 25 to 30 km and the OEM applies the nonlinearity correction function to the average photocount profile, however the HC method applies the correction to each scan.

Figures 4.8a and 4.8b are the average temperature difference profiles between the OEM (red) and HC (blue) NASA and DWD lidars and the NCEP operational analyses. The NASA OEM temperature retrieval shows 0.2 K improvement between 25 and 32 km altitude. There is almost no difference between the temperature profiles produced by the OEM and HC techniques between 32 and 37 km. The OEM technique increases the difference between the lidar and NCEP model temperatures between 42 and 52 km. However, above 52 km the OEM improves the difference between the lidar and NCEP by an average of 0.5 K. The comparison between the NCEP temperature profiles and the DWD average temperature profiles revealed that the OEM temperature profiles are consistently warmer than the HC method. The OEM improves the differences between the lidar and the NCEP model below 42 km by an average of 0.5 K. However, above 42 km the absolute values of the differences between the lidar measurements and the NCEP model are the same, but the OEM temperatures are warmer than the DWD HC temperatures. The most likely cause of the temperature differences between the OEM and HC method for the DWD lidar is due to the fact that different scans

121
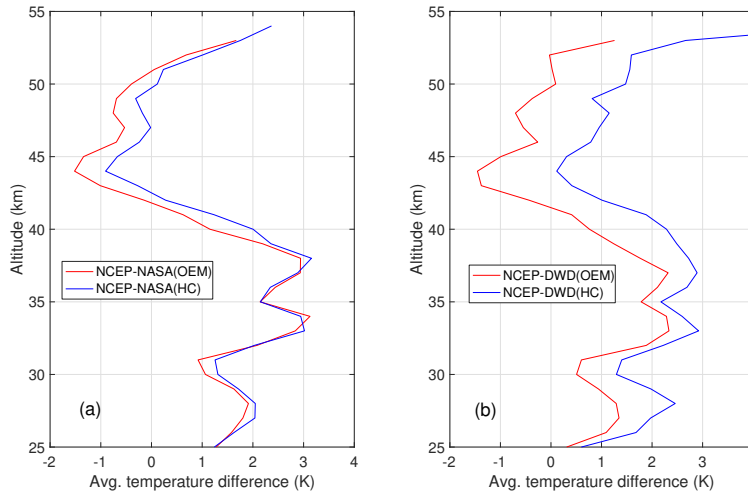
Figure 4.8: The average temperature difference between the NCEP temperature profiles and a) NASA lidar temperature profiles and b) DWD lidar temperature profiles.

that were used for the OEM retrieval. Over the 13 nights about 15% of the DWD lidar scans had significant variations from the nightly mean, principally due to clouds. We did not use these scan in the OEM analysis. DWD will reprocess their HC method temperatures using the same nights in the near future.

4.3.4 Comparing lidar and satellite temperature profiles

We now compare the OEM and HC retrieved temperature profiles from the DWD and NASA lidars to the temperatures measured by the MLS instrument on board the Aura satellite and SABER. The MLS uses OEM to retrieve temperature profiles therefore, it would be a good option to use its averaging kernels for comparison with lidars temperature profiles. The MLS temperature profiles were obtained from the version 4.2 retrievals. The MLS and SABER temperature profiles were chosen to be inside the region of $\pm 5°$ latitude (± 460 km) and $\pm 10°$ longitude (920 km) and coincident with the operating time of the lidars. The *a priori* temperature profiles for the MLS are the Goddard Earth Observing System (GEOS-5) model up to 1 mb and the CIRA-86 climatology above 1 mb (Schwartz et al., 2008). The averaging kernels of the MLS temperature profiles are only provided for the measurements taken at the equator and 70°N. The averaging kernels at latitudes close to these show very

small differences and are therefore not reported (Nathaniel J. Livesey, 2018). The degree of freedoms of MLS temperature profiles is 33 based on its averaging kernels. The NASA and DWD degrees of freedom are in average 48 and 36, respectively. Therefore, the lidars temperature profiles degraded using the MLS averaging kernels. In order to compare the temperature profiles between MLS and the DWD and NASA lidars, the MLS averaging kernels at 70°N were chosen to degrade the lidar temperature profiles by Eq. 4.1. Figure 4.9 shows the MLS averaging kernels used to degrade the lidar temperature profiles. The MLS averaging kernels for version 4.2 temperature retrieval are provided at the MLS website: https://mls.jpl.nasa.gov/data/ak/. Unlike the lidar averaging kernels, they never reach unity. Between 30 mb and 0.2 mb they are less than 0.4, however, between 0.2 mb and 0.01 mb they are between 0.6 and 0.8. The red line in Fig. 4.9 is the measurement response and represents the amount of contribution of the measurements in the temperature retrieval. The measurement response is calculated from summation of each row of the MLS averaging kernel matrix. The MLS measurement response is close to 1 at all levels except between 2 mb and 0.2 mb which there is a large fluctuation and changes from 0.9 to around 1.2 and this variation repeats again. The MLS vertical resolution corresponding the maximum width at half maximum of the MLS averaging kernels showed in Fig. 4.4. The MLS vertical resolution starts around 4 km at 25 km (28 mb) and increasing constantly to 10 km at 55 km (0.4 mb), then decreases again to 6 km at 65 km (0.09 mb) and then increases constantly again up to 10 km at 90 km (0.002 mb). At the lower pressure averaging kernels are larger, the vertical resolution at these levels is between 6 and 10 km.

To more accurately compare the MLS temperature profile with the lidar measurements, the average HC lidar temperature profile for 13 nights with the resolution decreased by applying the MLS averaging kernels (degraded profile) is calculated using the MLS averaging kernels (Fig. 4.10). Figure 4.10a shows the average NASA degraded temperature profile plotted up to 0.002 mb and the same is shown for the DWD lidar up to 0.01 mb in Fig. 4.10b. The shape of the average temperature profile for both lidars is very similar. There is good agreement between the lidars' average temperature profile and MLS's between 20 mb and 0.02 mb except between 4 and 1 mb, which coincides with the minimum in the MLS averaging kernels and where the measurement response changes rapidly. Also, NASA lidars'
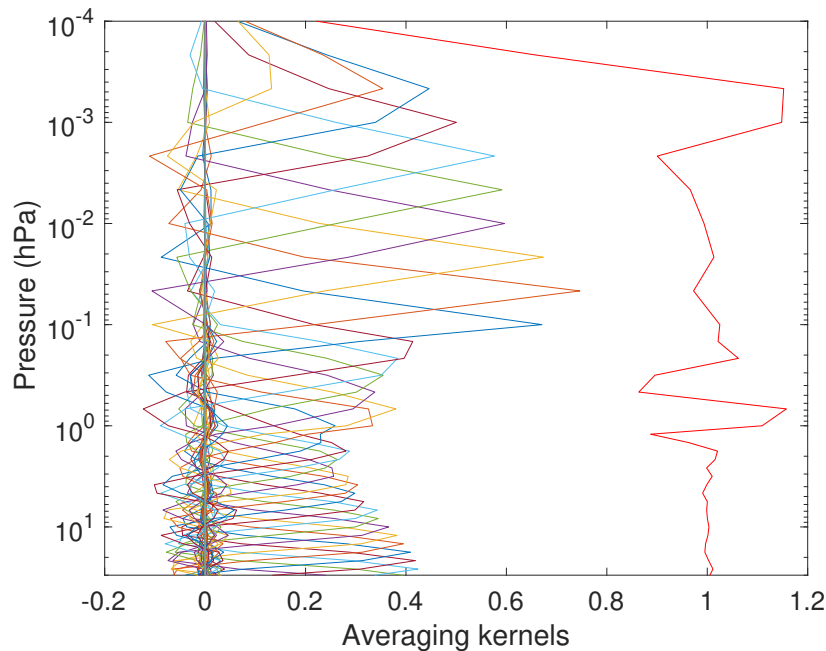
Figure 4.9: The MLS averaging kernels at 70°N. The red line represents the measurement response.

average temperature profiles in Fig. 4.10a shows a strong inversion layer between 0.03 mb and 0.001 mb that is not seen in the MLS average temperature profiles. However, this difference in temperatures may be due to fact that the lidar temperature profiles are retrieved over more than 6 hours of nightly measurements and the MLS temperature profiles are retrieved in less than 1 minute.

The MLS averaging kernels are much less than 1 at each level at low altitudes, however, the measurement response which is summation of each row of averaging kernels matrix is around 1. In order to see the effect of the MLS averaging kernels in the retrieved temperature profiles, two sample nights are chosen for direct comparison between the HC and MLS temperature profiles as well as using the degraded HC temperature profile by MLS averaging kernels and the MLS temperature profile (Fig. 4.11). In Fig. 4.11 a, the temperature difference between the lidar and MLS temperature profile is smaller than Fig. 4.11 b. There is a large jump in temperature difference in Fig. 4.11 b around 0.1 mb. The common feature in both cases is that the MLS averaging kernel makes the differences smoother. The average NASA degraded HC and HC temperatures between 12 mb and 0.5 mb (Fig. 4.12b) differ
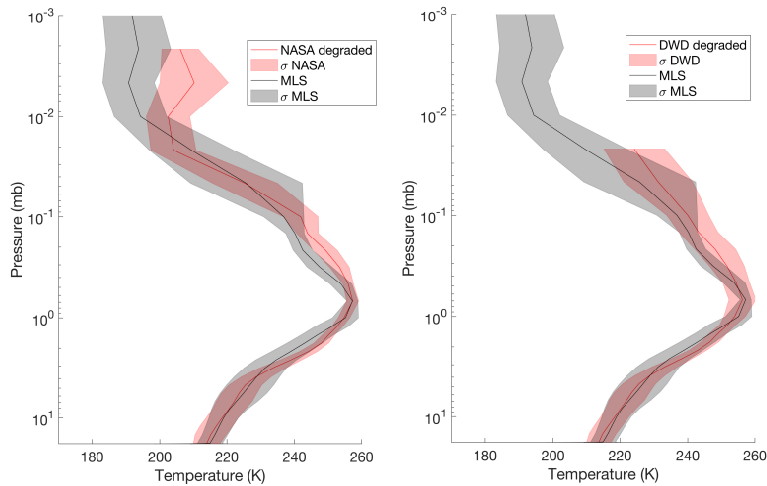
Figure 4.10: The average degraded HC temperature profile (red) for the NASA (a) and DWD (b) lidars and the MLS temperature profile (black) with corresponding temperature standard deviations (dotted lines).

from the MLS profile by less than $4\,\mathrm{K}$. Above the $0.2\,\mathrm{mb}$ pressure level and up to $0.02\,\mathrm{mb}$, where the MLS averaging kernels are larger, the degraded HC shows better agreement with the MLS temperature than the HC temperature by an average of $3\,\mathrm{K}$.

Figure 4.12b presents the same results as Fig. 4.12a, but for the DWD lidar. The average temperature difference between the MLS temperatures with the degraded OEM and HC temperatures behaves similarly to those discussed for the NASA lidar but only up to the $0.04\,\mathrm{mb}$ pressure level which is the maximum retrieval height for DWD.

The differences between the degraded OEM and satellite measurements were not shown because there were very little difference between the OEM and HC results. Possible reasons as to why the MLS and lidar average temperature profiles are not consistent with each other between 0.7 and $0.2\,\mathrm{mb}$ could be because of following reasons.

1. The lidars temperature profiles are averaged over 6 hours measurements, however, the MLS measurements are taken in less than 1 minute.

2. Tidal variability is large around 40 and $50\,\mathrm{km}$ (Baumgarten et al., 2018), which corresponds to the maximum temperature difference between the MLS and the lidar measurements.

Figure 4.11:   The temperature difference between the MLS temperature profile and the NASA temperature profile calculated by the degraded HC (red profiles) and the HC method (blue profile) for a) 20050527 b) 20050526.

3. The vertical resolution of the lidars is higher than the MLS and therefore more sensitive to geophysical variability than the MLS.

4. The averaging kernels of the MLS through the stratosphere and stratopause are very weak and could be the source of the temperature differences at lower altitudes.

5. There is a sharp change in the structure of the MLS averaging kernels around 0.2 mb and this variation could induce an artificial damping gradient in the retrieved MLS temperature profiles.

The Sounding of the Atmosphere using Broadband Radiometry (SABER; Mlynczak and Russell (1995)) has been operating on the Thermosphere Ionosphere Mesosphere Energetics and Dynamics (TIMED) satellite since 2001. The SABER temperature measurements are based on the kinetic temperature of CO_2 limb-emission radiance. The vertical resolution of the SABER is 2 km (Fig. 4.4) and is comparable with the lidar retrieval grids at 1.5 km. Therefore, it is useful to compare the retrieved lidar temperature profiles to the SABER measurements even though SABER doesn't use the OEM. The average temperature difference between the SABER and each lidar is shown in Fig. 4.13. The temperature differences for each lidar and the SABER average temperature profiles are within 3 K between 25 and 65 km
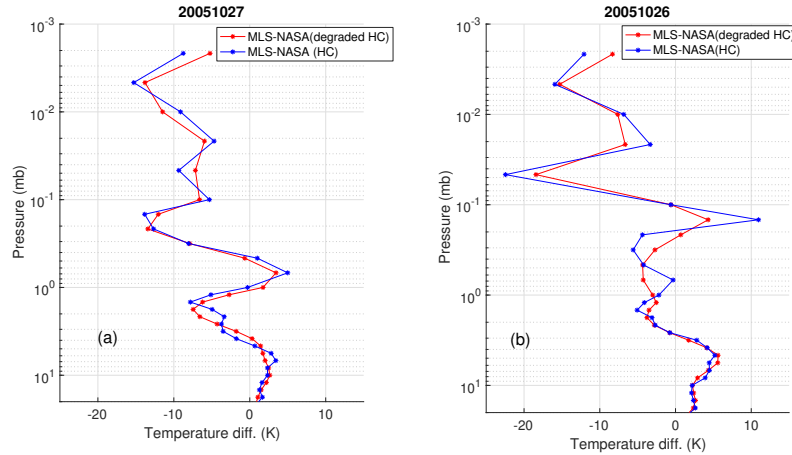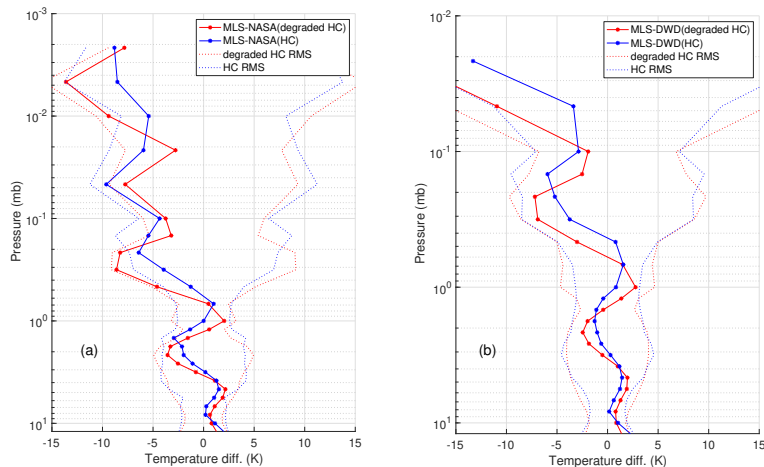
Figure 4.12: The average temperature difference between the average MLS temperature profiles and the lidar average temperature profiles calculated by the degrade HC (red profiles) and the HC method (blue profiles). The average temperature difference between the average MLS temperature profiles and a) the NASA degraded HC (red) and HC (blue) temperature profiles and b) the DWD degraded HC (red) and HC (blue) temperature profiles.

for both the OEM and HC method. Above 65 km up to 88 km the temperature differences between the SABER and NASA temperature profiles are between -3 and -7 K. The temperature difference between the SABER and DWD reaches almost 6 K at 70 km and above that increase rapidly. However, the DWD temperature profiles are not valid above 70 km.

4.4 Summary

The HOPE campaign of 2005 found the differences between the NASA and DWD lidar temperature algorithms and demonstrated they could be resolved. Here, we have used the OEM temperature retrieval to re-evaluate the comparisons between the DWD and NASA lidar temperature profiles after the corrections were made to the DWD HC retrievals. The results of our investigation using OEM temperature retrievals are summarized as follows:

1. The OEM uses the averaging kernels as a diagnostic tool to evaluate the contribution of the measurements on the temperature retrieval. The 0.9 and 0.8 cutoff heights were
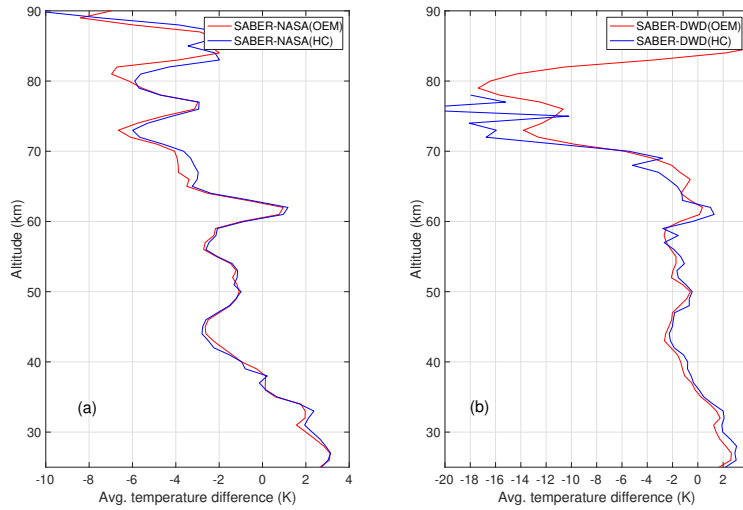
Figure 4.13:   The average temperature difference between the SABER temperature pro-
files and a) NASA lidar OEM and HC temperature profiles b) DWD lidar OEM and HC
temperature profiles

calculated using the measurement response function. If we consider the altitude at
which the measurement response is 0.9 as the cutoff height, the OEM increases the
validity of the temperature profile for both lidars by almost 10 km.

2. The averaging kernels of the OEM temperature retrieval for a sample night were pre-
sented for both lidars. Based on the measurement response function, the last altitude
where the measurements are 100% of the retrieval for the NASA and DWD lidars is
70 km and 48 km, respectively. Above these altitudes, the contribution of the lidar
measurements decreases.

3. The vertical resolution for the OEM temperature retrieval was calculated using each
lidar's averaging kernel matrix. The vertical resolution of both lidars using the OEM
are identical up to 65 km and above that are comparable.

4. The statistical uncertainty for the NASA lidar calculated by the OEM is same as the
HC method and is less than 1 K below 78 km. The DWD OEM statistical uncertainty
is 4 K smaller than the DWD HC method's at 70 km, which was reported by the HC
method 10 K at 70 km even with corrections.

128

5. The uncertainty budgets of both lidars were calculated for all uncertainties that are known to be on the order of $0.001\,\mathrm{K}$ (Sica and Haefele, 2015). The tie-on pressure uncertainty and Rayleigh cross section uncertainty on the Rayleigh extinction have the largest systematic uncertainties. The DWD lidar tie-on pressure uncertainty is higher than the Rayleigh cross section uncertainty, however, the NASA lidar's uncertainty budget shows the reverse due to the strong signal to noise ratio of the NASA lidar in higher latitudes. Also, the uncertainty of the DWD empirical saturation function was calculated to be $0.02\,\mathrm{K}$ at $25\,\mathrm{km}$.

6. The average temperature differences between the DWD and NASA temperature profiles were calculated using the OEM and degraded OEM and compared with the result from the HC method. The temperature difference between the lidars is less than $1\,\mathrm{K}$ between 25 and $65\,\mathrm{km}$ using the OEM and above that, the maximum difference is $3.2\,\mathrm{K}$ around $66\,\mathrm{km}$. The result for the HC method is less than $1\,\mathrm{K}$ between 25 and $47\,\mathrm{km}$ and it reaches to $3.2\,\mathrm{K}$ at $64\,\mathrm{km}$. Using the OEM and degrading the NASA lidar using the DWD averaging kernels improved the comparison above $60\,\mathrm{km}$, where the averaging kernels of the DWD start decreasing.

7. The temperature comparisons between the lidars' nightly OEM temperature profiles, the coincident radiosonde, and the NCEP model revealed that the OEM temperature retrieval is closer to the radiosonde and the NCEP model at all altitudes in comparison to the HC method.

8. The NASA and DWD average temperature profiles were compared to the MLS average temperature profiles. The MLS averaging kernels were used to degrade the lidars' temperature profiles. In the region where the averaging kernels were more than 0.7, the degraded OEM temperature profiles provided closer results to the MLS results around $3\,\mathrm{K}$.

9. The SABER temperature profiles were compared with the NASA and DWD temperature profiles. Below $54\,\mathrm{km}$ both SABER and MLS average temperature differences with lidars were within of $3\,\mathrm{K}$. Below $64\,\mathrm{km}$ ($0.1\,\mathrm{mb}$) the SABER temperature pro-

files were closer to the NASA and DWD temperature profiles by $3\,\mathrm{K}$, but above $64\,\mathrm{km}$ the MLS averaging kernels improved the comparison and the temperature difference between the MLS and NASA lidar was improved by $3\,\mathrm{K}$ up to $0.02\,\mathrm{mb}$.

4.5   Conclusions

We have shown that using the OEM retrieval temperature for Rayleigh-scatter lidar measurements can improve the intercomparison between lidars relative to traditional techniques. The extra information for each individual lidar includes the systematic uncertainties in addition to the statistical uncertainties. The DWD Rayleigh-scatter signal is more than 2 orders of magnitude smaller than the NASA lidar's signal. Considering this point, using the averaging kernel matrix revealed that the DWD temperature is valid up to $70\,\mathrm{km}$ and the NASA temperature is valid up to $87\,\mathrm{km}$ which is significantly higher than the altitudes shown in Steinbrecht et al. (2009). While these lidars were not designed primarily for temperature measurements, using OEM they can still reliably monitor the mesosphere.

The DWD lidar original vertical resolution was calculated using a fixed 5 point (1.5 km) boxcar average at all altitudes while NASA lidar used a variable width boxcar with widths less than 3 km below 65 km, increasing to 6 km above 75 km (Figure 5 of Steinbrecht et al. (2009)). The OEM provided the vertical resolution directly from the averaging kernel matrix. The advantage of using the averaging kernels to calculate vertical resolution is that the method is now identical for both lidars and it is possible to compare both lidars on an identical scale. Also, OEM does not required any additional smoothing to retrieve temperature.

The HOPE campaign found that the DWD uncertainty calculation was off by a factor of $\sqrt{5}$, which reduced the uncertainty from $22\,\mathrm{K}$ to $10\,\mathrm{K}$. One of the strengths of the OEM is that it propagates the uncertainty parameters automatically and provides the complete uncertainty budget. The maximum OEM-calculated statistical uncertainty for the DWD lidar was $6\,\mathrm{K}$ at $70\,\mathrm{km}$. The NASA lidar has an OEM statistical uncertainty of $0.8\,\mathrm{K}$ at $70\,\mathrm{km}$ and around $2\,\mathrm{K}$ at $80\,\mathrm{km}$.

Figure 4.6 shows that up to $70\,\mathrm{km}$ where both averaging kernels are roughly equal to each

other, the OEM and degraded OEM produces similar results. Weighting with the averaging kernel becomes useful when the averaging kernel is less than 1 (when both averaging kernels are 1 we can compare directly). When the averaging kernel is less than 1, we can use it to weight the NASA temperature and compare it to DWD. When we do this, we can see the result between 70 and 80 km changes and shows smaller differences between the two lidars' temperature measurements. Above 80 km the DWD temperature is essentially the *a priori*, which is why the weighted OEM difference goes to zero.

When comparing two lidars together, or a lidar with a satellite instrument, the OEM averaging kernels provide valuable information about the vertical resolution of the temperature retrieval, as well as a means to weight the measurements for more accurate comparisons. The comparison between the lidar (DWD and NASA) and satellite instrument (MLS and SABER) temperature profiles revealed that, using satellite averaging kernels (if is applicable) can improve the comparison if they are large enough. The temperature comparison improved significantly on the order of 3-4 K in the region where the lidar temperature profiles are valid (below 0.9 **Au**) and the MLS averaging kernels are greater than 0.6.

Bibliography

Baumgarten, K., M. Gerding, G. Baumgarten, and F.-J. Lübken. Temporal variability of tidal and gravity waves during a record long 10-day continuous lidar sounding. *Atmospheric Chemistry and Physics*, 18(1):371–384, 2018.

Ferrare, R. A., T. J. McGee, D. Whiteman, J. Burris, M. Owens, J. Butler, R. A. Barnes, F. Schmidlin, W. Komhyr, P. H. Wang, M. P. McCormick, and A. J. Miller. Lidar measurements of stratospheric temperature during stoic. *Journal of Geophysical Research: Atmospheres*, 100(D5):9303–9312, 1995.

Gross, Michael R., Thomas J. McGee, Richard A. Ferrare, Upendra N. Singh, and Patrick Kimvilakani. Temperature measurements made with a combined rayleigh-mie and raman lidar. *Appl. Opt.*, 36(24):5987–5995, Aug 1997.

Jalali, A., S. Hicks-Jalali, R. J. Sica, A. Haefele, and T. Clarmannvon . A practical method to

remove a priori information from lidar optimal estimation method retrievals. *Atmospheric Measurement Techniques Discussions*, 2018:1–23, 2018a. doi: 10.5194/amt-2018-347.

Jalali, A., R. J. Sica, and A. Haefele. A middle latitude rayleigh-scatter lidar temperature climatology determined using an optimal estimation method. *Atmospheric Measurement Techniques Discussions*, 2018:6043–6058, 2018b. doi: 10.5194/amt-11-6043-2018.

Leblanc, T., R. J. Sica, J. A. E. Gijselvan , S. Godin-Beekmann, A. Haefele, T. Trickl, G. Payen, and G. Liberti. Proposed standardized definitions for vertical resolution and uncertainty in the ndacc lidar ozone and temperature algorithms – part 2: Ozone dial uncertainty budget. *Atmospheric Measurement Techniques*, 9(8):4051–4078, 2016.

McGee, Thomas J., Michael Gross, Richard Ferrare, William Heaps, and Upendra Singh. Raman dial measurements of stratospheric ozone in the presence of volcanic aerosols. *Geophysical Research Letters*, 20(10):955–958, 1993.

McGee, Thomas J., Michael R. Gross, U. Singh, James J. Butler, and Patrick E. Kimvilakani. Improved stratospheric ozone lidar. *Optical Engineering*, 34:1421–1430, 1995.

Mlynczak, Martin G. and James M Russell. An overview of the saber experiment for the timed mission. Number NASA Langley Res. Cent. Langley, Va., 1995.

Nathaniel J. Livesey, Paul A. Wagner Lucien Froidevaux Alyn Lambert Gloria L. Manney Luis F. MillÃạn Valle Hugh C. Pumphrey Michelle L. Santee Michael J. Schwartz Shuhui Wang Ryan A. Fuller Robert F. Jarnot Brian W. Knosp Elmain Martinez Richard R. Lay, William G. Read. Version 4.2x level 2 data quality and description document. *JPL D-33509 Rev. D*, 18(Version 4.2x–3.1), 2018.

Nicolet, M. On the molecular scattering in the terrestrial atmosphere: an empirical formula for its calculation in the homosphere. *Planet. Space Sci.*, 32:1467–1468, 1984.

Randel, William, Petra Udelhofen, Eric Fleming, Marvin Geller, Mel Gelman, Kevin Hamilton, David Karoly, Dave Ortland, Steve Pawson, Richard Swinbank, Fei Wu, Mark Baldwin, Marie-Lise Chanin, Philippe Keckhut, Karin Labitzke, Ellis Remsberg, Adrian Sim-

mons, and Dong Wu. The sparc intercomparison of middle-atmosphere climatologies. *Journal of Climate*, 17(5):986–1003, 2004.

Schwartz, M. J., A. Lambert, G. L. Manney, W. G. Read, N. J. Livesey, L. Froidevaux, C. O. Ao, P. F. Bernath, C. D. Boone, R. E. Cofield, W. H. Daffer, B. J. Drouin, E. J. Fetzer, R. A. Fuller, R. F. Jarnot, J. H. Jiang, Y. B. Jiang, B. W. Knosp, K. Kruger, J.-L. F. Li, M. G. Mlynczak, S. Pawson, J. M. Russell, M. L. Santee, W. V. Snyder, P. C. Stek, R. P. Thurstans, A. M. Tompkins, P. A. Wagner, K. A. Walker, J. W. Waters, and D. L. Wu. Validation of the aura microwave limb sounder temperature and geopotential height measurements. *Journal of Geophysical Research: Atmospheres*, 113(D15), 2008.

Sica, R J and A Haefele. Retrieval of temperature from a multiple-channel Rayleigh-scatter lidar using an optimal estimation method. *Appl. Optics*, 54(8):1872–1889, 2015.

Sica, R. J. and A Haefele. Retrieval of water vapor mixing ratio from a multiple channel Raman-scatter lidar using an optimal estimation method. *Appl. Optics*, 55(4):763–777, 2016.

Sica, R. J., M. R. M. Izawa, K. A. Walker, C. Boone, S. V. Petelina, P. S. Argall, P. Bernath, G. B. Burns, V. Catoire, R. L. Collins, W. H. Daffer, C. De Clercq, Z. Y. Fan, B. J. Firanski, W. J. R. French, P. Gerard, M. Gerding, J. Granville, J. L. Innis, P. Keckhut, T. Kerzenmacher, A. R. Klekociuk, E. Kyrö, J. C. Lambert, E. J. Llewellyn, G. L. Manney, I. S. McDermid, K. Mizutani, Y. Murayama, C. Piccolo, P. Raspollini, M. Ridolfi, C. Robert, W. Steinbrecht, K. B. Strawbridge, K. Strong, R. Stübi, and B. Thurairajah. Validation of the atmospheric chemistry experiment (ace) version 2.2 temperature using ground-based and space-borne measurements. *Atmospheric Chemistry and Physics*, 8(1): 35–62, 2008. doi: 10.5194/acp-8-35-2008.

Singh, Upendra N., Philippe Keckhut, Thomas J. McGee, Michael R. Gross, Alain Hauchecorne, Evan F. Fishbein, Joe W. Waters, John C. Gille, Aidan E. Roche, and James M. Russell. Stratospheric temperature measurements by two collocated ndsc lidars during uars validation campaign. *Journal of Geophysical Research: Atmospheres*, 101(D6): 10287–10297, 1996.

Steinbrecht, W., T. J. McGee, L. W. Twigg, H. Claude, F. Schonenborn, G. K. Sumnicht, and D. Silbert. Intercomparison of stratospheric ozone and temperature profiles during the october 2005 hohenpeisenberg ozone profiling experiment (hope). *Atmospheric Measurement Techniques*, 2(1):125–145, 2009.

Wing, R., A. Hauchecorne, P. Keckhut, S. Godin-Beekmann, S. Khaykin, and E. M. McCullough. Lidar temperature series in the middle atmosphere as a reference data set. part b: Assessment of temperature observations from mls/aura and saber/timed satellites. *Atmospheric Measurement Techniques Discussions*, 2018:1–23, 2018.

Wu, D.L., W.G. Read, Z. Shippony, T. Leblanc, T.J. Duck, D.A. Ortland, R.J. Sica, P.S. Argall, J. Oberheide, A. Hauchecorne, P. Keckhut, C.Y. She, and D.A. Krueger. Mesospheric temperature from uars mls: retrieval and validation. *Journal of Atmospheric and Solar-Terrestrial Physics*, 65(2):245 – 267, 2003.

Chapter 5

Conclusions and Future Plans

In Chapter 2, I used an Optimal Estimation Method (OEM) to retrieve temperatures from more than 500 nights of PCL Rayleigh measurements from 1994 to 2013 and used to calculate an OEM temperature climatology between 30 and 110 km altitude. The OEM provided significant advantages over the traditional method in the form of increasing the altitude range of the temperatures by providing the averaging kernels at each altitude as a diagnostic tool. The uncertainty budget, including systematic and statistical uncertainties, and the vertical resolution for the PCL temperature climatology were calculated using the OEM on a profile-by-profile basis. I determined a quantitative cutoff height using the OEM temperature averaging kernels and validated them by comparing them to sodium lidar temperatures. In the traditional method, it is necessary to merge profiles from different lidar channels to create a single temperature profile. This issue was investigated in Jalali (2014). The process involved combining various random uncertainties, choosing overlap ranges, and calculating uncertainties due to merging raw photocount profiles, all of which contributed to the uncertainties in a manner difficult to quantify. The OEM does not require merging to incorporate data from multiple sources, and therefore removes the added uncertainty due to the merging process in the HC method. We also validated the OEM by comparing the PCL temperature climatology with sodium lidar climatologies and we found that the OEM-derived Rayleigh temperature climatology improved agreement relative to our previous comparisons using the traditional method, and the agreement of the OEM-derived temperatures is the same as the agreement between existing sodium lidar temperature climatologies.

In Chapter 3, I presented a method to remove the effect of the water vapour and temperature *a priori* information from the OEM water vapour and temperature lidar retrievals using their averaging kernels. This method was validated by applying it to a few nights of measurements of PCL temperature and RALMO water vapour retrievals. The main advantage of the *a priori* removal method is that it removes the *a priori* information from the OEM retrieval and improves the retrieval in the regions where the lidar signal-to-noise ratio is low. In water vapour profiles, where the signal level is determined by the amount of water vapour present in the atmosphere above the lidar, the *a priori* removal method improves the comparison to the radiosonde in regions where there is little water vapour and thus low signal-to-noise ratio measurements, particularly in the daytime. This improvement is useful for forecast models which rely on accurate tropospheric measurements for precipitation forecasts where small changes in water vapour can make large differences in the model predictions. An extension of this project would be to apply the method to the RALMO water vapour climatology to possibly gain more measurements in the upper troposphere and lower stratosphere (UTLS). There are very few accurate measurements of the UTLS region, despite its importance in understanding water vapor transport and the water cycle.

In Chapter 4, I used the OEM temperature retrieval averaging kernels to make an intercomparison between the NASA and DWD lidars, as well as between the lidars and SABER and MLS satellite temperature profiles. A common vertical resolution was calculated from the averaging kernel matrix, which improved the intercomparison by having both lidars on an identical height scale. By using OEM, the averaging kernels of the satellite or another lidar as a second instrument can be used to weight or "degrade" the lidar (first instrument) temperature profiles. The degraded lidar temperature profiles showed better agreement with the other lidar or satellite temperature profiles. This better agreement is due to using the averaging kernels as weighting functions and assumes that the degraded instrument's measurements are looking through the same atmosphere as the non-degraded instrument's. Future work for this project could be to use the degraded lidar temperature profiles, in order to improve the comparison of a lidar temperature climatology with satellite temperature climatology.

An extension of this thesis would be to compare the OEM PCL climatology with the

136

SABER climatology. This would require using coincident nights between the PCL measurements and SABER. However, the temporal coverage of the climatology is limited by the SABER launch date (2001) and a significant number of the PCL measurements were taken before 2001. This would yield an incomplete climatology as the PCL lacks a sufficient number of measurements during the winter. The better option for a satellite-lidar temperature measurement comparison would be to use the OEM on temperature measurements from the Observatory de Haute-Provence (OHP) in France. The OHP lidar has more coincident nights that could be used to compare with SABER or other recent satellites.

The PCL is a member of the International Network for the Detection of Atmospheric Composition Change (NDACC). There are roughly 7 Rayleigh lidars, including the PCL, with long-term temperature data sets. The primary focus of NDACC has been to investigate the physics and chemistry of the upper troposphere, stratosphere and mesosphere. The results of this thesis could improve the lidar community's research quality as a whole. The OEM increases the valid temperature measurements by $5 - 10\,\mathrm{km}$ for all three lidars used in this thesis and also provides a detailed uncertainty budget on a profile-by-profile basis. Using the OEM enables us to obtain useful information from the top $10\,\mathrm{km}$ of a lidar temperature profile. Typically, gaining $10\,\mathrm{km}$ in height would require a higher power laser or expanding the telescope diameter, both of which are expensive upgrades. Therefore, applying the OEM is comparable to a significant hardware upgrade.

The OEM can be used to extend temperature profiles for any Rayleigh-scatter lidar systems without extra cost. Extending the PCL temperature climatology up to $100\,\mathrm{km}$ will enable more in-depth studies of the dynamics of the MLT, such as the variations in height of the mesopause, which can rise to over $100\,\mathrm{km}$ altitude in the winter. This heights is beyond the range of many current Rayleigh systems that must cut-off the top of their measurements. Extending the PCL temperature measurements allows us to study the annual and semi-annual cycle of the MLT up to $100\,\mathrm{km}$.

Better understanding of the middle atmosphere and MLT region temperature has been shown to improve surface forecast model accuracy. Therefore, increasing the maximum range of lidar temperature retrievals into the upper atmosphere with a better assessment of measurement uncertainties will be useful to the modeling and forecasting community.

In the future, the OEM could be applied to all NDACC lidar measurements to have an image of temperature trends in the middle atmosphere at different altitudes, especially through the mesosphere and aid in the detection of global climate change. Using the OEM for all of these lidars would provide standard uncertainty budgets as well as their averaging kernels which would make comparison studies easier and more meaningful between them. One of the main concerns of the atmospheric lidar scientists regarding the OEM is the impact of the *a priori* on the OEM retrievals. The *a priori* removal technique presented in this thesis could satisfy their concerns by removing the removing the effect of the *a priori* from retrievals in addition to gaining extra information in low signal-to-noise ratio regions.

Bibliography

Jalali, Ali. Extending and merging the purple crow lidar temperature rayleigh and vibrational raman climatologies. *Master's thesis, The University of Western Ontario*, 2490, 2014.

VITA

Ali Jalali

Department of Physics & Astronomy, University of Western Ontario

London, Ontario, Canada, N6A 5B7

Education

2000-2005	University Of Urmia, Urmia, Iran, Solid state Physics, B.Sc.
2006-2009	University of Tehran, Tehran, Tehran, Iran, Meteorology, M.Sc.
2012-2014	University of Western Ontario, London, Ontario, Canada, Physics, M.Sc.
2014-2018	University of Western Ontario, London, Ontario, Canada, Physics, Ph.D.